X-ray Binary Evolution: The Effects of Self-Induced Irradiation

Jérôme Quintin
Bishop's University

Submitted to the Department of Physics
in partial fulfillment of the requirements for the degree of
Bachelor of Science.

Abstract

An extensive grid of binary evolutionary tracks has been computed using the `MESA` code to study irradiated X-ray binary systems. Non-irradiated X-ray binaries have been well studied, but this thesis shows how irradiation affects the evolution of low- and intermediate mass X-ray binaries (LMXBs and IMXBs) and their long-term secular average properties. Since the donor star loses some of its mass to the neutron star, an accretion disk is formed around the neutron star and X-rays are emitted. Some of this radiation is intercepted by the donor star and this in turn modifies its physical properties. A model that includes the geometry of the binary system and a Monte-Carlo simulation to determine the penetration depth of X-rays has been developed. For instance, assuming an efficiency factor as low as 5% for the irradiation flux, the bloating of the donor star can lead to irradiation cycles in which mass transfer surpasses the Eddington limit, which means that the neutron star will accrete less mass. If irradiation is not considered, neutron stars can become as massive as $2.5\,M_{\odot}$. But if irradiation is included, they generally accrete less mass and their masses are often less than $2.0\,M_{\odot}$. However, irradiation does not have a significant effect on the orbital period at which the system becomes detached (e.g., formation of a millisecond pulsar). Therefore, irradiation is a promising mechanism to explain the observed properties of binary millisecond pulsars.

Acknowledgments

I would like to express my deep and sincere gratitude to my supervisor Dr. Lorne Nelson for his generosity to transmit his knowledge. This work benefited greatly from his patience, his guidance, and his tremendous help. I would like to thank Dr. Jinrong Lin for his generosity and time while he was busy writing his Ph.D. thesis at MIT. I thank him for introducing me to the `MESA` code and how to run it on the Mammoth computer cluster. I also thank Dr. Saul Rappaport from MIT for interesting and enlightening discussions on binary evolution and irradiation. Obviously, I must be grateful to Dr. Bill Paxton (from UCSB) and his team for building the open-access `MESA` code and for improving it all the time. I thank the Réseau québécois de calcul de haute performance (RQCHP) for allowing me to use extensively the Mammoth computer cluster at the Université de Sherbrooke. Finally, I thank the Natural Sciences and Engineering Research Council of Canada (NSERC) that, in part, allowed me to present my work at national and international conferences.

Contents

Chapter 1

Introduction

In the 1960s, the first X-ray satellites were sent in orbit around the Earth and they led to the discovery of the first X-ray sources such as Scorpius X-1 and Cygnus X-1. Then, astronomers observed the X-ray sources in the optical band and they only found faint old stars. Thus, they concluded after some time that the X-rays would be the result of matter accretion onto compact objects such as black-holes and neutron stars. Such objects are now called X-ray binary systems, where a companion star and a compact star orbit in close proximity, emitting X-rays when mass is transferred from the former to the latter.

X-ray binary systems containing non-degenerate stars can be separated into three classes depending on the mass of the companion. For a low mass companion star ($M \lesssim 2.2\,M_{\odot}$), one refers to a low mass X-ray binary (LMXB), and equivalently, one refers to intermediate and high mass X-ray binaries (IMXBs and HMXBs) for companions in the ranges $2.2\,M_{\odot} \lesssim M \lesssim 10\,M_{\odot}$ and $M \gtrsim 10\,M_{\odot}$, respectively.

This thesis focuses on LMXBs and IMXBs, and more specifically, on their evolution. The field of LMXB evolution began in the early 1970s and has been thriving since then (e.g., [40, 134, 177, 71, 105, 127, 128, 17, 65, 122, 119, 106, 14]). One may be interested in understanding the formation of LMXBs, but this work focuses on the subsequent portion of the evolution, that is when mass is transferred from the companion star to the compact object. In this work, it will be assumed that the compact object is a neutron star. Studying X-ray binary systems with black-holes requires one to consider different physics that will not be discussed here.

Our understanding of the evolution of X-ray binary systems is largely due to numerical simulations which allow us to study the possible evolutionary paths of X-ray binaries. In recent years, the increasing power of computer clusters allowed theorists to investigate the evolution many X-ray binaries. For example, Podsiadlowski et al. [122] computed the evolution of about 150 LMXBs and IMXBs, and less than ten years later, Lin et al. [90] computed the evolution of about 42,000 systems. This thesis presents evolutionary grids of 4,200 systems (one tenth of Lin et al.'s density), where the initial conditions are taken in the

two-dimensional parameter space $P_{orb,i} - M_{2,i}$ (initial orbital period and initial companion star mass). However, this thesis does not show the results of only one evolutionary grid, but the results of 11 grids of 4,200 systems, where each grid changes the value of its additional parameters such as $M_{1,i}$, η, and β_{max} (the initial neutron star mass, the irradiation efficiency, and the maximum mass-transfer fraction). The meaning of these parameters will be discussed thoroughly in this thesis.

This thesis is separated in two parts. The first part focuses on the theory of X-ray binary systems such as stellar evolution, the mechanics of close binaries, and neutron star properties. Also, it discusses the standard evolution of LMXBs and IMXBs. The second part introduces the physics of self-induced X-ray irradiation. Chapter 3 discusses the model developed in this thesis to consider the effects of X-ray irradiation in the evolution of X-ray binary systems. Then, Chapter 4 shows new evolutionary grids including the effects of self-induced irradiation. Finally, the results are summarized in Chapter 5.

Part I

Theory and Background

Chapter 2

X-ray Binary Systems

The research results contained in this thesis concern compact binary systems consisting of a degenerate primary (a neutron star) and a main-sequence (or post-main sequence) companion. From now on, the companion star will be called the donor star. The origin of this name will soon become clear. In order to successfully model X-ray binary systems, one needs a stellar evolution code that computes the evolution of the donor star, the evolution of the neutron star, and the evolution of the system as a whole, i.e. that considers the interactions between the two stars. In this chapter, the theory of stellar evolution is explored and the evolution computer code is discussed. The theory behind binary evolution is developed and neutron star properties relevant to X-ray binary evolution are explored. Finally, the standard evolution of LMXBs and IMXBs is analyzed.

It should be noted that Sections 2.1 and 2.2 borrow heavily from the previous work of Dubeau, Goliasch, and Maisonneuve ([37, 50, 99], and references therein). Due to the very nature of the subjects discussed, some of the descriptions differ only moderately.

2.1 Stellar Evolution

The theory of stellar structure and evolution studies the physical processes in stars. It is an attempt to model the variation and distribution of the physical and chemical parameters such as density, pressure, temperature, radiation, and chemical composition of stars over time. There are five basic equations of stellar structure and evolution that emerge from the theory adopted for the stellar models used in this thesis. Each of these equations will be developed and explained in the subsequent sections. In brief, these equations form a complete set of coupled partial differential equations that govern the structural evolution of the stellar models. Each equation relates to one of the following: mass continuity, hydrostatic equilibrium, energy conservation, energy transport, and the temporal evolution of chemical composition.

An important note should be made about the complexity and difficulty of modeling the interior of stars and their physical processes. For this reason, some fundamental simplifying assumptions have to be made when developing such a model. Hence, for the remainder of the discussion in this chapter (and most of this thesis) the assumption is made that stars can be approximated as spherically symmetric and non-rotating. Additionally, the distortion effects of close companions are neglected and so are the consequences of the presence of magnetic fields. Similarly, the density, pressure, and chemical composition are assumed to be distributed radially. This set of assumptions allows the models generated to be described by only one "spatial" coordinate and the variable time, t.

Another important point is that for computational purposes, it is desirable to use what is called the Lagrangian approach when attempting to solve the differential equations (DE's) of stellar structure and evolution, rather than the classical Eulerian scheme. The Eulerian scheme uses fixed points in space as a reference for the independent variable. For stars, this implies following the changes in stellar properties at fixed points a distance r from the center of the star over time. The Lagrangian approach, on the other hand, is a classical hydrodynamic approach in which the reference frame is attached to differential fluid elements. In the case of a spherically symmetric star, these fluid elements then represent differential spherical shells (of mass dm) at a radial distance r from the center. Each mass shell can thus be evaluated as a diffusive, thermodynamic system changing over time. In brief, while both methods use time (t) as one of the independent variables, the Eulerian scheme uses r as the second independent variable, whereas the Lagrangian approach treats m as the second independent variable. The following sections will always conclude with the Lagrangian description of each equation. It should be noted, however, that the expression for the change of the same physical quantity with respect to time using the Eulerian method and the Lagrangian method are interchangeable.

2.1.1 Equations of Stellar Structure and Evolution

2.1.1.1 Mass Continuity

For a spherically symmetric star one can write the mass contained within a differential spherical shell a radial distance r from the center as

$$dm = 4\pi r^2 \rho \, dr \,, \tag{2.1}$$

where ρ is the density within this differential mass shell. With the requirement of mass continuity one can rewrite the above equation as

$$\frac{\partial m}{\partial r} = 4\pi r^2 \rho \,. \tag{2.2}$$

This equation is one of the five equations of stellar structure and evolution, and it is most often termed "equation of mass continuity". Clearly, Equation 2.2 gives the classical Eulerian description of mass continuity (using r as the independent variable). To express mass continuity with m as the independent variable (Lagrangian scheme), one simply inverts Equation 2.2 to obtain

$$\frac{\partial r}{\partial m} = \frac{1}{4\pi r^2 \rho}\,. \tag{2.3}$$

Note that time (t), the second independent variable, does not enter explicitly into the equation of mass continuity. Also note that time is implicitly being held constant in the derivative $\frac{\partial r}{\partial m}$.

2.1.1.2 Hydrostatic Equilibrium

The notion of hydrostatic equilibrium of a mass element describes the situation where all forces acting on that mass element cancel out. Given this constraint and the assumptions applied (gaseous spherical matter without rotation, magnetic fields, or distortion due to a companion), the only forces acting on each particle are due to gravity and the pressure gradient. To derive expressions for these forces, some spherical shell of mass dm and thickness dr at distance r from the center of the star shall be considered. The differential gravitational force per unit area $\left(\frac{dF_g}{A}\right)$ experienced by such a shell is

$$\frac{dF_g}{A} = -\frac{dm\, g_{shell}}{A} = -g\rho dr\,. \tag{2.4}$$

The net differential force per unit area due to pressure (dF_p) is the difference of the pressure on the exterior (P_e) and the interior (P_i) of the shell:

$$\frac{dF_p}{A} = P_i - P_e = -\left(\frac{\partial P}{\partial r}\right) dr\,. \tag{2.5}$$

Imposing the condition of hydrostatic equilibrium ($dF_g = dF_p$), one can equate Equations 2.4 and 2.5 to get

$$\left(\frac{\partial P}{\partial r}\right) = -g\rho = -\frac{Gm}{r^2}\rho\,, \tag{2.6}$$

or expressed in the Lagrangian scheme

$$\left(\frac{\partial P}{\partial m}\right) = -\frac{Gm}{4\pi r^4}\,, \tag{2.7}$$

where G is Newton's Gravitational Constant.

Equation 2.7 (or Equation 2.6 for the Eulerian scheme) is the stellar structure equation termed "equation of hydrostatic equilibrium".

2.1.1.3 Energy Conservation

Energy conservation with respect to a star can be put in this way: the total energy emitted (per unit of time) from a star's surface (luminosity) must be compensated by the total change in energy (per unit of time) in the interior of the star. A similar statement can be made regarding a spherical shell of mass dm within the star that encloses the fractional mass m. If the net energy per second flowing into or out of the shell is defined by L_m, then $\frac{\partial L_m}{\partial m}$ is the specific power gradient transferred through this shell. The value of $\frac{\partial L_m}{\partial m}$ is simply the sum of the different specific energy generation rates (and losses):

ϵ - energy generation rate of nuclear energy (generated within the shell per unit mass per unit time)

ν - energy loss rate due to escaping neutrinos (generated by nuclear reactions and plasma effects)

ζ - energy generation/loss rate due to changes in the thermal state of the matter

The changes in the thermal state of the matter ζ are related to the temperature (T) and the partial derivative of the "specific" entropy (per unit of mass) S of the stellar matter with respect to time by $\zeta = -T\frac{\partial S}{\partial t}$. The equation of stellar structure addressing energy conservation can thus be written as

$$\frac{\partial L_m}{\partial m} = \epsilon - \nu - T\frac{\partial S}{\partial t}\,. \tag{2.8}$$

2.1.1.4 Energy Transport

There are three main processes available to a star that allow it to transfer the energy generated in the interior of the star to its outer layers: conduction, convection, and radiation. The processes are similar in the sense that certain "particles" (photons in the case of radiation, largely degenerate electrons for conduction, and "blobs" of matter during convection) are exchanged between the hotter and cooler layers of the star. The mean free path of the particles, together with the temperature gradient of the surroundings, play a decisive role in the mode of energy transport. Thus, the equation for the energy transport within a star will be written with a condition for the temperature gradient necessary for the required energy flow. The temperature gradient with respect to pressure inside a star can be written as

$$\nabla = \frac{\partial \ln T}{\partial \ln P}\,. \tag{2.9}$$

Rewriting the above equation slightly yields

$$\begin{aligned} \nabla &= \tfrac{P}{T}\left(\tfrac{\partial T}{\partial m}\right)\left(\tfrac{\partial m}{\partial P}\right) \\ \therefore \ \tfrac{\partial T}{\partial m} &= \tfrac{T}{P}\left(\tfrac{\partial P}{\partial m}\right)\nabla\,, \end{aligned} \tag{2.10}$$

which renders, after substituting in Equation 2.7, the equation of stellar structure concerned with energy transport:

$$\frac{\partial T}{\partial m} = -\frac{GmT}{4\pi r^4 P}\nabla\,. \tag{2.11}$$

The temperature gradient (∇) that governs the above equation depends on the dominant mode of energy transport for the particular location in the star. The gradient to be used is either a combination of the radiative and conductive gradient $\nabla_{rad/cond}$ (since the radiative and conductive modes can operate simultaneously) or the convective gradient ∇_{con}. The latter applies to either efficient (adiabatic) or inefficient (superadiabatic) convection. The latter can be viewed as the leakage and transport of radiation from within the convective bubbles.

Radiation and Conduction

Radiative energy transport results from electromagnetic waves (photons) transferring energy between layers in the star. During conductive energy transport, on the other hand, degenerate electrons are the cause of the transfer of energy (very much like heat that is transferred very efficiently in metals). Since both of these modes can take place simultaneously, the "conductivities" of each can be added together. This is achieved by combining their opacities κ in the following way:

$$\frac{1}{\kappa} = \frac{1}{\kappa_{cond}} + \frac{1}{\kappa_{rad}}\,. \tag{2.12}$$

This is akin to saying that the "conductivities" add linearly. The combined temperature gradient due to radiation and conduction can then be written as

$$\nabla_{rad/cond} = \frac{3}{16\pi acG}\frac{\kappa L_m P}{mT^4}\,, \tag{2.13}$$

where c is the speed of light in vacuum and a is the radiation constant. The combined opacity κ is the Rosseland mean absorption coefficient expressed in units of cm^2/g. It should be noted that the conductive energy transport is negligible in most regions of a star since the mean free path of photons is much larger than that of electrons. However, conduction becomes important in dense degenerate regions (the interior of evolved stars and white dwarfs) and, thus, must be accounted for appropriately.

Convection

Convective energy transport is the exchange of energy between hotter and cooler layers of the star through macroscopic mass elements (or "bubbles" of matter). During convection, hotter bubbles move towards less dense regions and dissolve, delivering their excess of heat to their new surroundings. Similarly, cooler bubbles descend into lower layers. This turbulent mixing of stellar matter is an extremely efficient mode of energy transport. It occurs when the temperature gradient of a region becomes comparable with its adiabatic gradient and "blobs" become unstable against convection and begin to rise.

To simplify the complicated and turbulent motion of the convective bubbles a mixing length theory was introduced by Böhm-Vitense [20]. According to her model, convection is treated as the motion of vertically rising bubbles (much like the hot bubbles in a boiling pot of water). Assuming efficient convection (no heat exchange of the bubbles with their surroundings during their rise), the process is adiabatic. In this case, the convective gradient is almost exactly equal to the adiabatic gradient. Thus,

$$\nabla_{con} = \nabla_{ad}\,, \tag{2.14}$$

where the adiabatic gradient is defined as $\nabla_{ad} = \left(\frac{\partial \ln T}{\partial \ln P}\right)_s$, and hence we have

$$\nabla_{con} = \left(\frac{\partial \ln T}{\partial \ln P}\right)_s . \tag{2.15}$$

As stated before, the dominating mode of energy transport (radiation/conduction or convection) for a given layer in a star determines which gradient to substitute into Equation 2.11. Under the assumption that the chemical gradient is negligible, the determination of the dominant mode is thus done by comparing the value of the radiative/conductive gradient (Equation 2.13) of that layer with its adiabatic gradient (Equation 2.15). A radiative/conductive gradient lower than the adiabatic gradient ($\nabla_{rad/cond} < \nabla_{ad}$) implies that radiation is more efficient in transferring energy across that layer; otherwise, the layer is unstable against convection. In summary, Equation 2.11 can thus be rewritten as:

$$\frac{\partial T}{\partial m} = \begin{cases} -\frac{3\kappa}{64\pi^2 acr^4}\left(\frac{L_m}{T^3}\right) & \text{for } \nabla_{rad/cond} < \nabla_{ad} \text{ (radiation)} \\ -\frac{GMT}{4\pi r^4 P}\left(\frac{\partial \ln T}{\partial \ln P}\right)_s & \text{for } \nabla_{rad/cond} \geq \nabla_{ad} \text{ (efficient convection)} \end{cases} . \tag{2.16}$$

2.1.1.5 Temporal Evolution of Chemical Composition

As nuclear reactions take place in a particular region of a star, certain species of atoms are transformed into new ones. Hence, the chemical composition of that region changes over time. On the whole, the chemical composition of the entire star changes through this process. If one denotes the mass fraction of a particular species i by X_i, then one can write

$X_i = X_i(m,t)$, where m is the total mass of the region ($0 < m \leq M_{star}$). The mass fraction of a particular species with nuclear mass m_i is related to its total particle number per unit volume (n_i) by

$$X_i(m,t) = \frac{m_i n_i}{\rho}\,, \tag{2.17}$$

where ρ is the mass density. It should be noted that the sum over all mass fractions must always be equal to unity ($\sum_i X_i = 1$).

The different species that stars are composed of range through the isotopes of many different (mostly ionized) atoms such as H, He, Li, Be, B, C, N, O, [...]. The most abundant species by far are hydrogen (H) and helium (He), and thus the use of the following definitions with regard to the various mass fraction become useful: $X = X_H$, $Y = X_{He}$, and $Z =$ "the rest" $= 1 - X - Y$.

Changes in Mass Fraction in Non-convective Regions

The change in the abundance of a species over time in a region where no mixing takes place is solely governed by the reactions that create the particular species and by the number of reactions destroying it. This change in the abundance of a species i over time can be expressed in terms of its chemical mass fraction X_i by

$$\frac{\partial X_i}{\partial t} = \sum_K \frac{\in_{Ki}}{Q_{Ki}} - \sum_{K'} \frac{\in_{K'i}}{Q_{iK'}}\,, \tag{2.18}$$

where $\in_{Ki}$ and $\in_{K'i}$ are the energies of the K^{th} reaction that contributes to the creation of the species i and the destruction of the species i, respectively. Q_{Ki} is the energy generated when one unit mass of type i is transformed into species i during the K^{th} reaction. Similarly, $Q_{iK'}$ is the energy generated in the destruction of one mass unit of type i into type $K^{'}$.

Changes in Mass Fraction in Convective Regions

In convective zones, the continuous mixing due to the turbulent flow of rising and sinking "blobs" of matter causes the chemical composition to be homogeneous throughout the entire convective region. Hence, it is not sufficient to treat the change in chemical composition locally; rather, an averaging over infinitesimal increments dm across the entire convective zone becomes necessary. Equation 2.18 therefore becomes

$$\frac{\partial X_i}{\partial t} = \frac{\int_{conv\ zone} \left(\sum_K \frac{\in_{Ki}}{Q_{Ki}} - \sum_{K'} \frac{\in_{K'i}}{Q_{iK'}} \right) dm}{\int_{conv\ zone} dm}\,. \tag{2.19}$$

A discontinuity in $\dfrac{\partial X_i}{\partial t}$ might arise on the boundary between two adjacent convective shells. However, by computing changes in the mass fraction for each species over the entire region

one can simply extract X_i for that particular layer. Equation 2.19 thus represents an entire system of equations handling the abundance of every element simultaneously.

As mentioned at the beginning of this chapter, the equations discussed in the preceding sections (Equations 2.7, 2.3, 2.8, 2.11, and 2.18/2.19) form, when combined, a complete set of coupled first-order partial differential equations:

$$\frac{\partial r}{\partial m} = \frac{1}{4\pi r^2 \rho}\,, \tag{2.20}$$

$$\frac{\partial P}{\partial m} = -\frac{Gm}{4\pi r^4}\,, \tag{2.21}$$

$$\frac{\partial L_m}{\partial m} = \epsilon - \nu - T\frac{\partial S}{\partial t}\,, \tag{2.22}$$

$$\frac{\partial T}{\partial m} = -\frac{GmT}{4\pi r^4 P}\nabla\,, \tag{2.23}$$

$$\frac{\partial X_i}{\partial t} = \sum_K \frac{\in_{Ki}}{Q_{Ki}} - \sum_{K'} \frac{\in_{K'i}}{Q_{iK'}}\,. \tag{2.24}$$

They govern the structural evolution of the stellar models used for this work.

To numerically solve these equations, the differential (instantaneous) rates of change have to be replaced by discrete differences ($\partial \to \triangle$). Thus, the following system of algebraic difference equations must be solved:

$$\Delta r = \frac{1}{4\pi r^2 \rho}\Delta m\,, \tag{2.25}$$

$$\Delta P = -\frac{Gm}{4\pi r^4}\Delta m\,, \tag{2.26}$$

$$\Delta L_r = \in -T\frac{\Delta S}{\Delta t}\Delta m\,, \tag{2.27}$$

$$\Delta T = -\frac{GmT}{4\pi r^4 P}\nabla\Delta m\,, \tag{2.28}$$

$$\Delta X_i = \left(\sum\nolimits_K \frac{\in_K}{Q_{Ki}} - \sum\nolimits_{K'} \frac{\in_{K'}}{Q_{iK'}}\right)\Delta t\,. \tag{2.29}$$

It is this set of equations that governs the structure and evolution of the stellar models computed for this work.

2.1.2 The MESA Code

In the previous section, one saw the basics of stellar evolution and its equations. Now, in order to solve Equations 2.25, 2.26, 2.27, 2.28 and 2.29, one needs to write a computer code together with some input physics. Indeed, in order to produce meaningful and physical results when attempting to solve the equations of stellar structure and evolution (presented in Section 2.1), various additional information is required. In fact, when examining the equations of stellar structure and evolution (Equations 2.25 through 2.29), it becomes evident that the system of five equations contains fourteen (or more) variables ("unknowns"). They are time (t), mass (m), radius (r), temperature (T), pressure (P), luminosity (L), density (ρ), opacity (κ), entropy (S), energy generation/loss rates (ϵ, ν), the adiabatic gradient (∇_{ad}), chemical composition (X_i), and the amount of energy released (per unit of mass) during nuclear reactions (Q_{ik}). Choosing time and mass as the independent variables (Lagrangian approach) still leaves eleven unknowns (or more depending on the number of species i that are considered), but only five equations. Consequently, seven or more equations (or constraints) are necessary to allow the stellar structure equations to be solved. These equations are provided by what is called "input physics" (or auxiliary equations). However, the input physics generally do not consist of analytic equations, but provide the necessary relationships through numerical data in tables. This data can be categorized into three main groups: the equation of state, opacities, and nuclear reactions. The equation of state (EOS) provides relationships between ∇_{ad}, ρ, S, T, and P. The data on opacities provides the connection between ρ and T with κ. Information on nuclear reactions reveals the relationship between ϵ, ν, ρ, and T as well as provides data on Q_{ik}. Additionally, all three categories include dependencies on the chemical composition (X_i).

The MESA (Modules for Experiments in Stellar Astrophysics) computer code is the stellar evolution code that is used to produce the results of this thesis. It has been developed by Paxton et al. [118] and it includes all the necessary input physics as well as modern numerical methods to solve for the evolution of a star efficiently. The following paragraphs introduce particularities of the MESA code. However, there are many details that are not discussed here. See Paxton et al. [118] for more details.

The MESA code makes use of several common Fortran libraries for interpolation, solving linear and non-linear equations, solving differential equations, etc. Furthermore, most of the MESA code, entirely written in Fortran, uses the power of parallel programming in order to minimize the computing time. This is particularly useful with modern computer clusters such as the RQCHP's Mammouth-parallel II (the computer cluster used to produce the results of this thesis), which has processors with 24 cores.

The MESA code uses the OPAL equation of state tables from Rogers & Nayfonov [140] and the SCVH tables from Saumon et al. [145] as well as the HELM and PC equations of state (Timmes & Swesty [166] and Potekhin & Chabrier [125], respectively). See Paxton et al. [118] for more details on how these equations of state are used. The other input physics

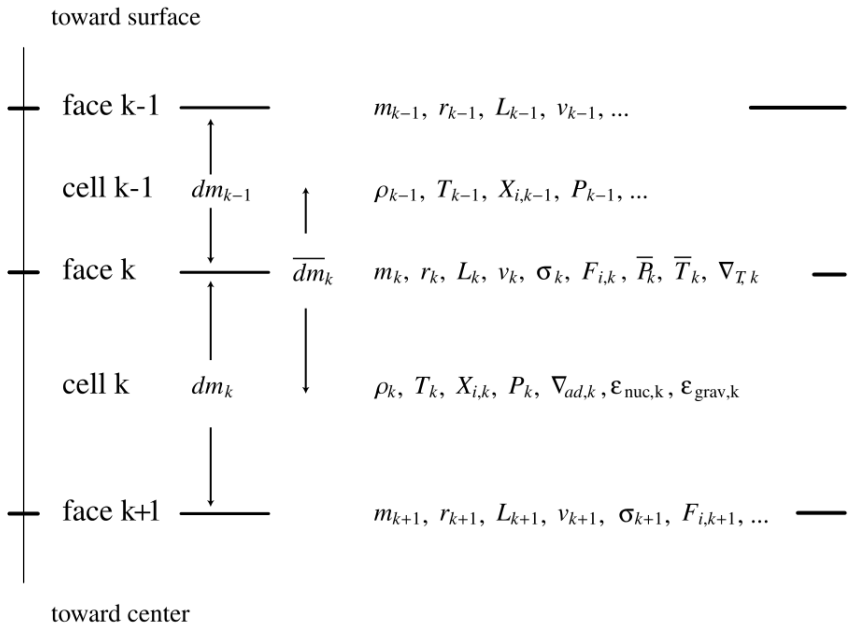

Figure 2.1: Shell (or cell) structure of the MESA code (taken from Paxton et al. [118]).

that are used in the MESA code are the opacities, the thermonuclear and weak reactions, and the nuclear reaction networks, all of which come from many different sources (see Paxton et al. [118], and references therein).

It is useful to note at this point that the equations of state mentioned above allow for different initial stellar metallicities. Note that the LMXBs that are studied in this thesis can be separated in two categories: the ones observed in the galactic plane and the ones observed in globular clusters. This thesis will only focus on the LMXBs observed in the galactic plane. Thus, the donor star will always begin its evolution as a zero aged main sequence star (ZAMS) with a generic metallicity of $Z = 0.02$. On the other hand, globular clusters are composed of very old stars, so they have much lower metallicities. It is important to note that changing the metallicity modifies the evolution of LMXBs (see Nelson et al. [106]).

Note that the MESA code is one-dimensional and spherically symmetric. It divides the star into hundreds or thousands shells, numbered from one at the surface and increasing inward (see Figure 2.1). Then, at each time step, the code simultaneously solves the entire set of partial difference equations (see the end of Section 2.1.1) for each shell, from the surface to the core.

From one time step to another, the MESA code adjusts its mesh, i.e. it modifies the position and the number of shells into which the star is divided. The MESA code is built such that the mesh adjusts itself to facilitate convergence to a solution, which depends on the complexity of nuclear burning, gradients of state variables (such as ρ, T, R), composition,

etc. Also, it selects time steps that minimizes the computational time, but that adjusts itself in order to account for relative changes in state variables. That way, for example, if the density of a particular shell has increased too much from one step to another, the code will shorten the time step to minimize the change in density. Again, for more details on how this is handled numerically, see Paxton et al. [118].

The `MESA` code handles convection and superadiabacity following the mixing length theory of convection as presented by Cox & Giuli [31]. However, since it obviously does not perform three-dimensional hydrodynamical calculations for the convection, it has to account for the hydrodynamical mixing instabilities at convective boundaries using a parametric model. This is called convective overshoot mixing. Paxton et al. [118] follow Herwig [61] and treat overshooting as decaying exponentially with radial distance, i.e. $D_{OV} \propto e^{-z}$, where D_{OV} is the overshoot mixing diffusion coefficient and z is the distance in the radiative layer away from the point where overshoot occurs. Although Herwig's [61] model may be suitable to AGB stars (on the asymptotic giant branch), it is not clear that this is really the physically correct treatment in other situations. In fact, it is believed by some researchers to be highly inaccurate (Ph. Podsiadlowski 2010, private communication). A more standard treatment is to use a Heaviside function,

$$D_{OV} = \begin{cases} D_0\gamma & r_0 < r < r_0 + r_{overshoot} \\ 0 & \text{elsewhere} \end{cases} , \tag{2.30}$$

where

$$D_0 = \frac{v_{c,o}\Lambda}{3} , \tag{2.31}$$

$$r_0 = f_0 H_P , \tag{2.32}$$

and

$$r_{overshoot} = f H_P , \tag{2.33}$$

where the `MESA` code computes the convective velocity ($v_{c,0}$), the mixing length (Λ), and the pressure scale height (H_P). Also, the user has to supply the overshoot step fraction (γ) as well as the parameter f_0 and f, which indicate what fraction of the pressure scale height above the location where $\nabla_{ad} = \nabla_{rad}$ is convective overshooting going to occur. For this thesis, we use the values of $\gamma = 0.25$ (J. Lin 2010, private communication), and $f_0 = 0.05$ and $f = 0.30$ (B. Paxton 2010, private communication). Thus, in this convective overshooting region, standard mixing length theory is applied with a diffusion coefficient D_{OV}.

2.2 Mechanics of Close Binaries

To simplify the discussion on the mechanics of close binary systems a few central assumptions must be made. These assumptions are taken to be valid throughout this section. The first

main assumption is that the orbit is approximately circular. In addition, the donor star's rotation is taken to be synchronized with its orbit. This situation is often referred to as "phase-locked". Those first two assumptions are well justified by the fact that the neutron star has a strong tidal interaction with the donor star. For example, for a $1\,M_\odot$ donor star and a $1.4\,M_\odot$ neutron star with an orbital period of 15 hours, the synchronization time would be of the order of 10^7 years ([63]). Third, the mass of each star is assumed to be distributed such that it can be approximated by a point mass at the center of the corresponding star. Note that throughout the rest of this thesis, variables with index 1 are referring to the neutron star and variables with index 2 are referring to the donor star. Note also that derivatives with respect to time will often be represented by dots, i.e. $\dot{} \equiv \frac{d}{dt}$.

2.2.1 Roche Lobe Geometry

If one assumes the neutron star as well as the donor to be centrally condensed, then they can be approximated by gravitating point sources. Certainly valid for the compact neutron star, the approximation also holds for the donor, considering that the majority of mass in stars is usually concentrated near central regions (and that the equipotential surfaces are roughly spherical). Applying this assumption allows tidal effects and rotational distortions on the stars to be neglected when calculating their gravitational potential. Taking such effects into account would make the subsequent Roche lobe calculations extremely complex since a time-varying potential would need to be considered. In summary, the model used in this work describes the potential field of a binary system with circular orbits in which each component may be treated as a point mass. To illustrate such a potential, a co-rotating Cartesian coordinate system with the origin placed on the center of mass of the neutron star, the z-axis perpendicular to the orbital plane, and the x-axis pointing towards the donor is introduced. The total potential can then be summarized by adding the gravitational potential due to each star and the fictitious centrifugal contribution:

$$\Phi = \Phi_{\text{grav}} + \Phi_{\text{centr}}\,. \tag{2.34}$$

The gravitational potential energy of a test-particle a distance r away from a single point mass M is simply $-\frac{GM}{r}$. The gravitational potential at any position $P(x, y, z)$ for the two masses is thus

$$\Phi_{\text{grav}} = -\left(\frac{GM_1}{(x^2+y^2+z^2)^{\frac{1}{2}}} + \frac{GM_2}{((x-a)^2+y^2+z^2)^{\frac{1}{2}}}\right)\,, \tag{2.35}$$

where a is the orbital separation of the system.

The centrifugal potential of a test-particle a perpendicular distance $r_\perp$ away from the axis of rotation with angular velocity ω is given by $-\frac{1}{2}(\omega r_\perp)^2$. For the two-body setup given

above, one has to take $r_\perp$ to be the distance from the center of mass of the binary (at $\frac{M_2}{(M_1+M_2)}a = \mu a$). Hence,

$$\Phi_{\text{centr}} = -\frac{1}{2}\omega^2((x-\mu a)^2 + y^2)\,, \tag{2.36}$$

with the angular velocity given by $\omega^2 = \frac{G(M_1+M_2)}{a^3}$. The full potential can thus be written as:

$$\Phi = -\frac{GM_1}{(x^2+y^2+z^2)^{\frac{1}{2}}} - \frac{GM_2}{((x-a)^2+y^2+z^2)^{\frac{1}{2}}} - \frac{1}{2}\omega^2((x-\mu a)^2 + y^2)\,. \tag{2.37}$$

Figure 2.2 shows some equipotential lines in the xy-plane of this potential for a fixed M_1, M_2, and a. It should be noted that, as can be seen from Equation 2.35, the equipotentials are really only functions of M_1 and M_2 that scale with a, i.e., $\Phi = \frac{GM_1}{a} f(\frac{x}{a}, \frac{y}{a}, \frac{z}{a}, M_1, M_2)$.

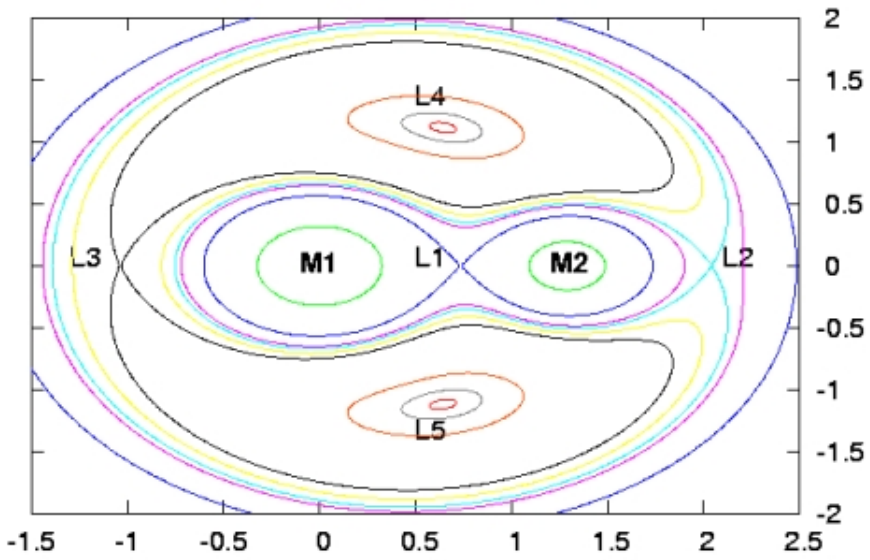

Figure 2.2: Equipotential surfaces in the $z = 0$ plane. Note that $L1$, $L2$, $L3$, $L4$ and $L5$ are known as the Lagrange points (stable and unstable gravitational equilibrium).
Source: *http://www.wissenschaft-online.de/astrowissen/images/intermed/RocheLobes+LagrangePoints.jpg*

Of particular significance in Figure 2.2 is the equipotential that encloses the binary in a figure-eight with each mass located in one of the loops. In three dimensions, this equipotential defines two teardrop-shaped volumes called "Roche lobes", each enclosing one of the masses. The two volumes touch at the point labeled $L1$. This is the "inner Lagrangian point", and

it is a saddle point in potential space considered here. At the inner Lagrangian point, a particle is equally bound to both stars.

It is also important to note that these equipotential surfaces describe the shape of the star. Assuming the response of a star to be hydrostatic, one can use the equation of hydrostatic equilibrium to describe the behavior of a particular fluid element at some point $P(x, y, z)$ with density ρ and pressure p by

$$\frac{1}{\rho} \bigtriangledown p + \bigtriangledown \Phi = 0 \,. \tag{2.38}$$

From the above equation, it can be seen that pressure and density on an equipotential surface are constant (e.g., Shu [152]). If one approximates the density and pressure of a star to be zero (or some other constant value) along its surface, then the surface also runs along an equipotential. This implies that a line of constant potential also describes the shape of a star. Consequently, if the volume of a star in a binary system exceeds its Roche lobe, then mass will flow through the inner Lagrangian point and is captured by its companion. Figure 2.3 gives a slightly more intuitive representation of the potential, and it clearly shows what the consequence of an overfilled Roche lobe would be.

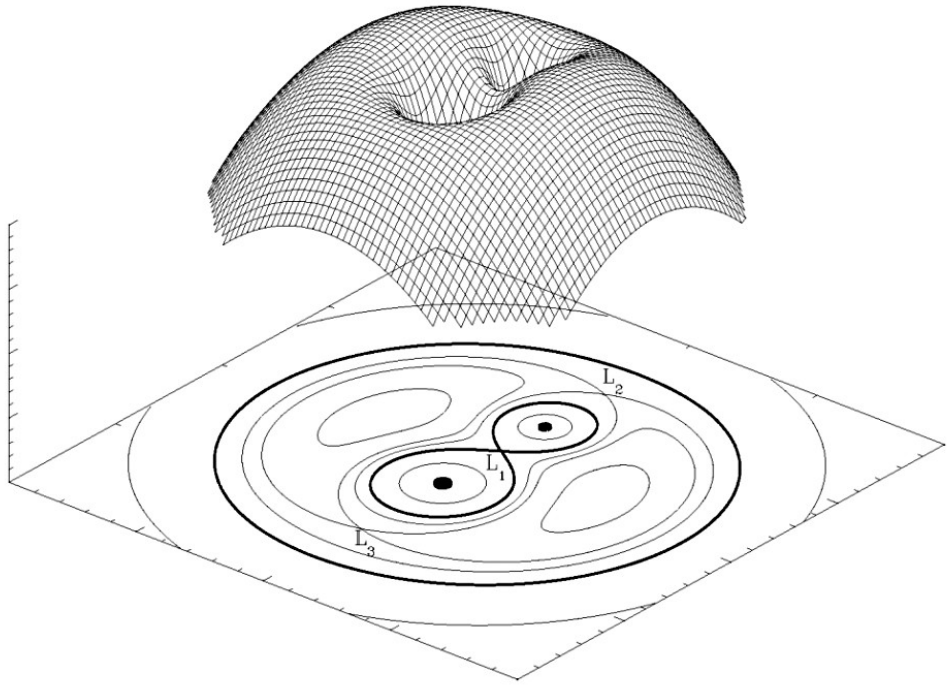

Figure 2.3: Equipotential surface in 2 spatial dimensions and the projections of many surfaces using contour mapping. Source: *https://www.e-education.psu.edu/astro801/files/astro801/image/Lesson%206/800px-RochePotential.jpg*

Inside the Roche lobe, mass is bound to its star. If both stars of a binary system are within their Roche lobe limits, then the system is "detached", and no mass transfer occurs. However, should one star exceed its Roche lobe, then mass will flow off that star and into the potential well of its companion. A system in this state is called semi-detached. Such a picture describes the case of LMXBs and IMXBs, and its consequences with respect to mass transfer will be discussed in subsequent sections. In the case of both stars over-filling their lobes a common envelope would form around the stars, engulfing them. This situation would allow for the possibility for mass to leave the system through the points L2 and L3 (the "second Lagrangian point" and "third Lagrangian point", respectively). This case will not be discussed in this work.

No exact analytical expression in terms of binary parameters (separation, masses, etc.) exists for the size and shape of the Roche lobe. Thus, to minimize computing time, an approximate analytical formula giving the radius of a sphere with the same volume as the corresponding actual Roche lobe is frequently used. The radius of this sphere is often termed "effective Roche lobe radius". Expressing the Roche lobe in terms of its effective Roche lobe radius is especially useful when spherical symmetry is assumed in stellar models. Early work on X-ray binary evolution (e.g., [177, 134, 133]) has used the following formula (see Kopal [82] or Paczyński [114, 115]) that gives the effective Roche lobe radius of the secondary ($R_{L,2}$) as a function of M_1, M_2 and a (the orbital separation of the binary) as long as $0 < M_2/M_1 \lesssim 0.8$:

$$\frac{R_{L,2}}{a} \approx \frac{2}{3^{\frac{4}{3}}} \left(\frac{M_2}{M_1 + M_2} \right)^{\frac{1}{3}} . \tag{2.39}$$

The particular formula used in more recent work (e.g., [122, 106, 50]) and that is used in this project was introduced by Eggleton [39] and is accurate to within 1% for all mass ratios $q \equiv \frac{M_2}{M_1}$. It is written as

$$R_{L,2} \approx \frac{0.49 q^{\frac{2}{3}}}{0.6 q^{\frac{2}{3}} + \ln\left(1 + q^{\frac{1}{3}}\right)} a \,, \tag{2.40}$$

for $0 < q < \infty$.

2.2.2 Mass-Transfer Rate

The `MESA` code computes the mass-transfer rate of the donor star according to the prescription of Ritter [135],

$$\dot{M}_2 = \dot{M}_0 e^{\frac{R_2 - R_L}{H_P}} . \tag{2.41}$$

Note that H_P is the pressure scale height at the surface of the donor star, and it can be computed as follows,

$$H_P = \frac{P_s}{g_s \rho_s}\,, \tag{2.42}$$

where P_s, $g_s = \frac{GM_2}{R_2^2}$, and ρ_s are the pressure, local gravitational acceleration, and density at the surface of the donor star, respectively. Also, the `MESA` code uses $\dot{M}_0 \equiv -5{\times}10^{-10}\, M_\odot\, \mathrm{yr}^{-1}$.

2.2.3 Angular Momentum Loss

There are two ways in which an initially detached binary system can come into contact. The simplest way is for one of the stars in the system to expand in radius until it reaches its Roche lobe limit. In simple terms, the star "grows" into its Roche lobe due to nuclear evolution. The other possibility for a system to come into contact is for the Roche lobe of a star to decrease in size until it reaches the surface of the star. Here, one could say that the Roche lobe "shrinks" onto the star. Such a reduction in the size of the Roche lobe must be the result of a decrease in the binary's orbital separation (recall from Section 2.2.1 that the potential scales with a, the orbital separation). Both situations can bring a binary into a semi-detached state and allow for the onset of mass transfer from one star to the other.

The fact that the loss of angular momentum in a binary leads to a decreased orbital separation is most easily understood when considering the following equation:

$$J^2 = G\frac{(M_1 M_2)^2}{(M_1 + M_2)}\, a\,. \tag{2.43}$$

This equation gives the instantaneous orbital angular momentum of a synchronized binary system with circular orbits about the center of mass. Here, G is the gravitational constant, M_1 and M_2 are the masses of the neutron star and donor star, respectively, and a is the orbital separation. Looking at Equation 2.43, one can see that a direct loss of angular momentum from a binary system must result in a decrease in orbital separation (assuming no mass transfer). The subsequent two sections of this thesis will discuss the two sinks of angular momentum that are deemed most significant and considered in this thesis: magnetic braking and gravitational radiation. Also, a detailed analysis with regard to the changes in orbital separation due to mass loss from the system and the redistribution of mass within the system will be presented.

2.2.3.1 Specific Angular Momentum of Mass Leaving the System

The most obvious way a binary system can lose angular momentum is through matter escaping the system. In the case of X-ray binaries, it will be seen in Section 2.3.1 that neutron stars have a critical accretion rate, so it is easy to imagine that not all mass flowing off the donor

star is accreted onto the neutron star (or is contained in the accretion disk). Thus, what follows is a simple analysis with regard to the specific angular momentum carried away by some small amount of mass δm escaping the system. The setup considers two point masses, M_1 and M_2, orbiting their common center of mass (CM) in circular orbits. The distances from this center of mass to the first and second mass are given by r_1 and r_2, respectively. The separation of the two masses is thus $r_1 + r_2 = a$. The angular momentum of a particle of mass δm a distance r_1 away from the axis of rotation (center of mass) is then given by

$$\vec{\delta J} = \vec{r_1} \times \delta m \, \vec{v_\perp} \,, \tag{2.44}$$

where $\vec{v_\perp}$ is the tangential velocity of the particle and $|\vec{v_\perp}| = \omega r_1$ (with ω representing the angular velocity of the particle). Since $\vec{r_1}$ is perpendicular to $\vec{v_\perp}$, one can write

$$\left|\vec{\delta J}\right| = r_1 \, \delta m \, r_1 \omega = r_1^2 \, \delta m \, \omega \,. \tag{2.45}$$

The definition of the center of mass gives $M_2 r_2 = M_1 r_1$ and therefore $r_1 = \frac{M_2}{(M_1+M_2)} \, a$. Hence, Equation 2.45 yields

$$\delta J = \frac{M_2^2}{M_T^{\frac{3}{2}}} a^{\frac{1}{2}} G^{\frac{1}{2}} \delta m \,, \tag{2.46}$$

where the angular velocity, ω, has been replaced by $\sqrt{\frac{G(M_1+M_2)}{a^3}}$. Equation 2.46 gives the orbital angular momentum of a particle with mass δm located at the position of M_1.

By applying the above result to X-ray binary systems and assuming that all escaping matter leaves the system from the position of the neutron star, one arrives at the equation for a system's change in angular momentum due to mass lost from the system:

$$\left(\frac{dJ}{dt}\right)_{\dot{M}} = \frac{M_2^2}{M_T^{\frac{3}{2}}} a^{\frac{1}{2}} G^{\frac{1}{2}} \frac{dm}{dt} \,. \tag{2.47}$$

Thus, noting that $\frac{dm}{dt}$ is really the change of mass of the whole system, one obtains

$$\frac{1}{J}\left(\frac{dJ}{dt}\right)_{\dot{M}} = \frac{M_2}{M_1 \, M_T} \dot{M}_T \,. \tag{2.48}$$

More generally, the angular momentum loss due to mass loss can be written as (e.g., [170, 157])

$$\frac{\dot{J}_{\dot{M}}}{J_{orb}} = \frac{\tilde{\alpha} + \tilde{\beta} q^2 + \tilde{\delta} \gamma (1+q)^2}{1+q} \frac{\dot{M}_2}{M_2} \,, \tag{2.49}$$

where $\tilde{\alpha}$, $\tilde{\beta}$, and $\tilde{\delta}$ are the fractions of mass lost from the donor star in the form of direct fast wind, the mass ejected from the vicinity of the neutron star, and from a circumbinary

coplanar toroid (with radius $a_r = \gamma^2 a$), respectively (see Soberman et al. [153] for more details on circumbinary coplanar toroid). Recall that $q \equiv M_2/M_1$. For this work, one can ignore the first and third effects since they are negligible. Thus,

$$\frac{\dot{J}_{\dot{M}}}{J_{orb}} = \frac{\tilde{\beta} q^2}{1+q} \frac{\dot{M}_2}{M_2}\,, \tag{2.50}$$

which can be rewritten as

$$\frac{\dot{J}_{\dot{M}}}{J_{orb}} = \tilde{\beta} \frac{M_2}{M_1 M_T} \dot{M}_2\,. \tag{2.51}$$

This equation is precisely Equation 2.48 under the definition $\tilde{\beta} \equiv \dot{M}_T/\dot{M}_2$. In general, it is more useful to define a transfer fraction β rather than a fraction of the mass lost, i.e. $\beta \equiv 1 - \tilde{\beta}$, or equivalently,

$$\beta \equiv -\frac{\dot{M}_1}{\dot{M}_2}\,. \tag{2.52}$$

Thus, using Kepler's Third Law and Equation 2.43, one can write

$$\dot{J}_{\dot{M}} = (1-\beta)\dot{M}_2 \left(\frac{M_2}{M_T}\right)^2 a^2 \omega\,, \tag{2.53}$$

where $\omega = \frac{2\pi}{P_{orb}}$. This equation is precisely what is used in the `MESA` code.

So far, it has been assumed that matter leaves the system close to the neutron star. However, it is possible to be more general and explore the possibility that matter leaves the system closer to the donor star or exactly at the neutron star. In this case, one can write (e.g., [133, 122])

$$\dot{J}_{\dot{M}} = \alpha(1-\beta)\dot{M}_2 a^2 \omega\,. \tag{2.54}$$

Note that if one takes

$$\alpha = \left(\frac{M_2}{M_T}\right)^2\,, \tag{2.55}$$

one obtains Equation 2.53. However, some authors (e.g., [122, 36]) prefer to use a value of 1 for α, which means that they assume that all the mass leaves the system exactly at the neutron star. For this thesis, the opposite case has been tested, i.e. $\alpha = 0$, which would mean that all the mass leaves the system exactly at the center of mass of the binary system. In this case, no orbital angular momentum is lost due to mass loss, and computing a few evolutionary tracks shows that this leads to X-ray binaries with much larger orbital periods and very massive neutron stars ($> 2.5 M_\odot$). For reasons that will become clear later (see Section 2.3.2), this is not favored. For this reason, α is chosen according to Equation 2.55 in this thesis, but again, the prescription for α is still a matter of discuss.

It will be seen in Section 2.3 how mass can leave X-ray binary systems. However, the exact value of β in Equation 2.53, the mass-transfer fraction, cannot be estimated observationally

nor theoretically. There are reasons to believe that the physical processes explored in Section 2.3 are not the only one that can lead to mass loss. Thus, the maximum mass-transfer fraction (β_{max}) is a free parameter. The value of β and β_{max} will be further discussed in Sections 2.3 and 2.4.4, respectively.

2.2.3.2 Gravitational Radiation

Based on Einstein's Theory of General Relativity, gravitational quadrupole radiation must be produced by any accelerating asymetrically rotating massive body (e.g., [102]). This radiation is thus a form of energy lost from the system (e.g., [86]). In the case of a binary with circular orbits, the energy lost from the system due to gravitational radiation (when averaged over one period) can be expressed as

$$\frac{dE}{dt} = -\frac{32}{5}\frac{G}{c^5}\left(\frac{M_1 M_2}{M_1 + M_2}\right)^2 a^4 \omega^6 \,, \tag{2.56}$$

where c is the speed of light (see Andronov et al. [3]). A corresponding expression for the loss of angular momentum due to gravitational radiation can be obtained by realizing that for circular orbits $\frac{dJ}{dt} = \frac{1}{\omega}\frac{dE}{dt}$. A proof for this relationship can be found in Appendix C.2 of Goliasch [50]. Then, the corresponding equation for loss of angular momentum due to gravitational radiation of a binary system with circular orbit is

$$\left(\frac{\partial J}{\partial t}\right)_{GR} = -\frac{32}{5}\frac{G}{c^5}\left(\frac{M_1 M_2}{M_1 + M_2}\right)^2 a^4 \omega^5 \,, \tag{2.57}$$

which can be rewritten as

$$\left(\frac{\partial J}{\partial t}\right)_{GR} = -\frac{32}{5}\frac{G^{\frac{7}{2}}(M_1 + M_2)^{\frac{1}{2}}}{c^5} M_1^2 M_2^2 \, a^{-\frac{7}{2}} \,. \tag{2.58}$$

2.2.3.3 Magnetic Braking

Gravitational radiation is a constant sink of angular momentum for systems considered in this thesis. However, there is a third mechanism believed to dissipate orbital angular momentum. This mechanism is most often called "magnetic braking" and is due to a "magnetic stellar wind". It generally dominates over gravitational radiation in terms of angular momentum loss. However, magnetic braking is governed by the characteristics and evolutionary state of the donor star and is thus not always present in X-ray binaries.

Magnetic braking is a phenomenon observed to be occurring in individual stars. It causes a loss of spin angular momentum in stars and forces them to decrease their rates of rotation (i.e., to "spin down"). The mechanism through which this angular momentum is lost is best understood by recalling the basic expression for the angular momentum (J) of a mass m

rotating at a distance r about an axis of rotation with tangential velocity v and rotational velocity ω_{rot}:

$$\mid \vec{J} \mid = r \cdot mv = r^2 \omega_{rot} \, . \tag{2.59}$$

From Equation 2.59, it is clear that even the smallest fraction of total mass (δm) can extract significant amounts of angular momentum from a system when escaping at a large enough radius (the classic example of a figure skater that spins fast with his arms close to his body -the axis of rotation- and then slows his rotation as he extends them out). This is the process believed to be at work that causes a magnetic braking torque in stars. As a star constantly loses small amounts of mass particles (stellar wind) from its outer atmosphere, they remain magnetically bound to the star out to very large radii before escaping.

A typical one solar-mass main-sequence star loses about of $10^{-13} \frac{M_\odot}{\mathrm{yr}}$ due to stellar winds (the exact strength and orientation of this wind is still in debate; see Warner [176] page 444, and references therein). Still, it is not the loss of this mass directly that results in a significant sink of angular momentum. In fact, without open magnetic field lines, a star's loss of angular momentum due to its wind is minute. However, it is believed that the "dynamo" effect can allow certain rapidly rotating stars to consistently generate a magnetic field in which open field lines extend out radially for several hundred solar radii. It is understood that such an arrangement of the magnetic field mostly occurs in stars with radiative cores and deep convective envelopes. Although the exact emergence of these radial magnetic field lines still remains to be explained, it is believed that they are rooted at the interface of the convective envelope and the radiative core (e.g., [62]). Fully convective stars, even with comparable magnetic activity, do not seem to produce such an arrangement of their field lines.

With magnetic field lines of significant strength extending radially, a star's stellar wind remains magnetically entrained on those lines after escaping the stellar atmosphere. The wind thus stays bound to the star and is forced to continue co-rotating with it up to some critical radius. The distance up to which stellar wind is still bound to the rotation of a star is given by the Alfvén radius. For solar-mass stars, the Alfvén radius (R_A) is estimated to be $\sim 100\, R_\odot$ from the star's axis of rotation (Warner [176]). At such large distances, the continuous loss of even insignificant amounts of mass can become a considerable sink of angular momentum for stars, as is evident from Equation 2.59. As mentioned above, for single stars this loss of angular momentum acts as a braking torque, slowing a star's rotation.

When developing an equation for the angular momentum lost through magnetic braking, it is common to use the correlation between equatorial rotation velocity and age based on main sequence stars with approximately one solar mass. Using the results of Kraft [83], Rappaport et al. [134] express this relationship as

$$v_e \approx f \times 10^{14} t_\circ^{-\frac{1}{2}} \, \frac{[\mathrm{cm}]}{[\mathrm{s}]} \, , \tag{2.60}$$

where $t_\circ$ is the time elapsed since the star settled onto the main sequence and f is a constant that lies in the range from ~ 0.75 to 1.75. From the above equation, a braking torque can be deduced (e.g., [173]) that Rappaport et al. [134] state as

$$\tau_{mb} \approx -0.5 \times 10^{-28} \left(\frac{k}{f}\right)^2 M R^4 \omega_{star}^3 \text{ [dyn] [cm]} , \tag{2.61}$$

with k being the structure constant of the star that yields the stellar moment of inertia $I = k^2 M R^2$, and ω_{star} represents the rotational angular velocity of the star. Also, a typical value for f is 1.14707 (e.g., [50]).

In the case of close interacting binary systems, the mutual gravity of the stars causes tidal forces that constrain their rotation about their own axis. This enforces a co-rotation of the components with the orbit (i.e., $\omega_{star} = \omega_{orbital}$, where $\omega_{orbital}$ is the Keplerian angular velocity of the system). The stars are "phase-locked" and thus forced to keep rotating at the orbital angular velocity. A phase-locked star that loses angular momentum through magnetic braking cannot simply decrease its rate of rotation. In consequence, it will "tap into" the angular momentum contained in the orbital motion of the binary in order to be able to maintain its rotational velocity. In other words, the loss of a star's angular momentum due to the magnetic stellar wind is coupled to a decrease of the system's orbital angular momentum. The actual mechanism how the angular momentum is redistributed is very poorly understood. The consensus is that it occurs through the donor star's interaction with the accretion disk.

Assuming circular orbits, one can express Equation 2.61 in terms of the Keplerian angular velocity of the binary. Using $f = 1.14707$, the orbital angular momentum lost by a X-ray binary due to the effects of magnetic braking is

$$\left(\frac{\partial J}{\partial t}\right)_{MB} = -3.8 \times 10^{-29} \frac{G^{\frac{3}{2}}}{a^{\frac{9}{2}}} M_T^{\frac{3}{2}} k^2 M_2 R_2^4 . \tag{2.62}$$

Rappaport et al. [134] have a more general equation[1],

$$\left(\frac{\partial J}{\partial t}\right)_{MB} = -3.8 \times 10^{-30} M_2 R_\odot^4 \left(\frac{R_2}{R_\odot}\right)^\gamma \omega^3 \, [dyn] \, [cm] , \tag{2.63}$$

where different values for the index γ are explored by them. As adopted by Nelson et al. [106] and others, the `MESA` code uses $\gamma = 3$, and this is the value used throughout this thesis.

In order to use Equation 2.62, one has to compute the coefficient k^2. For a sphere of constant density, the moment of inertia is known to be

$$I = \frac{2}{5} M R^2 = \frac{8}{15} \pi \rho R^5 , \tag{2.64}$$

[1] Although this equation is more general, it assumes that $k^2 = 0.1$. The more general equation would be $\left(\frac{\partial J}{\partial t}\right)_{MB} = -3.8 \times 10^{-29} k^2 M_2 R_\odot^4 \left(\frac{R_2}{R_\odot}\right)^\gamma \omega^3$.

so the moment of inertia of a thin spherical shell is given by

$$dI = \frac{8}{3}\pi\rho R^4 dR = \frac{2}{3}\left(4\pi\rho R^2 dR\right) R^2 = \frac{2}{3}\left(dM\right) R^2 \,. \tag{2.65}$$

The moment of inertia of the whole star can then be written as

$$I = \frac{2}{3}\int_0^M r^2 \,\mathrm{d}m \,, \tag{2.66}$$

so comparing with $I = k^2 M R^2$, one finds

$$k^2 = \frac{2}{3MR^2}\int_0^M r^2 \,\mathrm{d}m \,. \tag{2.67}$$

It is then possible to use the shell approximation of the star to evaluate Equation 2.67 (see Section 2.1.2 and Figure 2.1 for more details about shells). Thus, since one can assume the core to be a perfect sphere, one gets

$$k^2 \approx \frac{1}{MR^2}\left(\frac{2}{3}\sum_{i=1}^{n_z-1} r_i r_{i+1}\Delta m_i + \frac{2}{5}\Delta m_{n_z} r_{n_z}^2\right) , \tag{2.68}$$

where n_z is the total number of shells, r_i is the radius from the center of the star to the surface of shell i (thus, $r_i r_{i+1}$ is an approximation for r^2 at the center of shell i), and Δm_i is the mass of shell i. Therefore, Equation 2.63 becomes

$$\left(\frac{\partial J}{\partial t}\right)_{MB} = -3.8\times10^{-29}\,\frac{R_\odot^4}{R_2^2}\left(\frac{R_2}{R_\odot}\right)^{\gamma}\omega^3\left(\frac{2}{3}\right)\int_0^M r^2\,\mathrm{d}m \tag{2.69}$$

$$\therefore \left(\frac{\partial J}{\partial t}\right)_{MB} \approx -3.8\times10^{-29}\frac{R_2^{\gamma-2}}{R_\odot^{\gamma-4}}\omega^3\left(\frac{2}{3}\sum_{i=1}^{n_z-1} r_i r_{i+1}\Delta m_i + \frac{2}{5}\Delta m_{n_z} r_{n_z}^2\right) . \tag{2.70}$$

Magnetic Braking for Convective Stars

The widely accepted view is that the mechanism of magnetic braking does not take place when a star is fully convective. As discussed above, the arrangement of magnetic field lines differs considerably for such stars, and no free radial lines exist. This, combined with considerably diminished stellar winds, supports the position that magnetic braking does not apply to fully convective stars (see [176, 64] for a discussion and references). The mass below which single stars are fully convective occurs at $\simeq 0.25\,M_\odot$ according to the models produced for this work. For X-ray binary systems, donor stars that are continuously losing mass can eventually undergo a structure change and become fully convective. Accordingly, this point should mark the end of magnetic braking for the corresponding system. The dividing line

when mass-losing stars become fully convective is a function of their nuclear evolution and mass loss history. Thus, if during the evolution of a specific X-ray binary track for this work the donor star becomes convective, then the angular momentum loss due to magnetic braking is discounted for the remainder of the track. The sudden cessation in magnetic braking is believed to be the cause for the so-called "period gap" of CV-like systems (see Section 2.4.1). An alternative view and discussion regarding this abrupt cease of magnetic braking on the boundary to fully convective stars is given by Andronov et al. [3].

Furthermore, something similar occurs for more massive donor stars. If the donor star mass lies in the range $0.25\,M_\odot \lesssim M_2 \lesssim 1.4\,M_\odot$, then the donor has a convective zone in its outer layers that allows for magnetic braking. However, around $1.4\,M_\odot$, the outer layers of the star are fully radiative, and for larger masses, a convective zone is present closer to the core of the star, whereas the rest of the star is radiative. In this case, i.e. for $M_2 \gtrsim 1.4\,M_\odot$, magnetic braking cannot occur, and again, this implies that for X-ray binary systems with donors heavier than $1.4\,M_\odot$, angular momentum loss due to magnetic braking is not allowed.

2.2.4 Changes in Orbital Separation

Any loss of angular momentum from a binary system (be it matter escaping the system, magnetic braking, gravitational radiation, or some other mechanism) forces the system to respond to this loss. The system needs to reflect its new (lower) total angular momentum through a decreased orbital separation and/or angular velocity (see Section 2.2.3). However, for semi-detached binary systems, it is not only a loss of angular momentum from the system that can cause changes in the orbital separation. By conservation of angular momentum (when no angular momentum loss is present), a redistribution of mass also yields a change in a binary's orbital separation. To show this, one can start by re-stating Equation 2.43, the total orbital angular momentum J of a system consisting of two orbiting point masses M_1 and M_2 with total mass $M_T = M_1 + M_2$, and an orbital separation a:

$$J^2 = G\frac{M_1^2 M_2^2}{M_T} a\,. \tag{2.71}$$

In accordance with the above equation, conservation of angular momentum for such a system with regard to a redistribution of mass can be written as

$$J^2 = G\frac{M_1^2 M_2^2}{M_T} a = \bar{J}^2 = G\frac{\bar{M}_1^2 \bar{M}_2^2}{M_T} \bar{a}\,, \tag{2.72}$$

where the bars denote the corresponding values after some amount of mass (δM) has been transferred from mass 2 to mass 1 (the sum of the masses $M_T = M_1 + M_2$ remains constant). Rewriting the above equation yields

$$\frac{a}{\bar{a}} = \frac{M_1^2 M_2^2}{\bar{M}_1^2 \bar{M}_2^2}\,, \tag{2.73}$$

and substituting for $\bar{M}_1$ and $\bar{M}_2$ and then solving for $\bar{a}$ gives

$$\bar{a} = \frac{(M_1 + \delta M)^2 (M_2 - \delta M)^2}{M_1^2 M_2^2} a = \left(1 + \frac{\delta M}{M_1}\right)^2 \left(1 - \frac{\delta M}{M_2}\right)^2 a\,. \tag{2.74}$$

From the above equation, it can be seen that a redistribution of mass in a binary leads to changes in the orbital separation. In fact, the transfer of mass from the lower to the higher mass ($\bar{M}_1 = M_1 + \delta M$ and $\bar{M}_2 = M_2 - \delta M$, with $M_1 > M_2$) results in a widening of the orbit ($\bar{a} > a$), and vice-versa. A detailed proof of this result is given in Appendix C.3 of Goliasch [50]. It can be understood qualitatively by realizing that for $M_1 > M_2$, the center of mass is closer to M_1. A transfer of some mass δM from M_2 to M_1, therefore, reduces the angular momentum of the shifted mass. In accordance with conservation of total angular momentum, an increase in orbital separation is then inevitable to compensate for the reduction in angular momentum of δM.

In the case of X-ray binary systems, the combined effects of actual momentum losses and mass re-distributions have to be considered when modeling a system's orbital mechanics over time. Thus, the remainder of this section will derive an expression for changes in the orbital separation, taking all of the above into account. Starting from Equation 2.71, one can express the change of total angular momentum over time by

$$2\frac{\dot{J}}{J} = 2\frac{\dot{M}_1}{M_1} + 2\frac{\dot{M}_2}{M_2} + \frac{\dot{a}}{a} - \frac{\dot{M}_T}{M_T}\,. \tag{2.75}$$

For X-ray binary systems, the change of total angular momentum is the sum of angular momentum loss by the mechanisms discussed in the previous section:

$$\dot{J} = \left(\frac{\partial J}{\partial t}\right)_{GR} + \left(\frac{\partial J}{\partial t}\right)_{MB} + \left(\frac{\partial J}{\partial t}\right)_{\dot{M}}\,. \tag{2.76}$$

The first term on the right-hand side in the above equation represents the angular momentum carried away by gravitational radiation (as given by Equation 2.58), the second term represents the angular momentum lost through magnetic braking (as given by Equation 2.63), and the third term stands for the angular momentum carried away by mass leaving the system (as given by Equation 2.47). Combining Equations 2.75 and 2.76 and solving for $\dot{a}$ yields the desired expression for changes in the orbital separation:

$$\frac{\dot{a}}{a} = -2\left(\frac{\dot{M}_1}{M_1} + \frac{\dot{M}_2}{M_2}\right) - \frac{\dot{M}_T}{M_T} + \frac{2}{J}\left(\frac{\partial J}{\partial t}\right)_{GR} + \frac{2}{J}\left(\frac{\partial J}{\partial t}\right)_{MB} + \left(\frac{\partial J}{\partial t}\right)_{\dot{M}}\,. \tag{2.77}$$

The MESA code handles this computation by first computing $\dot{J}$ according to Equation 2.76, and then, it evaluates

$$J = J_{prev} + \dot{J}\, dt\,, \tag{2.78}$$

where J_{prev} is the orbital angular momentum in the previous step in the evolution and dt is the time step from the previous step to the actual step. Equivalently,

$$M_2 = M_{2,prev} + \dot{M}_2\, dt\,, \tag{2.79}$$

and

$$M_1 = M_{1,prev} + \dot{M}_1\, dt\,, \tag{2.80}$$

where $\dot{M}_2$ is computed according to Equation 2.41 and $\dot{M}_1 = -\beta \dot{M}_2$ (recall Equation 2.52). Finally, the orbital separation is computed using Equation 2.71:

$$a = \left(\frac{J}{M_1 M_2}\right)^2 \frac{(M_1 + M_2)}{G}\,. \tag{2.81}$$

2.3 Neutron Stars Properties

So far, this thesis has explored full evolutionary models. Indeed, computing the evolution of standard main-sequence stars has become fairly straightforward with the advancement of computer codes such as the MESA code. Also, the dynamics of binary systems as described in the previous section are relatively well understood. When it comes to neutron stars, building a computer code that would calculate their evolution has still not been done. In fact, our knowledge of neutron stars is quite limited. Neutron stars were predicted theoretically by L. D. Landau in the 1930s, but there is still a lot of unknown physics related to them (see Lipunov [91] or Shapiro & Teukolsky [150] for a general introduction). In particular, determining the composition of neutron stars and their equation of state is a very active field of research. This issue is discussed in Section 2.3.2.

Given the small size and the high gravitational potential of neutron stars, a neutron star evolution code would require a careful analysis of general relativity. Fortunately, knowing the exact structure of a neutron star would not give us additional information and change our final results significantly concerning X-ray binary evolution. However, there are some properties of neutron stars that must still be taken into account because of their impact on X-ray binary evolution. In the following sections, the theory regarding these properties is developed.

2.3.1 Eddington Limit

In his 1926 book, *The Internal Constitution of the Stars*, Arthur S. Eddington postulated that stars have a critical luminosity due to radiation pressure (see Eddington [38]). We

will examine this critical luminosity from first principles (see [93, 126, 143, 150, 101, 91] for standard textbook discussion). Radiation pressure can be written as

$$P_{rad} = \frac{1}{3} a T^4 \,, \tag{2.82}$$

which implies that

$$dP_{rad} = \frac{4}{3} a T^3 dT \,. \tag{2.83}$$

In Section 2.1.1, it has been found that the energy transport equation (Equation 2.11) for radiation (see Equation 2.16) can be written as

$$\frac{dT}{dm} = -\frac{3\kappa}{64\pi^2 a c r^4} \left(\frac{L_m}{T^3} \right) \,, \tag{2.84}$$

which can be translated into the Eulerian scheme as

$$\frac{dT}{dr} = -\frac{3}{4ac} \frac{\kappa\rho}{T^3} \frac{L_m}{4\pi r^2} \,. \tag{2.85}$$

Substituting dT from Equation 2.83 into Equation 2.85 yields

$$\frac{3}{4} \frac{1}{aT^3} \frac{dP_{rad}}{dr} = -\frac{3}{4ac} \frac{\kappa\rho}{T^3} \frac{L_m}{4\pi r^2} \,. \tag{2.86}$$

This equation can be divided by the equation of hydrostatic equilibrium (Equation 2.6) to find

$$\frac{dP_{rad}}{dP} = \frac{\kappa L_m}{4\pi c G m} \,. \tag{2.87}$$

Since $dP = dP_{rad} + dP_{gas}$, and since both P_{rad} and P_{gas} decrease outward, it is always true that $dP_{rad} < dP$, and consequently, $\frac{dP_{rad}}{dP} < 1$. Therefore, Equation 2.87 becomes

$$L_m < \frac{4\pi c G m}{\kappa} \,, \tag{2.88}$$

and for the surface of the star, one gets

$$L < \frac{4\pi c G M}{\kappa} \,. \tag{2.89}$$

The right-hand side of Equation 2.89 is the critical luminosity that Eddington came up with, hence the definition of L_{edd}:

$$L_{edd} \equiv \frac{4\pi c G M}{\kappa} \,. \tag{2.90}$$

Note that for relativistic objects such as neutron stars or black holes, it is possible to account for general relativistic effects (e.g., [116, 150]), and one obtains

$$L_{edd} = \frac{4\pi c G M}{\kappa} \left(1 - \frac{2GM}{Rc^2}\right)^{-\frac{1}{2}} . \tag{2.91}$$

Now, the goal is to see why this critical luminosity is important in X-ray binary evolution. In general, for steady *spherical* accretion onto a neutron star (neglecting any magnetic field), one has

$$L_1 = \frac{G M_1 \dot{M}_1}{R_1} , \tag{2.92}$$

This assumes that all the energy coming from the accreting gas is radiated at the same rate as it is liberated. One can then define the efficiency of radiative emission (as Shapiro & Teukolsky [150] call it), or in other words, the accretion efficiency (as Kolb [81] calls it). It can be seen as the efficiency of converting gravitational energy (the rest mass energy of the accreted matter) into heat. The accretion efficiency is defined as

$$\xi \equiv \frac{L}{\dot{M} c^2} , \tag{2.93}$$

so for a neutron star, one can use Equation 2.92 to estimate the efficiency as being

$$\xi = \frac{G M_1}{R_1 c^2} . \tag{2.94}$$

For a typical neutron star, one has $\xi \sim 0.1$ (e.g., [150, 143]). For a white dwarf, the efficiency is $\xi \sim 3 \times 10^{-4}$ (e.g., [143, 93]), and for a black hole, it can be from $\xi \sim 0.06$ to $\xi \sim 0.3$ (e.g., [143, 81, 149, 123]), where it is smaller for Schwarzschild black holes and larger for Kerr black holes. Now, the definition of the accretion efficiency (Equation 2.93) and the Eddington luminosity (Equation 2.91) can be combined to find a critical accretion rate for neutron stars:

$$\dot{M}_{edd} = \frac{L_{edd}}{\xi c^2} = \frac{4\pi G M_1}{c \kappa \xi} \left(1 - \frac{2GM_1}{R_1 c^2}\right)^{-\frac{1}{2}} . \tag{2.95}$$

It can finally be simplified using Equation 2.94:

$$\dot{M}_{edd} = \frac{4\pi G M_1}{c \kappa \xi} \left(1 - 2\xi\right)^{-\frac{1}{2}} . \tag{2.96}$$

Let us recall that the mass that is transferred onto the neutron star comes from the outer layers of the donor star. Thus, the opacity of this material comes from the Thomson scattering of the material on the surface of the donor star, so one can write (e.g., [79])

$$\kappa = \frac{8\pi}{3} \frac{r_e^2}{\mu_e m_u} , \tag{2.97}$$

where r_e is the classical electron radius, μ_e is the mean molecular weight per free electron, and m_u is the atomic mass constant. Typically, for a fully ionized gas, one can approximate μ_e to be (e.g., [79])

$$\mu_e = \frac{2}{1+X}\,, \tag{2.98}$$

where X is the mass fraction of hydrogen (taken at the surface of the donor star in our case). Thus, one can rewrite

$$\kappa \cong 0.20(1+X)\,\mathrm{cm}^2\,\mathrm{g}^{-1}\,. \tag{2.99}$$

One thus gets the final expression for the critical mass-transfer rate:

$$\dot{M}_{edd} = \frac{4\pi G M_1}{c\kappa_{const}(1+X)\xi}\,(1-2\xi)^{-\frac{1}{2}}\,, \tag{2.100}$$

where one defines $\kappa_{const} \equiv \frac{4\pi r_e^2}{3m_u} \cong 0.20\,\mathrm{cm}^2\,\mathrm{g}^{-1}$. Although the value of $\dot{M}_{edd}$ changes throughout the evolution of X-ray binaries, it is important to remember for the rest of this thesis that it is of the order of $10^{-8}\,M_\odot/\mathrm{yr}$.

So, the critical Eddington luminosity limits the amount of mass that the donor star can successfully transfer to the neutron star. In other words, the Eddington limit reduces the mass-transfer fraction β introduced in Section 2.2.3.1. Since $\beta \equiv -\dot{M}_1/\dot{M}_2$ and since one wants $\dot{M}_{1,max} = \dot{M}_{edd}$, one can write

$$\beta = \beta_{edd} = \min\left\{\beta_{max}, \frac{\dot{M}_{edd}}{|\dot{M}_2|}\right\}\,, \tag{2.101}$$

where the value of the maximum mass-transfer fraction, β_{max}, is discussed in Section 2.4.4.

2.3.2 Binding Energy

Another important aspect that comes into play when studying X-ray binaries is the binding energy of neutron stars. It has been pointed out by Alécian & Morsink [2] and by Bagchi [7] that the binding energy of neutron stars and general relativity (see Lavagetto et al. [89]) might have an effect on the evolution of LMXBs and IMXBs.

The binding energy of a neutron star is defined as the difference between its baryonic mass (the rest mass of the individual baryons that make up the neutron star) and its gravitational mass (at infinity):

$$BE = (M_B - M_G)\,c^2\,. \tag{2.102}$$

In more detail, the gravitational mass of a neutron star is given by

$$M_G = \int \rho(r) r^2 dr d\Omega = \int_0^R 4\pi r^2 \rho(r) dr\,, \tag{2.103}$$

where $d\Omega = \sin\theta\, d\theta d\phi$. The right-most equality assumes a spherically symmetric neutron star, which is a very good approximation for such compact objects. It is important to note that the gravitational mass is the one measured observationally and the one used in studies of neutron star mass distribution (e.g., [80, 113, 165, 169, 148]). However, since a neutron star is a relativistic object, one should consider Schwarzschild geometry. That way, one can define the proper mass of a neutron star to be

$$M_P = \int e^{\frac{\lambda}{2}} \rho r^2 dr d\Omega \,, \tag{2.104}$$

where $e^{\frac{\lambda}{2}} = \left(1 - \frac{2Gm_G(r)}{rc^2}\right)^{-\frac{1}{2}}$ is the square root of the radial component of the Schwarzchild metric tensor (Landau-Lifshitz notation, [86]). Thus, the proper mass becomes

$$M_P = 4\pi \int_0^R \left(1 - \frac{2Gm_G(r)}{rc^2}\right)^{-\frac{1}{2}} \rho(r) r^2 dr \,, \tag{2.105}$$

and the total number of baryons becomes

$$N_B = 4\pi \int_0^R \left(1 - \frac{2Gm_G(r)}{rc^2}\right)^{-\frac{1}{2}} n(r) r^2 dr \,, \tag{2.106}$$

where $n(r)$ is the particle number density. The definition of the baryonic mass of a neutron star immediately follows:

$$M_B = 4\pi m_B \int_0^R \left(1 - \frac{2Gm_G(r)}{rc^2}\right)^{-\frac{1}{2}} n(r) r^2 dr \,, \tag{2.107}$$

where m_B is the mass of a baryon. For a general discussion on the baryon number of a star and of binding energy, see Glendenning [49], and for a general discussion of Schwarzchild geometry, refer to any standard general relativity textbook (e.g., [28, 175, 102]).

Now, let us emphasize why the binding energy is important in X-ray binary evolution. Physically, when mass is transferred from the donor star to the neutron star, the neutron star accretes baryonic mass, so

$$M_{acc} = -\beta_{edd} \dot{M}_2 dt = dM_B \,, \tag{2.108}$$

i.e., the accreted mass by the neutron star is equal to the change in its baryonic mass. Using the definition of binding energy (Equation 2.102), one gets

$$M_{acc} = dM_B = dM_G + d\left(\frac{BE}{c^2}\right) . \tag{2.109}$$

Since astronomers measure $M_1 = M_G$, every time the neutron star accretes some mass dM_B through X-ray binary evolution, one has to subtract the change in binding energy $d\left(\frac{BE}{c^2}\right)$ to determine the change in gravitational mass of the neutron star (dM_G).

If one knows the equation of state of a neutron star (i.e., $\rho(r)$ and $n(r)$), it is then possible to evaluate Equations 2.103 and 2.107 to find the baryonic and gravitational mass, and consequently, the binding energy. However, finding equations of state for neutron stars is still a very active field of research because of our poor understanding of matter at high density. However, there are many prospective equations of state for neutron stars (see Lattimer & Prakash [87], and references therein) that allow us to estimate the binding energy. In particular, Lattimer & Prakash [87] came up with an approximate expression for the binding energy that fits the most common neutron-star equations of state:

$$\frac{BE}{M_G c^2} = \frac{6\epsilon}{5\,(2-\epsilon)}\,, \tag{2.110}$$

where $\epsilon \equiv \frac{GM_G}{Rc^2}$. Note that this ϵ is the same factor as in Equation 2.94. Figure 2.4 shows this fit (black curve) and many prospective equations of state, from standard ones (e.g., AP4) to more exotic equations of state (e.g., GS1). The fit is better for the more standard equations of state, and this is fine since most of the exotic equations of state have been ruled out by the discovery of a $\sim 2\,M_\odot$ neutron star (see Figure 2.5).

Now, in order to use Equation 2.109 with Equation 2.110, it would be useful to find the ratio $\frac{dM_G}{dM_B}$ as a function of the factor ϵ. In general, let us assume there exists a function

$$f(\epsilon) \equiv \frac{BE}{M_G c^2} \tag{2.111}$$

for the binding energy as a function of ϵ. Then, rearranging Equation 2.111 and taking the differential, one obtains

$$d\left(\frac{BE}{c^2}\right) = dM_G\, f(\epsilon) + M_G\, df(\epsilon)\,, \tag{2.112}$$

so Equation 2.109 becomes

$$dM_B = dM_G \left(1 + f(\epsilon) + \left(\frac{dM_G}{M_G}\right)^{-1} df(\epsilon)\right)\,, \tag{2.113}$$

where by the definition of ϵ, one has

$$\frac{dM_G}{M_G} = \frac{d\epsilon}{\epsilon}\,, \tag{2.114}$$

hence

$$dM_B = dM_G \left(1 + f(\epsilon) + \epsilon\frac{df}{d\epsilon}\right) \tag{2.115}$$

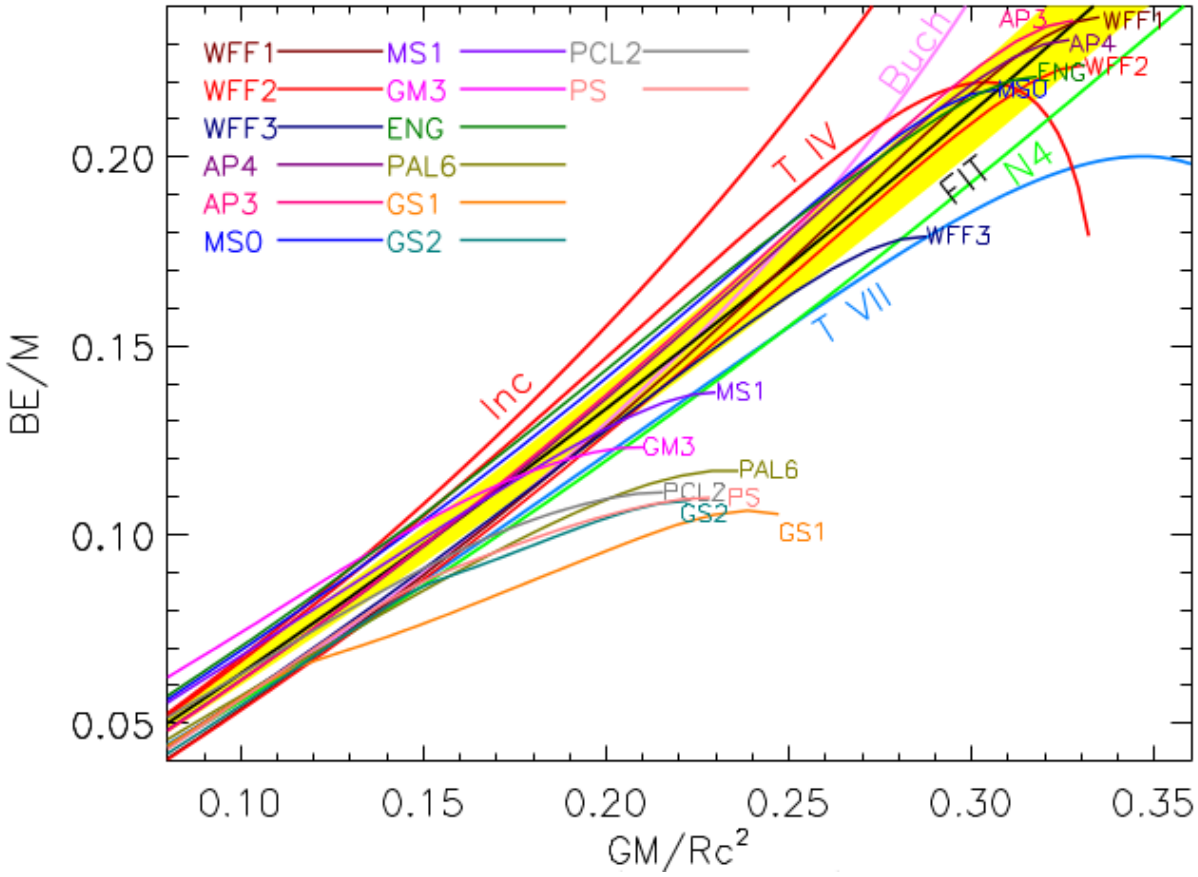

Figure 2.4: Binding energy of a neutron star as a function of $\epsilon \equiv \frac{GM_G}{Rc^2}$ for different prospective equations of state (taken from Lattimer [88], but originally in Lattimer & Prakash [87]; see these articles for more details).

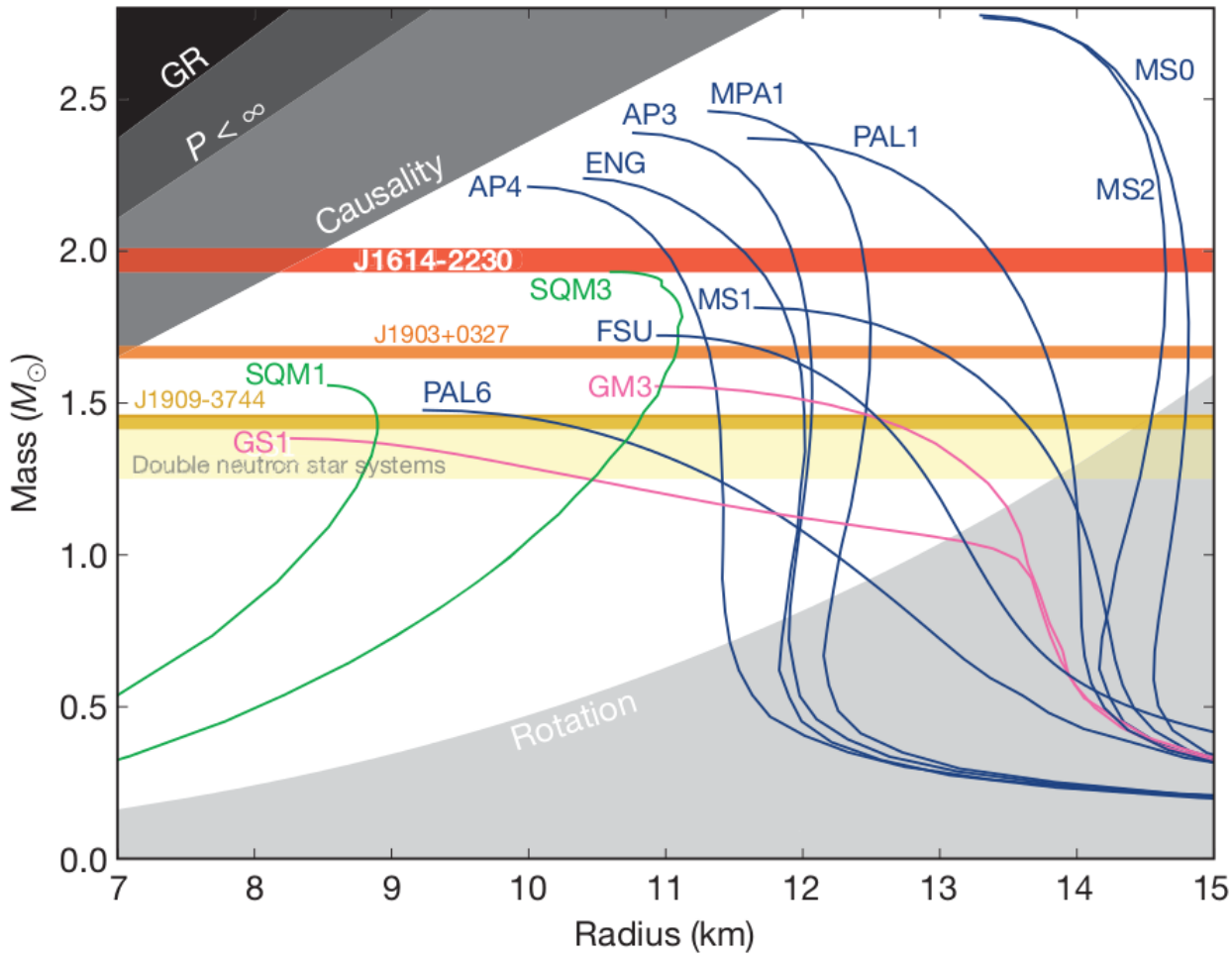

Figure 2.5: Mass of a neutron star versus its radius for different prospective equations of state (taken from Demorest et al. [35]). The mass of J1909-3744 (yellow band), J1903+0327 (orange band), and J1614-2230 (red band) have been added to the graph. The discovery of J1614-2230 rules out many equations of state such as MS1, FSU, GM3, PAL6, GS1, and SQM1. See Demorest et al. [35] for more details.

$$\therefore \frac{dM_G}{dM_B} = \left(1 + f(\epsilon) + \epsilon \frac{df}{d\epsilon}\right)^{-1} . \tag{2.116}$$

If one takes $f(\epsilon)$ to be Equation 2.110, one can compute the right hand side of Equation 2.116 and find

$$\frac{dM_G}{dM_B} = \frac{5\,(\epsilon - 2)^2}{20 + 4\epsilon - \epsilon^2} . \tag{2.117}$$

This equation can now be used to correct the accreted mass by the neutron star throughout its evolution.

Lavagetto et al. [89] consider an extra relativistic effect that would change the accreted gravitational mass, that is the intrinsic angular momentum J:

$$dM_G = \left(\frac{\partial M_G}{\partial M_B}\right)_J dM_B + \left(\frac{\partial M_G}{\partial J}\right)_{M_B} dJ . \tag{2.118}$$

The first partial derivative of Equation 2.118 is precisely what has been found earlier (Equation 2.117). The second partial derivative is due to the rotation of the neutron star, i.e.,

$$\left(\frac{\partial M_G}{\partial J}\right)_{M_B} = \frac{\omega_{NS}}{c^2}, \tag{2.119}$$

where ω_{NS} is the neutron star spin frequency.

Bagchi [7] computed models in which rotating neutron stars are considered. She found out that for $\omega_{NS} = 3000\,s^{-1}$ and for a fixed value of M_G, the proper mass of the neutron star (and consequently, the baryonic mass) would decrease by an amount of less than 1%.

Let us do some estimations regarding the angular momentum of a neutron star. Classically, one can say that for a neutron star, $J = I\omega_{NS}$ with $I \cong 2M_1R_1^2/5$ (constant density approximation). Thus,

$$\frac{\dot{J}}{J} \cong \frac{\dot{M}_1}{M_1} + \frac{2\dot{R}_1}{R_1} + \frac{\dot{\omega}_{NS}}{\omega_{NS}} , \tag{2.120}$$

but looking at the more standard equations of state for neutron stars (such as AP4) on Figure 2.5, within a mass range of $1.4M_\odot - 2.0M_\odot$, one can clearly set $\dot{R}_1 = 0$. Since $\omega_{NS} = 2\pi/P$ and $M_1 = M_G$, one can use Equation 2.120 to find

$$\frac{\omega_{NS}}{c^2}\frac{\dot{J}}{\dot{M}_G} \cong \frac{2R_1^2\omega_{NS}^2}{5c^2}\left(1 - \frac{M_1}{\dot{M}_1}\frac{\dot{P}}{P}\right) . \tag{2.121}$$

It is known that millisecond pulsars can have very small period derivatives such as $\dot{P} \lesssim 10^{-18}$ (e.g., [84]). If one assumes that $\dot{P}$ is so small that $\frac{M_1}{\dot{M}_1}\frac{\dot{P}}{P} \approx 0$, the maximum value that $\frac{\omega_{NS}}{c^2}\frac{\dot{J}}{\dot{M}_G}$ can take is roughly $\frac{2R_1^2\omega_{NS}^2}{5c^2}$. Taking $R_1 \approx 15\,\mathrm{km}$ (which is probably too large) and taking

$\omega_{NS} \approx 6000\,\mathrm{s}^{-1}$ (which would be a really fast millisecond pulsar), then $\frac{\omega_{NS}}{c^2}\frac{\dot{J}}{\dot{M}_G}$ would be around 3.6%. If one takes more realistic values (say $R_1 \approx 11\,\mathrm{km}$ and $\omega_{NS} \approx 3000\,\mathrm{s}^{-1}$), then $\frac{\omega_{NS}}{c^2}\frac{\dot{J}}{\dot{M}_G}$ drops to $\approx 0.5\%$. This indicates that the term $\left(\frac{\partial M_G}{\partial J}\right)_{M_B} dJ$ of Equation 2.118 is probably negligible for this work.

Angular Momentum Loss due to Neutron Star Properties

Alécian & Morsink [2] and Lavage to et al. [89] mention in their article that the binding energy of neutron stars has an additional effect on X-ray binaries. Indeed, the mass defect due to binding energy can be seen as mass leaving the system, and one can thus expect that this leads to angular momentum loss as seen in Section 2.2.3.1. To see this, let us recall that $dM_G = dM_1$ and $dM_B = -\beta_{edd}\, dM_2$ (Equation 2.108), and let us rewrite Equation 2.118 (without the term at the far right for the reasons given in the previous paragraph):

$$dM_1 = -\frac{dM_G}{dM_B}\,\beta_{edd}\, dM_2\,. \tag{2.122}$$

The term $\frac{dM_G}{dM_B}$ can then be seen as reducing the mass-transfer fraction, β. Let us then define

$$\beta_{BE} \equiv \frac{dM_G}{dM_B}\,, \tag{2.123}$$

which can be computed according to Equation 2.117. Then, one has

$$\dot{M}_1 = -\beta_{BE}\beta_{edd}\dot{M}_2\,, \tag{2.124}$$

so since $\beta \equiv -\dot{M}_1/\dot{M}_2$, one finally obtains

$$\beta = \beta_{BE}\beta_{edd}\,. \tag{2.125}$$

Recalling that β modifies the angular momentum loss due to mass loss (see Equation 2.53), it is obvious that, similarly to the Eddington limit, the binding energy of neutron stars reduces the angular momentum of X-ray binary systems.

Neutron Star Radius

The radius of the neutron star has already been encountered in some equations (e.g., Equation 2.95) and it will come back in the theory of Section 3.1. As just seen, the radius of neutron stars has yet to be determined. There are many candidates to the equation of state and they all have different mass-radius relationships. However, looking at some of the equations of state in Figure 2.5, it is fair to claim that the radius is always close to being constant for a mass range of $1.4\,M_\odot - 2.0\,M_\odot$. For this work, it has been decided that R_1 is a constant value of $R_1 = 11.5\,\mathrm{km}$. This value is roughly an average of the two common

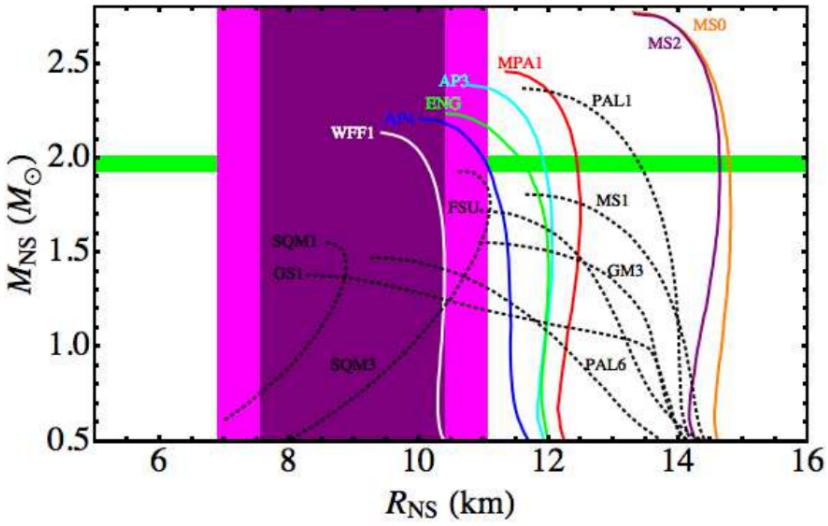

Figure 2.6: Graph of the mass of neutron stars as a function of their radius. Several possible equations of state are labeled on the graph. The purple regions show the possible radii of neutron stars at the 90% and 99% confidence levels according to Guillot et al. [53]. See their article for more details.

equations of state AP3 and AP4 (see Akmal et al. [1]). Recently, Guillot et al. [53] claimed that, at the 90% confidence level, the radius of a neutron star should be $R_{NS} = 9.1^{+1.3}_{-1.5}$ km. Their 99% confidence level reaches $\simeq 11$ km (see Figure 2.6). The value for this work of 11.5 km would thus be slightly out of their range, but changing our value of R_1 by a very small fraction would certainly not alter the final results of this thesis significantly as will be justified in Section 3.2.6.

2.4 Evolution of Low- and Intermediate-Mass X-ray Binaries

Now that the necessary theory has been discussed, one can perform computer simulations to study the evolution of LMBXs and IMXBs. The `MESA` code computes the stellar evolution of the donor star as described in Sections 2.1.1 and 2.1.2. We can also use a "test suite" called `rlo` standing for Roche lobe overflow. This suite computes all the binary system properties as described in Section 2.2. Furthermore, the suite has been improved so that it properly computes the Eddington mass transfer limit as seen in Section 2.3.1, and so that it computes the mass defect of neutron stars due to their binding energy as described in Section 2.3.2.

To carry out X-ray binary evolution using the `MESA` code, there are a number of parame-

ters that must be inputed such as the initial orbital period, the initial donor star mass, and the initial neutron star mass. This work will compute the evolution of a large portion of the $P_{orb,i} - M_{2,i}$ (initial orbital period and initial donor star mass) parameter space for LMBXs and IMXBs. In Section 2.4.2, evolutionary grids will be shown where the initial donor star mass will range from $1.0\,M_\odot$ to $4.0\,M_\odot$ and the initial orbital period will range from 10 to 250 hours.

The initial (natal) mass that should be assigned to the neutron star is something less obvious. One could investigate neutron-star natal-masses ranging from $1.0\,M_\odot$ to $1.6\,M_\odot$, but this would seriously boost the number of evolutionary tracks to compute and increase the computing time. Instead, this work will mainly use the canonical natal mass of $1.4\,M_\odot$ for the neutron star. The values of $1.2\,M_\odot$ and $1.6\,M_\odot$ will also be explored for reasons that will become clear shortly (see Section 2.4.3). The birth masses of neutron stars is an active field of research on its own, and the different channels that lead to neutron stars and to LMXBs and IMXBs make it difficult to determine a natal mass. For example, Schwab et al. [148] suggest that there exists a bimodal distribution of neutron star masses: one around $\sim 1.25\,M_\odot$ and one around $\sim 1.35\,M_\odot$. Also, Özel et al. [113] studied double neutron stars binaries, neutron stars accreting from high-mass companions, and slow pulsars to infer the birth-mass of neutron stars. They obtained a mass of $1.33 \pm 0.06\,M_\odot$ for double neutron stars and a mass of $1.28 \pm 0.24\,M_\odot$ for accreting and slow pulsars. Given that these values are still relatively uncertainty, they amply justify the choice of $1.2\,M_\odot$ and $1.4\,M_\odot$ for this thesis. The reason for investigating a natal mass of $1.6\,M_\odot$ will be justified later.

The main observables of X-ray binary systems are the orbital period and the mass of the donor star. It is for that reason that the evolution of the orbital period as a function of the mass of the donor star will be analyzed to understand the different evolutionary paths (see Section 2.4.1). Also, other observables are interesting such as the mass of the neutron star and the mass-transfer rate, and the fact that they are critical to our understanding of X-ray binary systems will soon become clear (see Section 2.4.2).

In Section 2.4.3, the end points of the evolutionary tracks will be analyzed since they can be easily compared to astronomical observations. Finally, the effect of modifying the value of the maximum mass-transfer fraction, β_{max}, will be explored in Section 2.4.4.

2.4.1 Evolutionary Tracks

Let us first look at some typical evolutionary tracks that are represented in Figure 2.7. These tracks were computed by Lin et al. [90] using an earlier version of the `MESA` code. Although a different formula for $\dot{M}_{edd}$ was used and although the binding energy of the neutron star was not considered, the qualitative behavior of these tracks remains the same.

Let us start with the curve labeled CV in Figure 2.7. This type of evolutionary path is obtained when the initial orbital period is relatively small (roughly below 20 hours). It is called a CV-like evolution because it resembles the evolution a Cataclysmic Variable (CV),

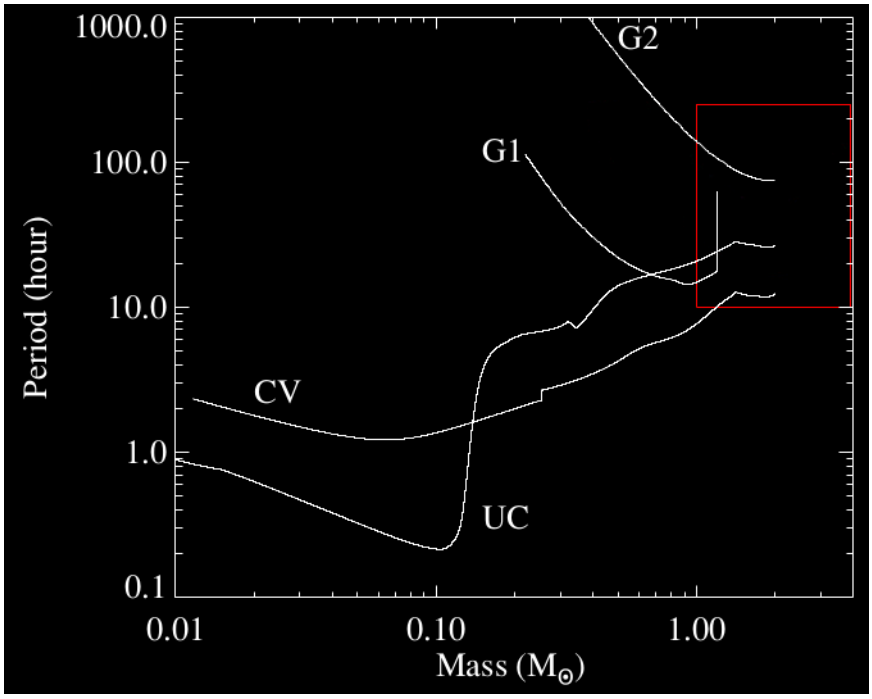

Figure 2.7: Examples of LMXB and IMXB evolutionary tracks (taken from Lin et al. [90]).

where the accretor is a white dwarf rather than a neutron star. For a thorough discussion on CV evolution, refer to Goliasch [50], and references therein. Note the presence of (a) a period gap (due to magnetic braking mentioned in Section 2.2.3.3); and, (b) the minimum period characteristic to CV evolution. After a Hubble time, the donor star has a mass of $\sim 0.01\,M_{\odot}$ and an orbital period of a few hours.

If one starts the evolution with a larger initial orbital period (curve labeled UC in Figure 2.7), one obtains an ultracompact binary. It is hard to determine what exact initial conditions lead to this type of evolution because of the sensitivity of the bifurcation (between this type of evolution and the one discussed in the next paragraph) to the initial conditions. This bifurcation becomes clearer when looking at the full evolutionary grid. With a larger initial period, the donor star tends to be more evolved at the beginning of its mass-transfer phase. The resulting evolution of ultracompacts resembles the evolution of Cataclysmic Variables, but the orbital period shrinks to much smaller minimum values on the order of a few minutes.

If one starts with an even larger initial orbital period (curves labeled G1 and G2 in Figure 2.7), the donor star will have the time to evolve to become a giant before its mass-transfer phase. With a large radius, the mass-transfer rates during this type of evolution are very high, sometimes above the Edmonton limit. In this case, the orbital period increases instead of decreasing. In the end, the donor star has no more mass to transfer and it collapses to

become a white dwarf. It then forms a so-called binary millisecond pulsar (BMSP) with the mass of the white dwarf ranging from $0.15\,M_\odot$ to $0.7\,M_\odot$ and with an orbital period above 10 hours.

2.4.2 Evolutionary Grids and More Evolutionary Tracks

Let us now look at the big picture. In Figure 2.8, one sees the results of two evolutionary grids. The red boxes delimit the set of equally-spaced initial conditions. In panel a), the computed grid includes 4,200 models which comprises 60 initial donor masses over the range of $1.0 - 4.0\,M_\odot$ and, for each of these, 70 initial orbital periods over the range of $10 - 250$ hr. In panel b), Lin et al. [90] computed ten times more models; i.e., for each initial donor masses, there were 700 initial orbital periods instead of 70. An initial mass of $1.4\,M_\odot$ was used in any case. Note that every initial condition evolved towards the three channels defined previously (CV, UC, G). The color code in both graphs indicates the logarithmic relative probability of finding an X-ray binary of a given orbital period and donor star mass at the present epoch. The red color indicates a probability 1000 times greater than the green and 10^6 times greater than the blue. That way, one can see, for example, that finding an X-ray binary in a CV-like evolution is much more probable than finding an ultracompact binary.

In general, both panels a) and b) of Figure 2.8 show the same features. Obviously, Lin et al. [90] have a denser graph because they computed the evolution of ten times more systems, but other than that, the same evolutionary paths are reproduced with similar probabilities. For now, it is thus not possible to comment on the effects of the binding energy of neutron stars on the evolution of X-ray binary systems.

Earlier, we mentioned the existence of a bifurcation between an evolution towards smaller donor star masses and smaller orbital periods (CV-like evolution and ultracompacts) and an evolution towards the formation of binary millisecond pulsars (giants). This means that for very similar initial conditions, it is possible to end up with completely different binary systems. For example, around an orbital period of 20 hours and a donor star mass of $0.2\,M_\odot$ in Figure 2.8, one can see some tracks that are very close to finishing their evolution as binary millisecond pulsars, but that rather become ultracompacts.

In Figure 2.9, one can see a plot of the mass-transfer rate as a function of the orbital period for the same evolutionary grid shown in panel a) of Figure 2.8. For $P_{orb} < 10$ hours, one is looking at mostly the CV-like evolutionary tracks and the ultracompacts. In this region, the mass-transfer rate is mostly below $\dot{M}_{edd} \sim 10^{-8}\,M_\odot/\mathrm{yr}$, albeit for orbital periods below $\simeq 0.6$ hours, there are a few peeks in the mass-transfer rate that go above $10^{-8}\,M_\odot/\mathrm{yr}$. These peaks come from the ultracompacts that reach very short minimum orbital periods. One can also note the presence of the period gap in between $P_{orb} \simeq 2.5$ hours and $P_{orb} \simeq 3$ hours (a feature common to Cataclysmic Variables).

For $P_{orb} > 10$ hours, we find that the donors largely become giants that evolve to become binary millisecond pulsars. The main difference in this region is that the mass-transfer rates

a)

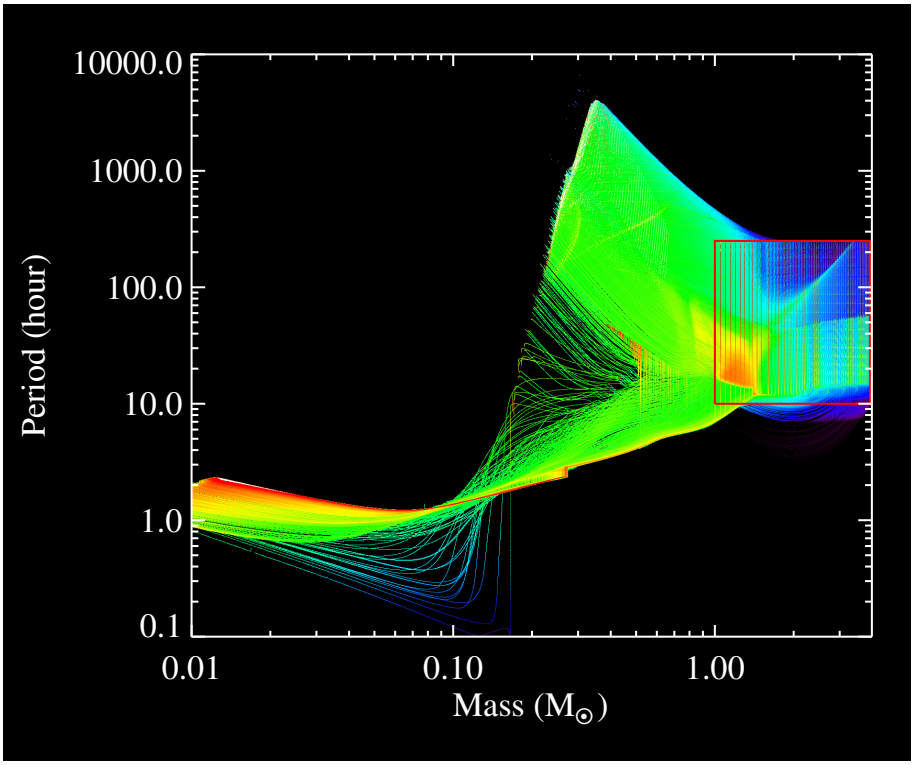

b)

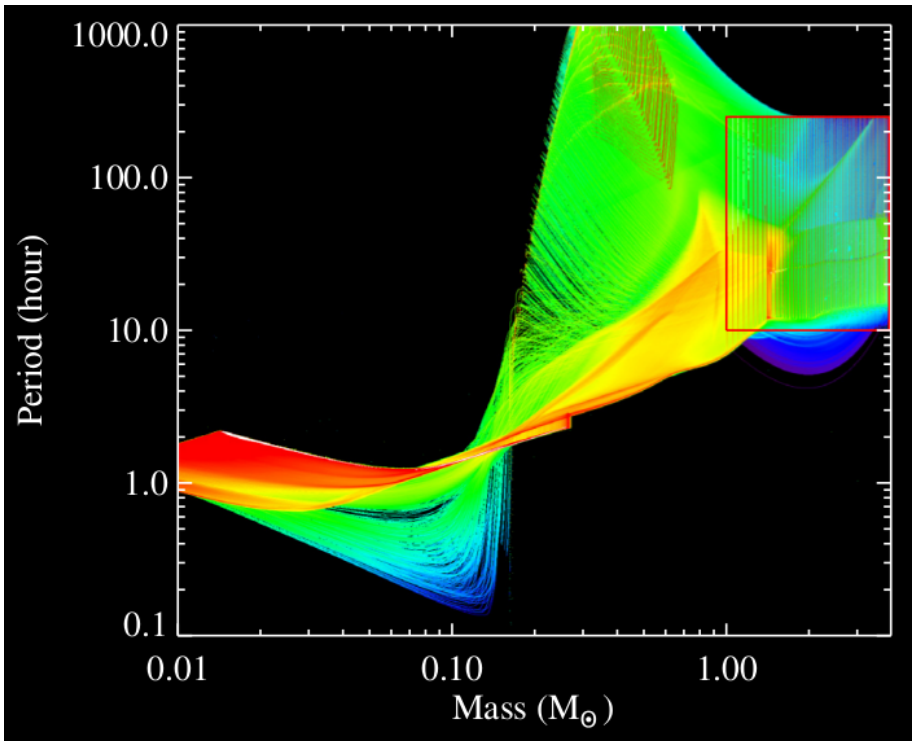

Figure 2.8: a) Evolutionary grid of $4,200$ systems using `MESA` with a correction to $\dot{M}_{edd}$ and considering the binding energy of neutron stars. b) Evolutionary grid of $42,000$ computed by Lin et al. [90] with an earlier version of `MESA`. Note that the scale of the Period-axis is different in graph a) and b).

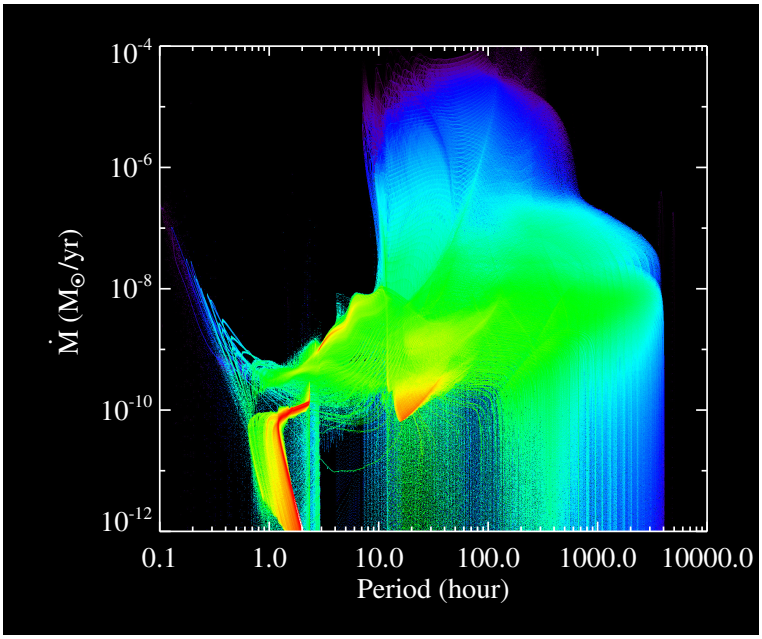

Figure 2.9: Mass-transfer rate as a function of the orbital period for the same evolutionary grid of 4,200 binary systems described in the text.

are much larger. In fact, some of the tracks reach close to $\dot{M}_2 = 10^{-4}\,M_\odot/\mathrm{yr}$, but obviously, as the color indicates, the binary systems that reach very high mass-transfer rates do not spend a lot of time in that state.

Now, let us look at a few evolutionary tracks in more detail. First, let us look at Figure 2.10. This system started as an intermediate mass donor star in a $\simeq 2$ day period. In this case, there are two main phases to the evolution. Looking at the mass-transfer rate, there is a first large peak close to 0.01 Gyrs. At this point, looking at the mass of the system, one sees that the donor star loses a lot of mass (blue curve), but the mass-transfer rate being larger than the Eddington limit, the neutron star accretes barely any mass (red curve). At this point, as long as $M_2 > M_1$, the orbital period decreases, but when the neutron star becomes more massive than the donor, the orbital period increases. Then, at $\simeq 0.06$ Gyrs, there is another enhanced mass-transfer phase that starts when the donor star has no more hydrogen at its center. For this case, however, the mass-transfer rate stays below the Eddington limit (or does not go very far above the limit). Thus, the neutron star accretes most of its mass during this phase, and given the increasing differences between M_1 and M_2, the orbital period significantly increases. Once this phase is over, the donor star burns helium in its center, and the mass fractions of oxygen and carbon become dominant. Also, the radius of the donor shrinks to $\sim 1\%$ the radius of the Sun. In fact, the donor star becomes a carbon-oxygen (CO) white dwarf.

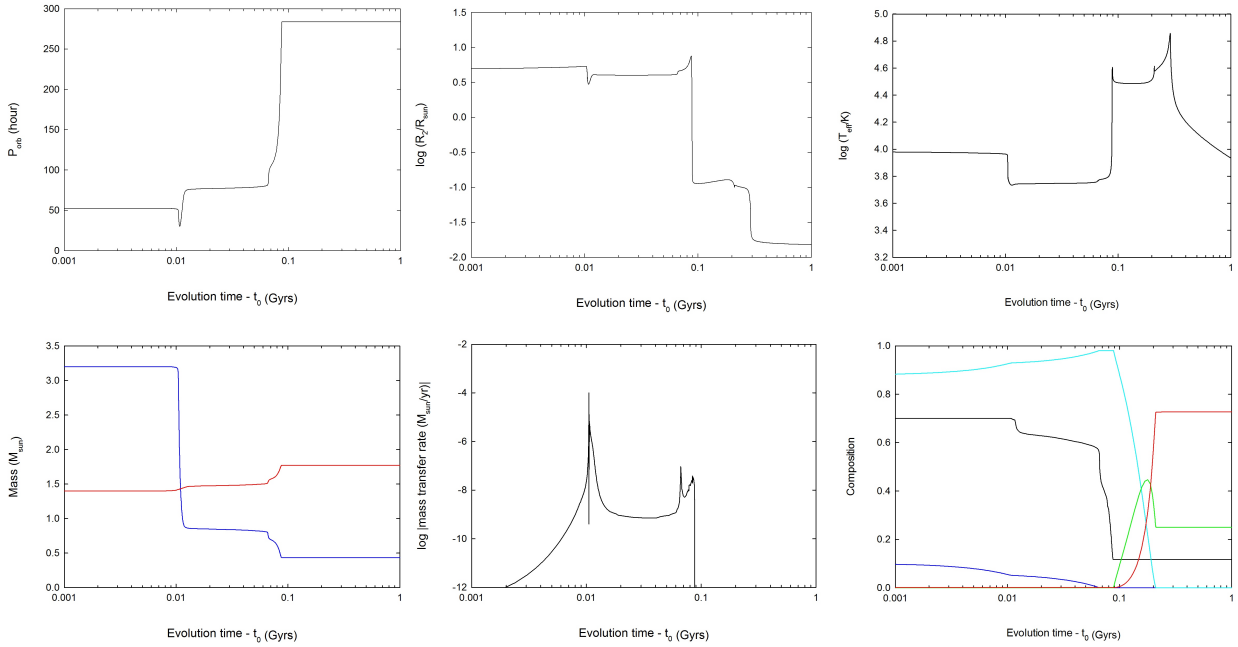

Figure 2.10: The six graphs are functions of evolution time minus t_0, where t_0 represents the moment where mass transfer starts. From left to right and from top to bottom, we have: the orbital period, the radius of the donor star, the surface temperature of the donor star, the mass of the stars in the binary system (blue for the donor star, red for the neutron star), the mass-transfer rate, and the composition of the donor star, where blue, cyan, green, red, and black represent respectively the mass fractions at the center of H, He_4, C_{12}, O_{16}, and H at the surface. The initial conditions for this evolution are $M_{1,i} = 1.4\,M_\odot$, $M_{2,i} = 3.20\,M_\odot$ and $P_{orb,i} \cong 52.48$ hours. The final values are $M_{1,f} \cong 1.77\,M_\odot$, $M_{2,f} \cong 0.43\,M_\odot$ and $P_{orb,f} \cong 283.8$ hours.

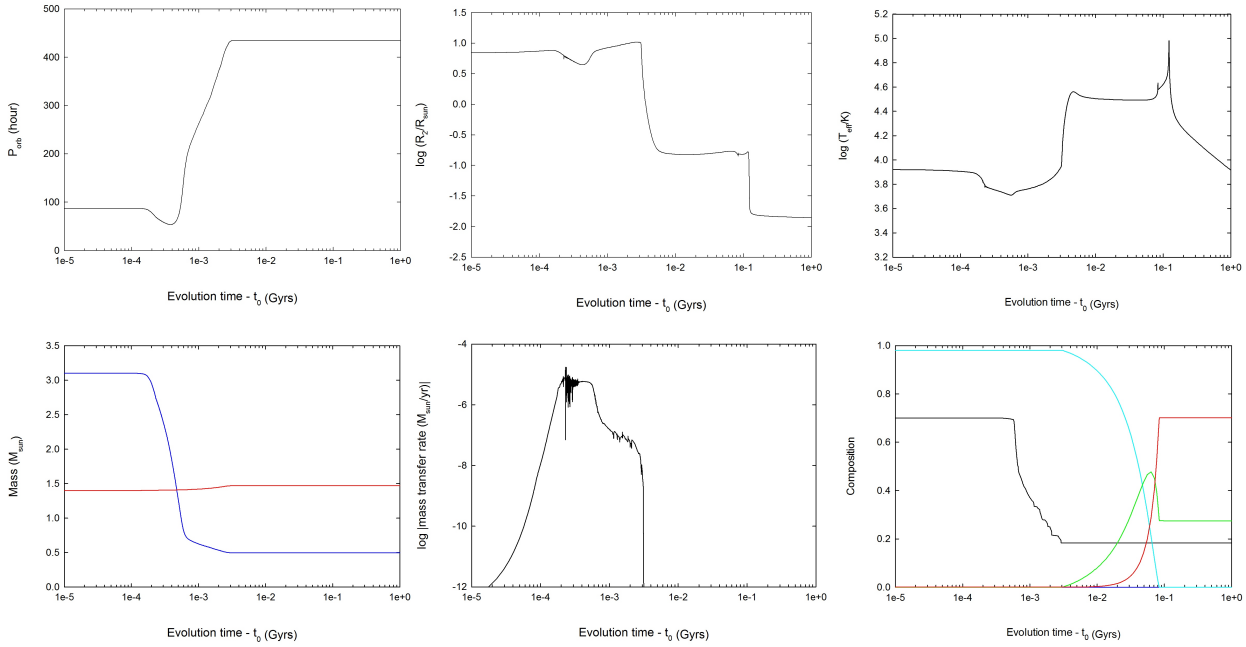

Figure 2.11: Same description for the graphs as for Figure 2.10. The initial conditions for this evolution are $M_{1,i} = 1.4\,M_\odot$, $M_{2,i} = 3.10\,M_\odot$ and $P_{orb,i} \cong 87.10$ hours. The final values are $M_{1,f} \cong 1.47\,M_\odot$, $M_{2,f} \cong 0.50\,M_\odot$ and $P_{orb,f} \cong 434.2$ hours.

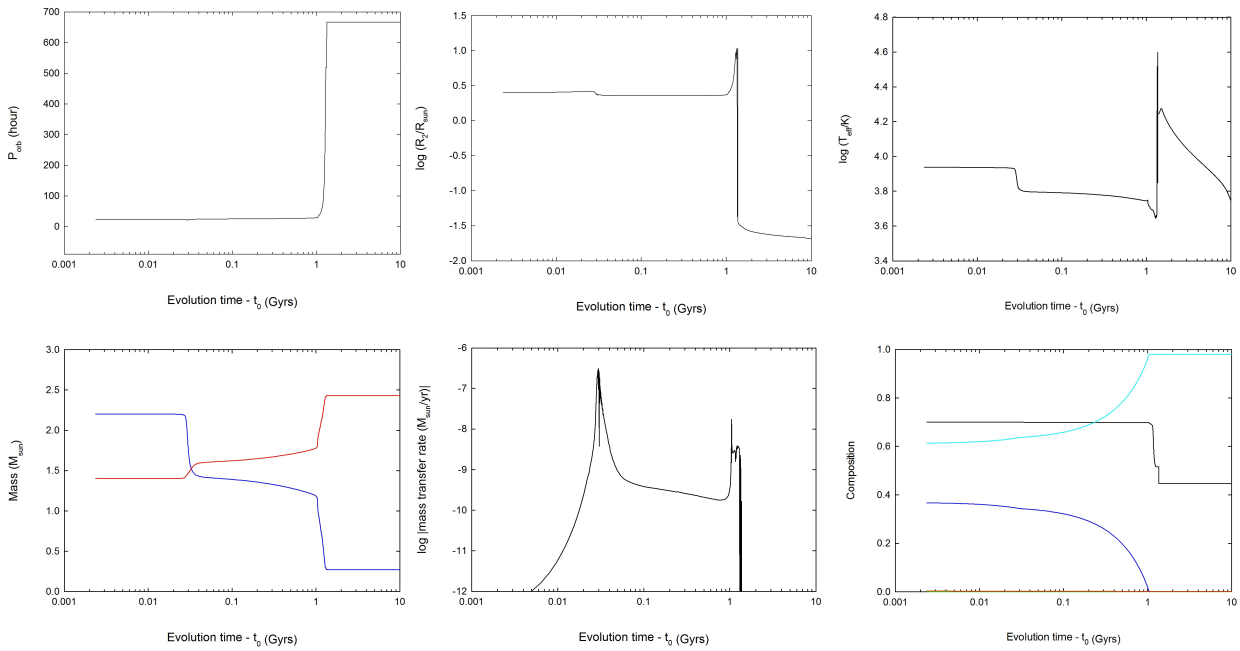

Figure 2.12: Same description for the graphs as for Figure 2.10. The initial conditions for this evolution are $M_{1,i} = 1.4\,M_\odot$, $M_{2,i} = 2.20\,M_\odot$ and $P_{orb,i} \cong 22.91$ hours. The final values are $M_{1,f} \cong 2.43\,M_\odot$, $M_{2,f} \cong 0.27\,M_\odot$ and $P_{orb,f} \cong 666.9$ hours.

Now, let us look at the evolution depicted in Figure 2.11. In this case, one starts again with an intermediate-mass donor star, but in a $\simeq 3.6$ day initial orbital period. Already, the evolution is somewhat different. At the beginning, around 0.0002 Gyrs, the mass-transfer rate peaks above the Eddington limit, so the donor loses a lot of mass, but the neutron star accretes almost nothing. The orbital period decreases a little, but rapidly, the donor star becomes less massive than the neutron star, and the orbital period increases significantly. Note that the noise in the mass transfer curve is not physical. This is due to having a time step that is too large to have a good resolution. However, this allows for faster computations, which is significant for large simulations, and the end results remain correct. Note that because the evolution started with a larger orbital period, the donor starts its mass-transfer phase with already no more hydrogen at its center. Thus, helium burns after the first mass-transfer peak and there is no second mass-transfer phase such as in the previous case. Therefore, the donor ends as a carbon-oxygen white dwarf once again, but the neutron star has not accreted a lot of mass.

Looking at Figure 2.12, one starts with a smaller donor star ($2.2\,M_\odot$) in a $\simeq 23$ hour period. This time, one finds again two main phases. During the first mass-transfer phase, the mass-transfer rate is above the Eddington limit, but not by a large fraction, so the neutron

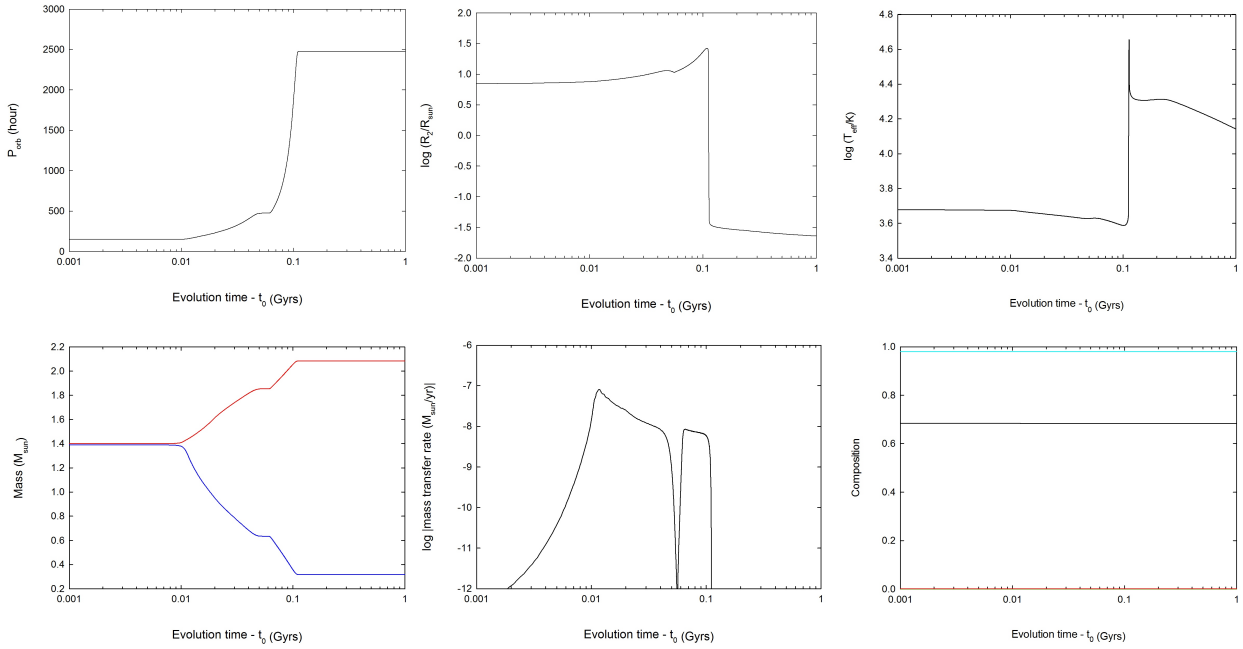

Figure 2.13: Same description for the graphs as for Figure 2.10. The initial conditions for this evolution are $M_{1,i} = 1.4\,M_\odot$, $M_{2,i} = 1.39\,M_\odot$ and $P_{orb,i} \cong 158.49$ hours. The final values are $M_{1,f} \cong 2.08\,M_\odot$, $M_{2,f} \cong 0.32\,M_\odot$ and $P_{orb,f} \cong 2476.9$ hours.

star manages to accrete some mass. Then, because of the smaller initial orbital period, one notes that the initial radius is smaller than seen before, and the donor star has burned less hydrogen. Thus, a second mass-transfer phase starts when all the hydrogen is burned. The mass-transfer rate being smaller than the Eddington limit, the neutron star accretes a significant amount of mass, and the orbital period increases substantially. Also, the radius drops, and the system ends with a massive neutron star and a helium-core white dwarf.

Starting with different initial conditions ($M_{2,i} \simeq M_{1,i}$, $\simeq 6.6$ day period), one observes a rather different evolution looking at Figure 2.13. With such a large initial period, the donor star has no more hydrogen at its core at the beginning of mass transfer. The mass-transfer rate then stays below the Eddington limit (or only slightly above), and the neutron star accretes a lot of mass. The composition remains the same, the donor shrinks, and the system ends with a massive neutron star and a helium-core white dwarf.

2.4.3 Ends Points and Binary Millisecond Pulsars

In the previous section, the evolutionary tracks of a few LMXBs and IMXBs were shown. In general, the donor star ended its evolution as a white dwarf. The resulting neutron star-white dwarf system is called a binary millisecond pulsar (introduced in Section 2.4.1), since the neutron is spun up by mass accretion to become a millisecond pulsar (see Tauris & van den Heuvel [157], and references therein, for a general discussion on the formation of binary millisecond pulsars).

Table 2.1: Observed properties of many binary millisecond pulsars.

Pulsar Name [Ref.]	$M_{WD}\,(M_\odot)$	$M_{NS}\,(M_\odot)$	$P_{orb}\,(\text{hour})^2$
J0034-0534 [9]	≥ 0.14	–	38.14
J0218+4232 [104, 85]	≥ 0.16	–	48.69
J0437-4715 [172]	0.254 ± 0.014	1.76 ± 0.20	137.79
J0613-0200 [94]	≥ 0.13	–	28.76
J0621+1002 [154, 111]	$0.97^{+0.27}_{-0.15}$	$1.70^{+0.10}_{-0.17}$	199.65
J0751+1807 [110, 111]	0.191 ± 0.015	1.26 ± 0.14	6.32
J1012+5307 [24, 113]	0.156 ± 0.02	1.64 ± 0.22	14.5
J1023+0038 [18]	~ 0.2	–	4.8
J1045-4509 [9, 165]	≥ 0.16	≤ 1.48	98.00
J1141-6545 [16]	1.02 ± 0.01	1.27 ± 0.01	4.74
J1232-6501 [27]	≥ 0.14	–	44.72
J1435-6100 [27]	≥ 0.9	–	32.52
J1454-5846 [27]	≥ 0.87	–	298.15
J1455-3330 [94]	≥ 0.27	–	1828.19
J1528-3146 [69]	≥ 0.94	–	76.33
J1600-3053 [69]	≥ 0.2	–	344.36
J1603-7202 [95]	≥ 0.29	–	151.41
J1614-2230 [35]	0.500 ± 0.006	1.97 ± 0.04	208.48
J1643-1224 [94]	≥ 0.13	–	3528.42
J1713+0747 [155]	0.28 ± 0.03	$1.53^{+0.08}_{-0.06}$	1627.80
J1738+0333 [4]	$0.181^{+0.007}_{-0.005}$	$1.47^{+0.07}_{-0.06}$	8.51
J1741+1351 [69]	≥ 0.24	–	392.04
J1745-0952 [70]	≥ 0.11	–	118.64
J1802-2124 [41]	0.78 ± 0.04	1.24 ± 0.11	16.77

[2]Note that the value written for the orbital period is rounded to the last digit given the high accuracy with which it can be measured.

J1804-2718 [95, 165]	≥ 0.21	≤ 1.73	267.6
J1810-2005 [70]	≥ 0.28	–	360.29
J1816+4510 [72]	0.193 ± 0.012	1.84 ± 0.11	8.66
J1853+1303 [52]	$0.33 - 0.37$	1.4 ± 0.7	2775.69
B1855+09 [73, 109]	0.258 ± 0.028	$1.57^{+0.12}_{-0.11}$	295.92
J1903+0327 [44]!!!	1.029 ± 0.008	1.667 ± 0.021	2284.18
J1904+0412 [27]	≥ 0.22	–	358.42
J1909-3744 [68]	0.2038 ± 0.0022	1.438 ± 0.024	36.80
J1910+1256 [52]	$0.30 - 0.34$	1.6 ± 0.6	1403.20
J1911-1114 [95]	≥ 0.12	–	65.20
J1918-0642 [70]	≥ 0.24	–	261.92
J1933-6211 [69]	≥ 0.32	–	307.67
B1957+20 [171]	0.035 ± 0.002	2.40 ± 0.12	9.17
J2016+1948 [52]	$0.43 - 0.47$	1.0 ± 0.5	15240.57
J2019+2425 [108]	~ 0.35	≤ 1.51	1836.28
J2129-5721 [95]	≥ 0.14	–	159.01
J2145-0750 [9]	≥ 0.43	–	164.13
J2317+1439 [25, 178]	≈ 0.21	–	59.02

Table 2.2: Observed properties of many binary millisecond pulsars in globular clusters.

Pulsar Name [Ref.]	Globular Cluster	$M_{WD}\,(M_\odot)$	$M_{NS}\,(M_\odot)$	$P_{orb}\,(\mathrm{d})$
J0024−7205E [45]	47 Tuc	≥ 0.15	–	2.256844820
J0024−7204H [45, 80]	47 Tuc	$0.18^{+0.086}_{-0.016}$	$1.48^{+0.03}_{-0.06}$	2.35769683
J0024−7204I [45]	47 Tuc	≥ 0.013	–	0.229792249
J0023−7203J [45]	47 Tuc	≥ 0.021	–	0.12066493779
J0024−7204O [45]	47 Tuc	≥ 0.022	–	0.1359743050
J0024−7204P [26, 8]	47 Tuc	~ 0.02	–	0.1472
J0024−7204Q [45]	47 Tuc	≥ 0.18	–	1.189084048
J0024−7204R [26, 8]	47 Tuc	~ 0.03	–	0.0662
J0024−7204S [45]	47 Tuc	≥ 0.088	–	1.201724235
J0024−7204T [45]	47 Tuc	≥ 0.17	–	1.126176767
J0024−7203U [45]	47 Tuc	≥ 0.12	–	0.4291056833
J0024−7204V [26, 8]	47 Tuc	~ 0.35	–	0.227

J0024−7204W [26, 8]	47 Tuc	$\gtrsim 0.13$[3]	–	0.1330
J0024 – 7204Y [26, 8]	47 Tuc	~ 0.16	–	0.52194
J0514 – 4002A [47, 80]	NGC 1851	≥ 0.96	$1.49^{+0.04}_{-0.27}$	18.78517915
B1310+18 [8]	M53	~ 0.35	–	255.8
J1342+2822B [8]	M3	~ 0.21	–	1.41735
B1516+02B [48]	M5	$0.172^{+0.107}_{-0.023}$	$2.09^{+0.18}_{-0.19}$	6.8584538
J1518+0204D [8]	M5	~ 0.20	–	1.22
J1518+0204E [8]	M5	~ 0.15	–	1.10
J1546 – 3747A [97]	NGC 5986	≥ 0.16	–	1.3467116
B1639+36B [8]	M13	~ 0.19	–	1.25911
J1641+3627D [8]	M13	~ 0.18	–	0.591
J1641+3627E [8]	M13	~ 0.02	–	0.117
J1701 – 3006A [96]	M62	≥ 0.2	–	3.8059483732
J1701 – 3006B [96]	M62	≥ 0.12	–	0.1445451718
J1701 – 3006C [96]	M62	≥ 0.071	–	0.21500007119
J1701 – 3006D [96]	M62	≥ 0.12	–	1.1179034034
J1701 – 3006E [96]	M62	≥ 0.031	–	0.1584774951
J1701 – 3006F [96]	M62	≥ 0.021	–	0.2054870422
B1718 – 19 [8]	NGC 6342	~ 0.13	–	0.25827
J1740 – 5340A [33, 8]	NGC 6397	≥ 0.18	–	1.35406
J1748 – 2021B [46]	NGC 6440	$0.142^{+0.086}_{-0.018}$	$2.74^{+0.21}_{-0.22}$	20.5500072
J1748 – 2021D [46]	NGC 6440	≥ 0.12	–	0.2860686769
J1748 – 2021F [46]	NGC 6440	≥ 0.30	–	9.83396979
J1748 – 2446A [8, 130]	Ter5	≥ 0.089	–	0.075646
J1748 – 2446E [130]	Ter5	≥ 0.22	–	60.06
J1748 – 2446I [130]	Ter5	≥ 0.24	$1.91^{+0.02}_{-0.10}$	1.328
J1748 – 2446J [130]	Ter5	≥ 0.38	$1.79^{+0.02}_{-0.10}$	1.102
J1748 – 2446M [130]	Ter5	≥ 0.14	–	0.4431
J1748 – 2446N [130]	Ter5	≥ 0.48	–	0.3855
J1748 – 2446O [130]	Ter5	≥ 0.036	–	0.2595
J1748 – 2446P [130]	Ter5	≥ 0.38	–	0.3626
J1748 – 2446V [130]	Ter5	≥ 0.12	–	0.5036
J1748 – 2446W [130]	Ter5	≥ 0.30	–	4.877
J1748 – 2446Y [8, 130]	Ter5	≥ 0.14	–	1.16443
J1748 – 2446ad [8]	Ter5	~ 0.16	–	1.09443

[3]The companion star is not a white dwarf but a main sequence star according to Bogdanov et al. 2005 [19].

J1748 – 2446ae [8]	Ter5	~ 0.019	–	0.17073
J1750 – 3703A [46]	NGC 6441	≥ 0.53	≤ 1.65	17.3342759
J1750 – 3703B [46]	NGC 6441	≥ 0.17	–	3.60511446
J1801 – 0857B [98]	NGC 6517	≥ 0.33	–	59.8364526
B1802-07 [164, 6, 165]	NGC 6539	0.33 ± 0.08	$1.26^{+0.08}_{-0.17}$	2.61676335
J1807 – 2459A [96]	NGC 6544	≥ 0.0092	–	0.071091483516
J1807 – 2459B [96]	NGC 6544	1.2064 ± 0.0020	1.3655 ± 0.0021	9.9566681588
J1824 – 2452C [48]	M28	≥ 0.260	≤ 1.367	8.07781
J1824 – 2452G [8]	M28	~ 0.011	–	0.1046
J1824 – 2452H [117, 8]	M28	~ 0.20	–	0.43502743
J1824 – 2452I [8]	M28	~ 0.20	–	0.45941
J1824 – 2452J [8]	M28	~ 0.015	–	0.0974
J1824 – 2452K [8]	M28	~ 0.16	–	3.91034
J1824 – 2452L [8]	M28	~ 0.022	–	0.22571
J1836 – 2354A [98]	M22	≥ 0.017	–	0.2028278011
J1905+0154A [8]	NGC 6749	~ 0.090	–	0.81255
J1910 – 59 [33]	NGC 6752	≥ 0.19	–	0.865
J1910 – 5959A [30]	NGC 6752	0.180 ± 0.018	1.33 ± 0.11	0.83711347691
J1911 – 5958A[4] [11, 8]	NGC 6752[5]	0.18 ± 0.02	$1.40^{+0.16}_{-0.10}$	0.83711
J1911+0102A [8]	NGC 6760	~ 0.020	–	0.140996
J1953+1846A [8]	M71	~ 0.032	–	0.1766
J2140 – 2310A [131]	M30	≥ 0.1	–	0.17398746418

Table 2.1 lists some observed binary millisecond pulsars and their properties. While the orbital period can be computed very accurately, the same is not true for the masses of the component stars. Indeed, the uncertainty due to the unknown inclination angle of these binary systems makes it hard to compute the mass of the neutron star and of its companion. For most systems, it is only possible to have a lower bound on the companion's mass. However, for other systems, the mass of the pulsar can be estimated with a proper analysis of the Shapiro radio delay (e.g., [68, 156]).

Our goal is to compare the end points of every evolutionary tracks computed in the grid shown in Figure 2.8 together with the observed binary millisecond pulsars. This is exactly what Figure 2.14 shows. Looking at panel a), the final orbital period as a function of the final donor star mass, one can see that the observed properties of most of the binary millisecond pulsars can be explained by the numerical simulations in this work. Note that the presence of a blue-green line this figure. It represents a possible relationship between the orbital

[4]I'M NOT SURE IF THAT'S NOT THE SAME BMSP THAN THE ONE ABOVE (J1910-5959A)...

[5]Bassa et al. 2006 [11] discuss the fact that PSR J1911-5958A might be a field oject rather than part of the globular cluster NGC 6752. However, they cannot confirm nor disprove this fact.

period and the white dwarf's mass for binary millisecond pulsars. Although there exists many formulae for the $P_{orb,f} - M_{2,f}$ relation (e.g., [133, 160, 106]), this work compares its results with the formula of Lin et al. [90]. It turns out that the curve matches the numerical results of this thesis. In general, the end points shown in Figure 2.14 match the results of Lin et al. [90] obtained with an earlier version of the `MESA` code (different treatment of the physics of mass accretion onto a neutron star).

Looking at panel b) of Figure 2.14, the conclusion is rather different. Although a few binary millisecond pulsars have massive neutron stars, most of them have masses in the range $1.2-1.8\,M_\odot$ with white dwarfs of small masses ($0.15-0.30\,M_\odot$). However, the computations produced mainly massive neutron stars ($1.9-2.6\,M_\odot$) with small white dwarfs and small neutron stars with massive white dwarfs. Thus, there seems to be a disagreement between the observations and the theoretical model.

Note that Lin et al. [90] did not consider the effects of the binding energy of neutron stars. Because of that, their work shows even more massive neutron stars where smaller neutron stars would be desired. Thus, this work shows an improvement in terms of producing smaller neutron stars because of their binding energy, but still, the neutron stars would need to be smaller to match the observations.

2.4.4 The Effects of Changing the Maximum mass-transfer fraction

One way to produce less massive neutron stars is to limit the mass-transfer fraction; i.e., reduce the value of β_{max}. Recalling Equation 2.101 and the definition of β, it is easy to see that small values of β_{max} would seriously reduce the accretion rate of the neutron star, $\dot{M}_1$. Thus, the neutron star would accrete less mass throughout the evolution of the X-ray binary system. In the end, the mass of the neutron stars would probably be closer to the observed values.

There are reasons to believe that purely conservative mass transfer ($\beta_{max} = 1$) does not occur. Indeed, relativistic jets or high radiation pressures causing wind emanating from the atmosphere of the accretion disk could lead to inefficient accretion. Also, the propeller effect might be important. The propeller effect (first introduced by Illarionov & Sunyaev [66]) takes place when the magnetospheric radius is larger than the corotation radius, i.e., when (see Rappaport et al. [132])

$$r_m \simeq (GM_1)^{-1/7}\,\dot{M}_1^{-2/7}\mu^{4/7} > r_c = \left(\frac{GM_1}{\omega_{NS}^2}\right)^{1/3}, \tag{2.126}$$

where μ is the magnetic dipole moment of the neutron star. When this happens, the centrifugal force pushes matter away from the neutron star, and consequently, from the X-ray binary system. There has been observational evidence of the propeller effect in some X-ray pulsars (e.g., [32, 179]).

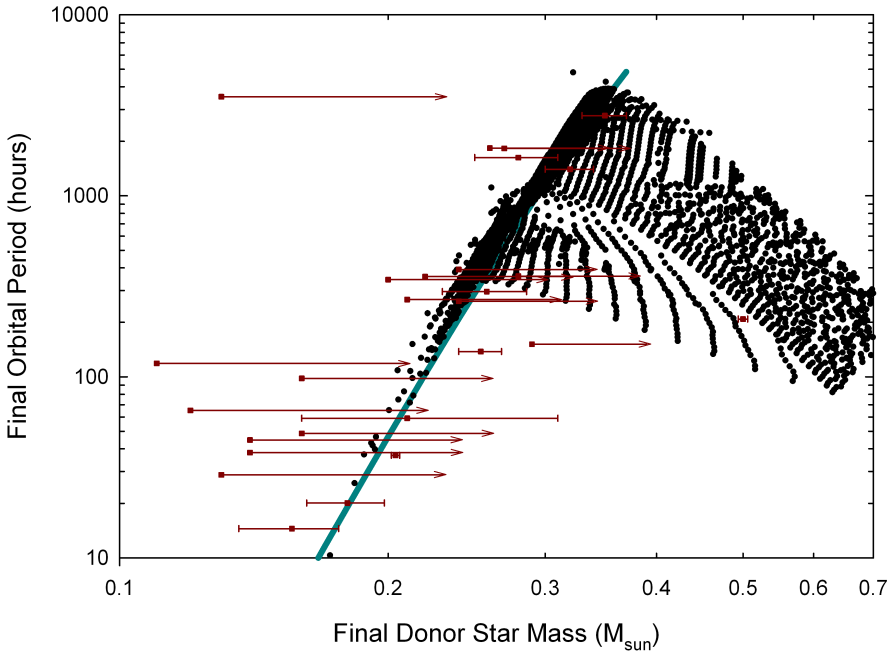

a)

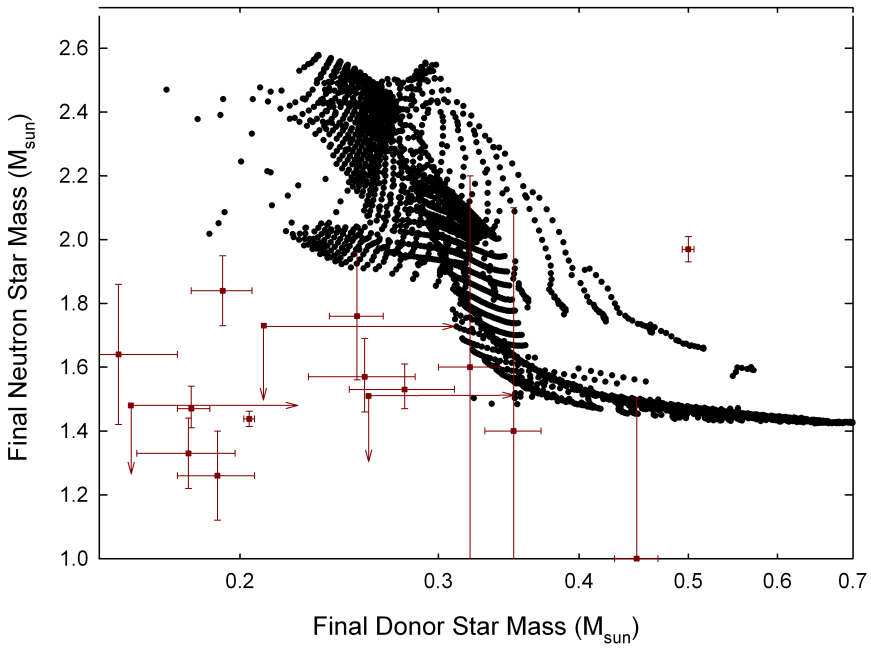

b)

Figure 2.14: End points of the evolutionary grid presented in Figure 2.8a). The blue line in panel a) comes from Lin et al. [90]. The observed binary millisecond pulsars (the red squares together with their uncertainty bars) are taken from Table 2.1.

The value that β_{max} should take is not obvious though. For example, Podsiadlowski et al. [122] and others (e.g., [160, 107, 15]) used $\beta_{max} = 0.5$, and Lin et al. [90] used $\beta_{max} = 0.9$, somewhat arbitrarily. Also, Nelson et al. [106] tested $\beta_{max} = 0$ (completely non-conservative mass transfer) as a limiting case, but they acknowledge that this value is highly uncertain. The value of $\beta_{max} = 1$ has been used so far in this thesis, and this is what will be used the the following chapters. This can also be viewed as a limiting case, keeping in mind that neutron star can accrete less than what is found via *ad hoc* non-conservative mass transfer.

In order to better understand the effects of modifying β_{max}, one can compute similar grids to panel a) of Figure 2.8, and change the value of β_{max}. De Vito and Benvenuto [36] tried to do something similar by computing small evolutionary grids with several values of β_{max}. Although, they were able to quantify the effects of changing β_{max}, they were not able to conclude what the value of the maximum mass-transfer fraction should be.

Let us look at the effects of changing β_{max}. Figure 2.15 shows the same evolutionary grid as panel a) of Figure 2.8, but with different values of β_{max}: panel a) shows $\beta_{max} = 0.5$ and panel b) shows $\beta_{max} = 0$. In general, the evolutionary paths do not seem to be modified, so one has to look at the end points to really grasp the magnitude of the effect.

Looking at panel a) of Figure 2.16, one can see that for $\beta_{max} = 1$ and $\beta_{max} = 0.5$, the end points are really similar. The case $\beta_{max} = 0$ produced systems with slightly shorter final orbital periods, but the effect does not seem to be too important. Looking at panel b), one can see the three cases completely dissociated from one another. Obviously, for the case $\beta_{max} = 0$, the final neutron star mass is $1.4\,M_{\odot}$, the same as the natal mass since none of the mass transferred is accreted onto the neutron star. For the case $\beta_{max} = 0.5$, it is fair to say that the final neutron stars have masses half-way between the $\beta_{max} = 1$ case and the $\beta_{max} = 0$ case. The $\beta_{max} = 0$ and $\beta_{max} = 0.5$ cases have the advantage of reproducing the observed properties of the smaller neutron stars as expected and as wanted, but there is a caveat. Focusing on the observed system PSR J1614-2230 with $M_{NS} = 1.97 \pm 0.04\,M_{\odot}$ and $M_{WD} = 0.500 \pm 0.006\,M_{\odot}$, one can see that none of the models in panel b) of Figure 2.16 can reproduce the observations. This system could not be explained with $M_{1,i} = 1.4\,M_{\odot}$ and $\beta_{max} = 1$, but with smaller values of β_{max}, the final values deviated even more. With conservative mass transfer, it is possible to reproduce the properties of this system with $M_{1,i} = 1.6\,M_{\odot}$ (see Section 4.2.2, and Lin et al. [90] who uses $\beta_{max} = 0.9$). However, if one assumes non-conservative mass transfer (say $\beta_{max} \lesssim 0.5$), then it becomes really difficult to explain the observed properties of PSR J1614-2230 since it would require a really large natal mass for the neutron star.

To summarize, it seems that with $\beta_{max} = 1$, the numerical simulations produce systems with final orbital periods and final donor star masses that match most of the observed binary millisecond pulsars. However, the results produce neutron stars that seem to have accreted too much matter compared to the observed systems. Thus, to resolve this issue, one has to either claim that mass transfer is highly non-conservative (probably $0 \leq \beta_{max} \lesssim 0.5$) or that the natal mass of the neutron star has to be smaller (different natal masses for the

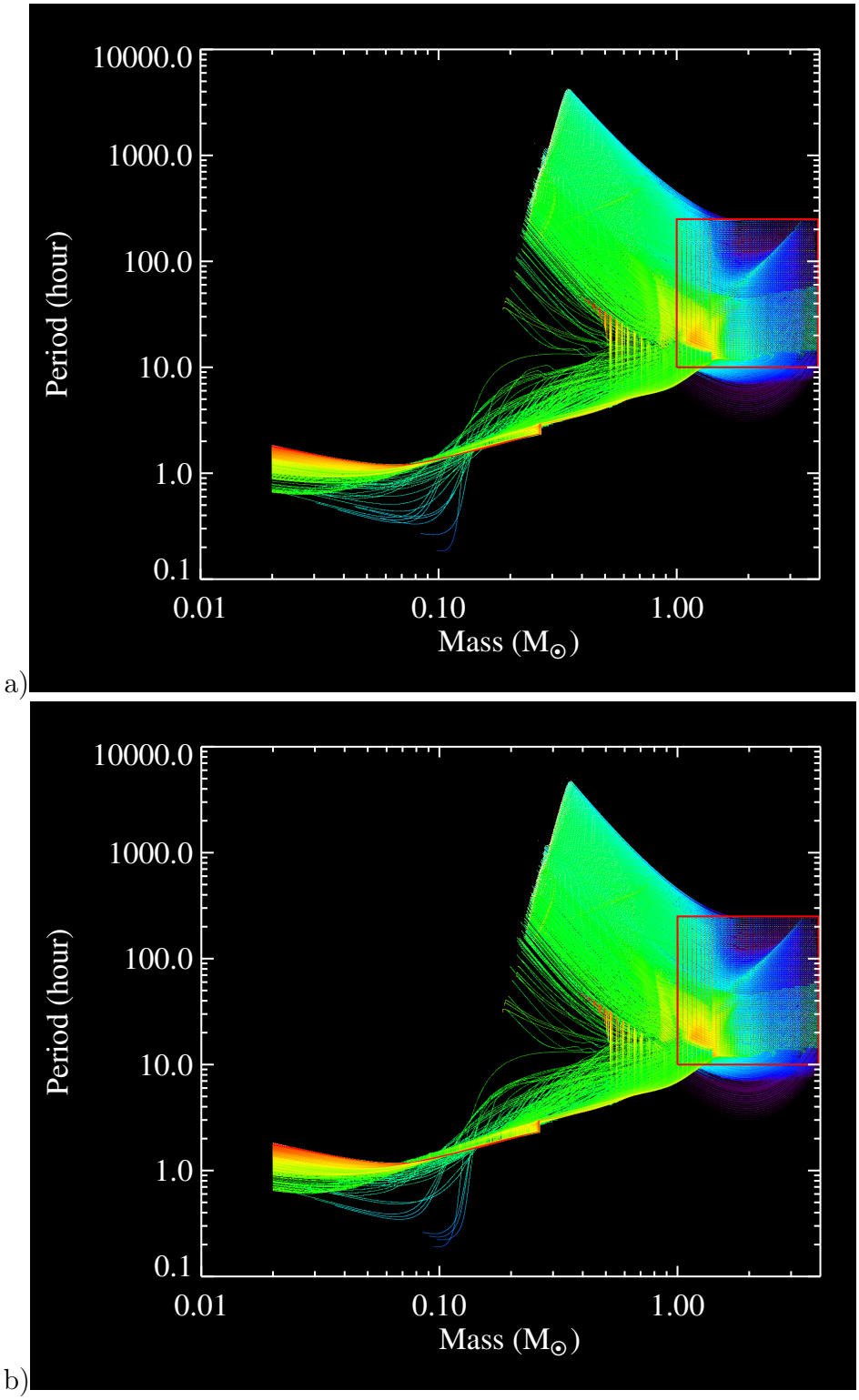

Figure 2.15: Same description as panel a) of Figure 2.8. Panel a) shows the results with $\beta_{max} = 0.5$ and panel b) shows the results with $\beta_{max} = 0.0$.

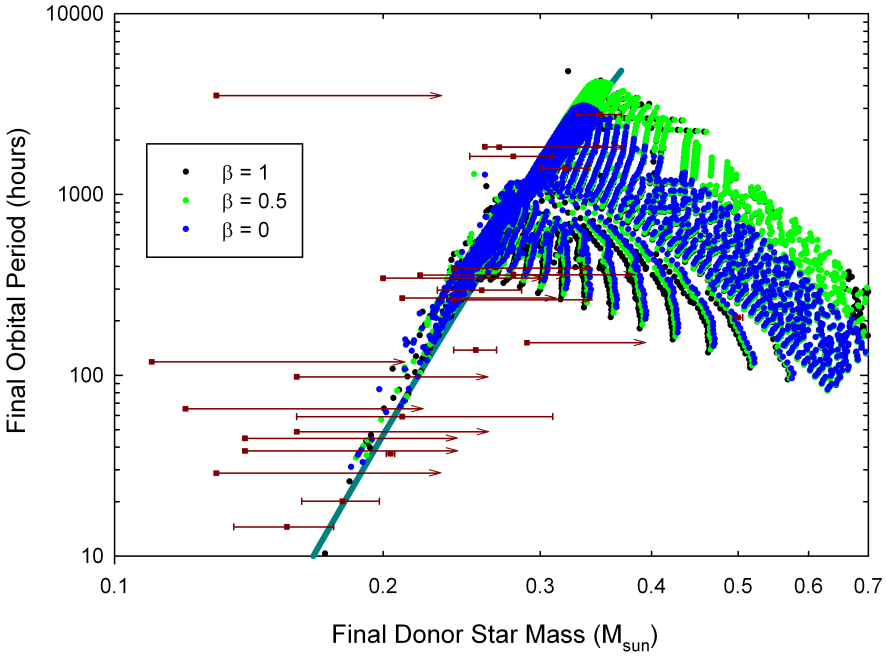

a)

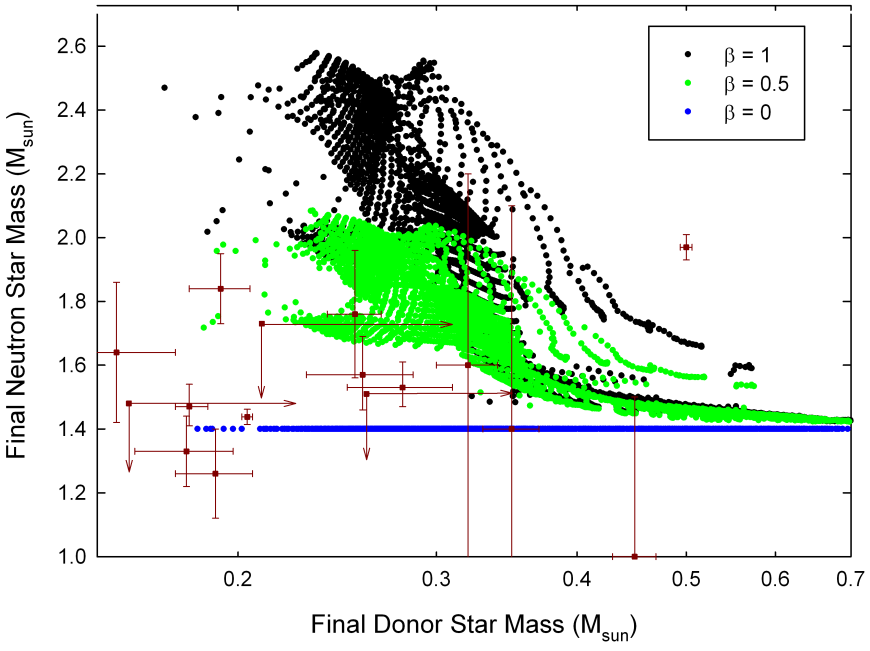

b)

Figure 2.16: End points of the evolutionary grids shown in Figure 2.15. Note that the black dots show $\beta_{max} = 1$, the green dots show $\beta_{max} = 0.5$, and the blue dots show $\beta_{max} = 0.0$.

neutron stars will be tested in Section 4.2.2). However, if mass transfer is non-conservative, it becomes really difficult to reproduce the observed properties of PSR J1614-2230 even with a larger natal mass for the neutron star. The solution to this issue might reside in the effects of self-induced irradiation as will be discussed in the following chapters.

Part II

The Effects of Self-Induced Irradiation

Chapter 3

X-ray Irradiation: The Model

The physics of X-ray irradiation (or heating) of the donor star has been completely ignored so far in our study. It is important to note that X-ray irradiation has been ignored in many studies of X-ray binary evolution (e.g., [134, 177, 133, 160, 122, 106, 90, 158, 36]) and it is still an open question as to whether or not irradiation should be taken into consideration in X-ray binary evolution. The goal of the following chapters is to find how important are the effects of X-ray irradiation.

X-ray irradiation occurs when the charged particles in the accretion disk of the neutron star are accelerated and radiate X-rays. If some of the X-rays are intercepted by the donor star, then the X-ray photons penetrate the photosphere of the donor and deposit extra energy in the outer envelopes. The extra energy destabilizes the donor star, which then increases its radius as the star attempts to attain thermal equilibrium. With a larger radius, more mass of the donor star overflows the Roche lobe, thus increasing the mass-transfer rate. Therefore, it is expected that this effect modifies the evolution of X-ray binary systems.

Astrophysicists started investigating the effects of X-ray irradiation as early as the 1970s and 1980s (e.g., [5, 12, 112, 54, 74, 144]); it is only at the beginning of the 1990s that they began to understand why this might be important in X-ray binary evolution (e.g., [120, 161, 58, 42, 55]). Podsiadlowski [120, 121] (and Hameury et al. [55, 56] a few years later) showed that a constant irradiation flux increased the radius of low-mass stars (see Figure 3.1).

Then, other groups investigated the effects of irradiation in the 1990s (e.g., [21, 34, 51, 163, 59, 136, 162, 174, 60, 75, 76, 138, 57, 77]), and soon thereafter, they began to compute evolutionary tracks considering the effects of irradiation for Cataclysmic Variables (e.g., [100]) and for low-mass X-ray binaries (e.g., [139, 22, 23, 137, 15]). However, none of them had computed a full evolutionary grid to understand the overall effect of X-ray irradiation.

The `rlo` test suite in the `MESA` code offers the possibility of including X-ray irradiation in X-ray binary evolution, but this is done rather crudely. For this reason, a more sophisticated model is built in thesis. Sections 3.1 and 3.2, respectively, show the theory behind X-ray

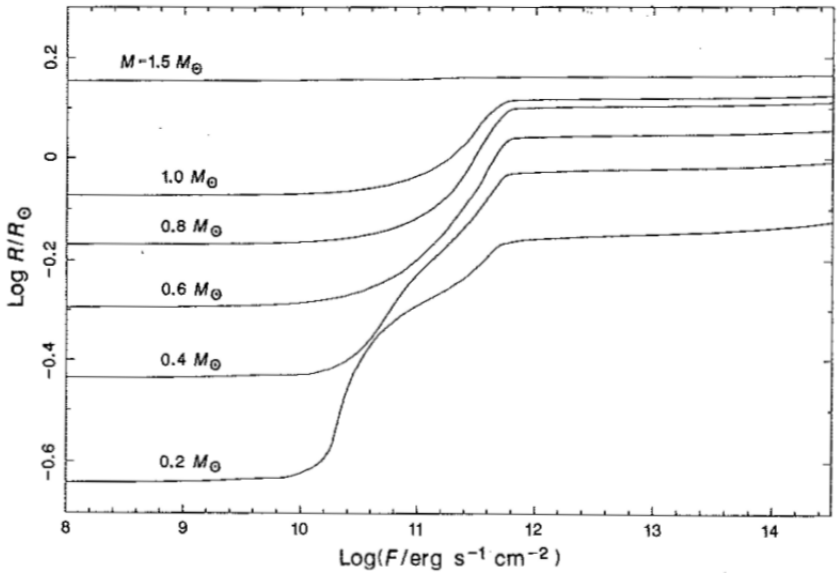

Figure 3.1: Equilibrium radius, R, as a function of external irradiation flux, F, for unevolved stars of mass M (taken from Podsiadlowski [120]). Hameury et al. [55, 56] obtained similar results.

irradiation and the model built in this thesis to include the effects of irradiation. Then, Section 3.3.2 shows evolutionary track including the effects of X-ray irradiation.

3.1 Irradiation Flux

First of all, it is necessary to know what X-ray flux irradiates the donor star. The irradiating luminosity, L_{irr}, is really only the luminosity of the neutron star. So, replacing L_1 by L_{irr} in Equation 2.92, one has

$$L_{irr} = \frac{GM_1\dot{M}_1}{R_1}\,. \tag{3.1}$$

Then, assuming that the X-rays are emitted isotropically, the irradiating flux at the surface of the donor star can be expressed as

$$F_{irr} = \frac{L_{irr}}{4\pi a^2} = \frac{GM_1\dot{M}_1}{4\pi a^2 R_1}\,. \tag{3.2}$$

However, there are strong reasons to believe that not all this X-ray flux reaches the donor star. Indeed, it might be possible that the accretion disk of the neutron star intercepts a fraction of the X-rays, thus reducing F_{irr}. Unfortunately, the theory of accretion disk physics

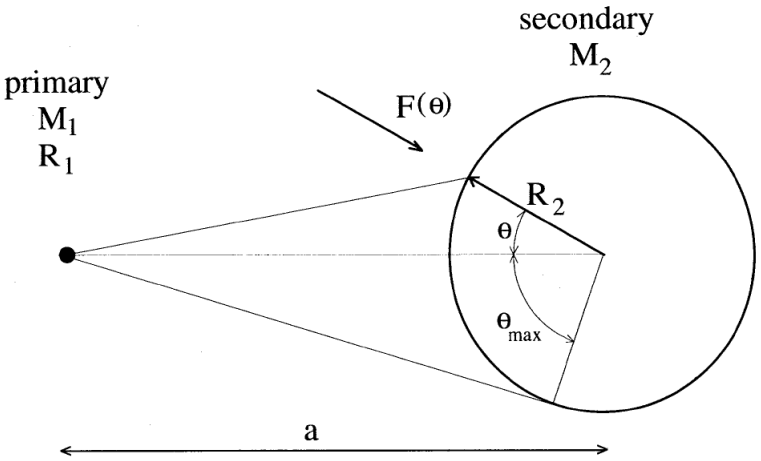

Figure 3.2: Geometry of an X-ray binary system (taken from King et al. [76]).

is an active field of research on its own (for an introduction on the subject, see for example, [167, 78, 43], and references therein, or any standard high-energy astrophysics textbook such as [93, 81, 101, 91]). Thus, computing what fraction of the total X-ray flux could traverse a certain type of accretion disk would require intensive computations. Moreover, it is not even well understood what kind of accretion disk is formed around neutron stars in X-ray binaries, thus making the calculations rather uncertain. For those reasons, it is preferred for this thesis to simply introduce an efficiency factor η (as Hameury et al. [55] and many others do, e.g., [59, 100, 139, 22, 23]). This factor accounts for the fraction of the total X-ray flux that reaches the surface of the donor star. Therefore, Equation 3.2 must be modified:

$$F_{irr} = \frac{\eta G M_1 \dot{M}_1}{4\pi a^2 R_1} \,. \tag{3.3}$$

Obviously, this equation is valid at the surface point aligned with the center of both the donor star and the neutron star. At different points on the surface, a geometrical factor must be taken into account. Therefore,

$$F_{irr}(\theta) = \frac{\eta G M_1 \dot{M}_1}{4\pi a^2 R_1} h(\theta) \,, \tag{3.4}$$

where $h(\theta)$ is the geometrical factor and θ is the angle shown in Figure 3.2.

King et al. [76] have an equation for the geometrical factor,

$$h(\theta) = \frac{\cos(\theta) - f_2}{(1 - 2 f_2 \cos(\theta) + f_2^2)^{\frac{3}{2}}} \,, \tag{3.5}$$

with $f_2 \equiv R_2/a$. Although this equation has been reused in several articles (e.g., [57, 100, 139, 22]), we believe that it should be

$$h(\theta) = \frac{\cos(\theta) - f_2}{(1 - 2f_2\cos(\theta) + f_2^2)^{\frac{1}{2}}}\,. \tag{3.6}$$

A proof of this can be found in Appendix A.1 of this work.

Hameury et al. [55], Harpaz & Rappaport [59], and Becker et al. [13] came up with prescriptions for the efficiency factor η that would qualitatively have the desired properties for a shielding term. For instance, Hameury et al. used

$$L_{irr} = \begin{cases} \eta L_1 \left(\frac{R_2}{2a}\right)^2 & \text{if } \dot{M}_2 < \dot{M}_{edd} \\ \eta L_{edd} \left(\frac{R_2}{2a}\right)^2 \frac{\left(\dot{M}_2/\dot{M}_{edd}\right)^2}{e^{|\dot{M}_2|/\dot{M}_{edd}-1}} & \text{if } \dot{M}_2 \geq \dot{M}_{edd} \end{cases}, \tag{3.7}$$

and Harpaz & Rappaport used

$$L_{irr} = \begin{cases} \eta L_1 \left(\frac{R_2}{2a}\right)^2 & \text{if } \dot{M}_2 < \dot{M}_{edd} \\ \eta L_{edd} \left(\frac{R_2}{2a}\right)^2 \exp\left(1 - \frac{|\dot{M}_2|}{\dot{M}_{edd}}\right) & \text{if } \dot{M}_2 \geq \dot{M}_{edd} \end{cases}. \tag{3.8}$$

In both cases, η is arbitrarily taken to be 0.1. Note that the factor $(R_2/2a)^2$ approximately accounts for the geometry of the system.

Rather than using some of these *ad hoc* equations, this work simply uses Equation 3.4 and tests different values of η. In particular, the following values are tested: $\eta = 0.05$, 0.1, 0.5, and 1.0 (see Chapter 4). Testing different values for η is what is done by several other groups (e.g., [174, 100, 139, 22, 15]).

As discussed in Section 2.3.2, there is some uncertainty regarding the choice of R_1, but for the reasons explained in Section 2.3.2, a constant value of 11.5 km is taken throughout this thesis.

3.2 Energy Deposition

Now, the effects of irradiation can only take place if the X-ray irradiating flux reaches the photosphere of the donor star. To verify this, let us first do a few calculations from first principles. The hydrostatic equation of stellar structure, $\frac{dP}{dr} = -g\rho$, combined with the ideal gas law, $P = \rho N_A k_B T/\mu$, (which implies that $\frac{dP}{dr} = \frac{d\rho}{dr} N_A k_B T/\mu$) yields

$$-g\rho = \frac{1}{\mu}\frac{d\rho}{dr} N_A k_B T\,, \tag{3.9}$$

which can be integrated from the surface of the star ($r = R$), to an arbitrary radius, r. Thus,

$$\rho(r) = \rho_s \exp\left[\frac{\mu g}{N_A k_B T}\left(R - r\right)\right] . \tag{3.10}$$

Introducing the column depth (Σ) which is defined to satisfy

$$\frac{d\Sigma}{dr} = -\rho\,, \tag{3.11}$$

one can integrate from infinity to an arbitrary radius to find (letting $\Sigma \to 0$ as $r \to \infty$)

$$\Sigma(r) = \frac{\rho_s N_A k_B T}{\mu g} \exp\left[\frac{\mu g\left(R - r\right)}{N_A k_B T}\right] . \tag{3.12}$$

Solving for r yields

$$r = \left[1 - \frac{k_B T}{\mu g R} \ln\left(\frac{\Sigma \mu g}{\rho_s k_B T}\right)\right] R\,. \tag{3.13}$$

It is thought that for X-rays in the energy range of $1 - 10\,\mathrm{keV}$, the column depth is of the order $\Sigma \sim 0.01 - 1\,\mathrm{g/cm^2}$ (e.g., [59]). A standard value of $1\,\mathrm{g/cm^2}$ is adopted in the `MESA` code to crudely model the effects of irradiation. Thus, taking $\Sigma_{irr} = 1\,\mathrm{g/cm^2}$ and standard values for temperature, density, and gravity (say for the Sun), one finds

$$r_{irr} \cong 1.0005\, R_\odot\,. \tag{3.14}$$

This would mean that X-rays would deposit energy right above the photosphere of the Sun. However, it could be that the column depth for X-rays is larger than $1\,\mathrm{g/cm^2}$, which would allow the X-rays to propagate below the photosphere. Also, even if the X-rays do not reach the photosphere at the beginning of the mass-transfer phase, the X-rays will heat up the atmosphere, which will make it become more optically thin to X-rays (see Brett & Smith [21]), and consequently, the X-rays will penetrate deeper into the atmosphere and, ultimately, penetrate the photosphere as expected.

Under these assumptions, the atmosphere of the donor star will be ignored and it will be assumed that X-rays reach the photosphere of the star with the flux given by Equation 3.3. The next step is to determine the penetration depth of the X-rays and the energy they deposit in the donor star. As this point, many groups (e.g., [120, 55, 59, 100, 139, 22]) greatly simplify the problem by assuming that the X-ray energy deposition is completely equivalent to changing the donor star's effective surface boundary condition. In other words, the blackbody luminosity at the surface of the star,

$$L_s = 4\pi R^2 \sigma_{SB} T_{eff}^4\,, \tag{3.15}$$

becomes (e.g., [55, 139])

$$L_s = 4\pi R^2 \sigma_{SB} T_{eff}^4 - L_{irr} = 4\pi R^2 \left(1 - s_{eff}\right) \sigma_{SB} T_{eff}^4 \,, \tag{3.16}$$

where s_{eff} is a function of F_{irr}. However, given the sophistication of the `MESA` code used in this thesis, we can obtain much more accurate results by performing Monte-Carlo simulations to determine the most probable penetration depth of the X-ray photons in the donor star. Then, it is easy to modify the conservation of energy equation of stellar structure at the appropriate depth by adding a factor ϵ_{irr}; recalling Equation 2.8, we have

$$\frac{\partial L_m}{\partial m} = \epsilon - \nu - T\frac{\partial S}{\partial t} + \epsilon_{irr} \,. \tag{3.17}$$

3.2.1 Monte-Carlo Simulation

As explained in the previous section, the goal is to perform Monte-Carlo simulations to determine the penetration depth of X-rays in a star. The idea is as follows. Using random numbers, one generates a large number of X-ray energies that follow the energy distribution determined from the X-ray spectrum of the neutron star. Then, for each X-ray energy, one expects the optical depth (τ) of the photon to follow a probability distribution of the form

$$\frac{d\mathcal{P}}{d\tau} \propto e^{-\tau} \,, \tag{3.18}$$

where $\mathcal{P}$ is the probability. Recall that $d\tau = \kappa\rho dz$ where $\kappa = \sigma n/\rho$ is the opacity, n is the number density, σ is the cross-section of the X-ray photon, and z is the depth below the photosphere of the donor star. Introducing the mean free path $\lambda = 1/n\sigma$, one has $d\tau = \frac{1}{\lambda}dz$ and $\tau = z/\lambda$. Thus, one can rewrite Equation 3.18 as follows:

$$\frac{d\mathcal{P}}{dz} \propto \frac{e^{-\frac{z}{\lambda}}}{\lambda} \,. \tag{3.19}$$

Obviously, since the mean free path λ depends on the cross-section, λ depends on the X-ray energy that has been generated (this will be discussed more in depth in Section 3.2.3). Then, for each X-ray energy generated, one generates another random number, say $rand$, and one requires

$$\frac{\int_0^z \frac{d\mathcal{P}}{dz'} dz'}{\int_0^\infty \frac{d\mathcal{P}}{dz'} dz'} = rand \,, \tag{3.20}$$

which implies

$$z = -\lambda \ln\left(rand\right) \,. \tag{3.21}$$

One ends up with a probability distribution of the X-ray energy as a function of the depth below the photosphere. An example is shown in Section 3.2.5.

3.2.2 Neutron Star X-ray Spectrum

As seen in Section 3.2.1, to perform Monte-Carlo simulations to determine the penetration depth of X-rays, the X-ray spectrum of those X-rays has to be known. Although astronomers can fit nice power-law distributions, black-body distributions, thermal bremsstrahlung distributions, or combinations of them to X-ray binary spectra (e.g., [147, 29, 67, 146]), it is hard to predict the exact shape of these spectra theoretically (e.g., [151, 168, 141, 124, 142]). The general consensus is that for lower photon energies, the spectrum follows a black-body distribution, and for higher energies, the spectrum follows a power law with a high energy cut-off. Thus, one can write

$$\frac{d\mathcal{P}}{dE} \propto \begin{cases} \frac{E^2}{e^{E/k_B T_0}-1} & \text{if } E \lesssim E_0 \\ E^{-\alpha-1} e^{-E/E_{cut}} & \text{if } E \gtrsim E_0 \end{cases}, \tag{3.22}$$

where E is the X-ray energy, T_0 is the temperature of the black-body, E_0 is the turning point energy at which the power law becomes more important than the black-body distribution, α is a parameter of the power law function, and E_{cut} is the cut-off energy. This thesis follows Vilhu et al. [174] who uses $\alpha = 0.5$ and $E_{cut} = 10\,\text{keV}$, although other values are possible (e.g., [168, 142]). Following Tuchman & Yahel [168], $E_0 \sim 5\,\text{keV}$ is used. Finally, a thermal energy of $kT_0 = 1.16\,keV$ is used to match the spectra obtained by Tuchman & Yahel [168] (see Figure 3.3).

Then, using random numbers to generate X-ray energies that follow the distribution given above would require one to solve the following equation for E:

$$\frac{\int_0^E \frac{d\mathcal{P}}{dE'} dE'}{\int_0^\infty \frac{d\mathcal{P}}{dE'} dE'} = rand\,, \tag{3.23}$$

where $rand$ is some random number. However, since one cannot integrate Equation 3.22 analytically, one can again use the Monte-Carlo technique. To do this, a random number, say E_{rand}, is picked from $E_{min} = 0.01\,\text{keV}$ to $E_{max} = 20\,\text{keV}$. Then, another random number, say $\left(\frac{d\mathcal{P}}{dE}\right)_{rand}$, is picked from $\left(\frac{d\mathcal{P}}{dE}\right)_{min}$ to $\left(\frac{d\mathcal{P}}{dE}\right)_{max}$. Note that the values of $\left(\frac{d\mathcal{P}}{dE}\right)_{min}$ and $\left(\frac{d\mathcal{P}}{dE}\right)_{max}$ depend on how the function $\frac{d\mathcal{P}}{dE}$ is normalized. Then, if $\left(\frac{d\mathcal{P}}{dE}\right)_{rand} \leq \frac{d\mathcal{P}}{dE}\Big|_{E=E_{rand}}$, one obtains E_{rand}. If this algorithm is repeated a large number of times, the set of energies obtained will follow the desired distribution.

3.2.3 X-ray Mean Free Path

For every E_{rand} generated, the mean free path (λ), must be computed. Recall that

$$\lambda = \frac{1}{n\sigma}\,, \tag{3.24}$$

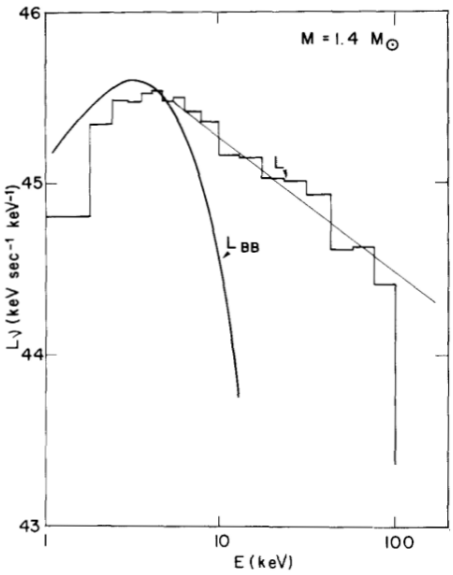

Figure 3.3: Simulated X-ray spectrum of a $1.4\,M_{\odot}$ neutron star that follows a black-body distribution for $E \lesssim 5\,keV$ and a power law function at higher energies (taken from Tuchman & Yahel [168]).

where σ is the total X-ray absorption cross-section. Following Vilhu et al. [174], σ is computed using the neutral element photoelectric absorption from Morrison & McCammon [103], the free-free absorption by protons (H-ions) and He-ions from Basko & Sunyaev [10], and the free electron scattering is handled by the Thomson cross-section. Therefore,

$$\lambda = \frac{1}{n_{neutral}\sigma_{neutral} + k_{ff} + n_e\sigma_T}\,. \tag{3.25}$$

Morrison & McCammon [103] computed the cross-section of photons in the range $0.03 - 10\,\mathrm{keV}$ for typical cosmic abundances due to neutral elements. Since one expects no neutral Hydrogen and no neutral Helium to be present in the donor star, the cross-section is taken to be 0 for $E \lesssim 0.12\,\mathrm{keV}$ (see Figure 3.4). For higher energies, the cross-section curve has discontinuities due to the K-shell absorption edges of the element indicated in Figure 3.4. However, it is still a good approximation to use a linear interpolation formula (see Longair [92]),

$$\frac{\sigma_{neutral}(E)}{\mathrm{cm}^2} = 2 \times 10^{-22} \left(\frac{E}{\mathrm{keV}}\right)^{-\frac{8}{3}}\,. \tag{3.26}$$

One still has to subtract the neutral Hydrogen and neutral Helium from this equation for $E \gtrsim 0.12\,\mathrm{keV}$. One can approximate the H + He curve in Figure 3.4 with the following

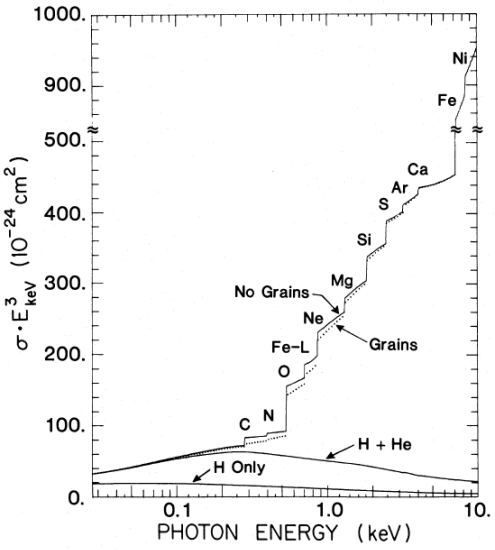

Figure 3.4: X-ray cross-section for neutral Hydrogen, Helium, and heavy elements (taken from Morrison & McCammon [103]).

fitting function,

$$\frac{\sigma_{H+He}(E)}{10^{-24}\,\mathrm{cm}^2} = \frac{51.4772 - 27.4443\log\left(\frac{E}{\mathrm{keV}}\right) - 13.3857\log\left(\frac{E}{\mathrm{keV}}\right)^2 + 9.4055\log\left(\frac{E}{\mathrm{keV}}\right)^3}{\left(\frac{E}{\mathrm{keV}}\right)^3}\,, \quad (3.27)$$

where log is the logarithm base 10. Thus, the final cross-section due to heavy neutral elements is

$$\sigma_X(E) \equiv \sigma_{neutral}(E) - \sigma_{H+He}(E)\,. \quad (3.28)$$

The number density of neutral elements, $n_{neutral}$, is computed as follows:

$$n_{neutral} = \frac{\langle\rho\rangle\, N_A}{\mu}\,, \quad (3.29)$$

where $\langle\rho\rangle$ is the averaged density of the donor star and $\mu/N_A \approx 2.16\times10^{-24}$ g is the averaged mass of the neutral elements (computed from the cosmic abundances used by Morrison & McCammon [103]). Obviously, the mass density changes as the X-rays travel in the donor star. For this reason, the averaged mass density is computed at every shell k, from the surface to that shell. Thus,

$$\langle\rho\rangle_k = \frac{1}{k}\sum_{i=1}^{k}\rho_i\,, \quad (3.30)$$

where the mass density ρ_i at the center of shell i is given by the `MESA` code.

As mentioned previously, the free-free absorption by protons (H-ions) and He-ions is computed following Basko & Sunyaev [10]. So,

$$k_{ff} = 3.7 \times 10^8 N_e \left(\sum_i N_i Z_i^2 \right) T^{-\frac{1}{2}} \left(\frac{E}{h} \right)^{-3} \left(1 - e^{-\frac{E}{k_B T}} \right) \text{cm}^{-1} \,, \tag{3.31}$$

where N_e and N_i are the number of electrons and ions of charge Z_i per unit volume, respectively, T is the temperature of the donor star, and h is Planck's constant. Considering only H and He ions, k_{ff} is computed as follows,

$$k_{ff} = 3.7 \times 10^8 n_{neutral}^2 \langle y \rangle \left(0.9078 + 4 \times 0.0908 \right) \langle T \rangle^{-\frac{1}{2}} \left(\frac{E}{h} \right)^{-3} \left(1 - e^{-\frac{E}{k_B \langle T \rangle}} \right) \text{cm}^{-1} \,, \tag{3.32}$$

where y is the mean number of free electrons per nucleon assuming complete ionization (which is computed by the `MESA` code), 0.9078 and 0.0908 are the fractions of H and He ions respectively, and again, $\langle\rangle$ represents the average from the surface down to shell k.

Finally, considering free electron scattering, the Thomson cross-section is well known to be $\sigma_T = 6.6524 \times 10^{-25}\,\text{cm}^2$, and the number of free electrons, n_e, is calculated by the `MESA` code.

It turns out that the neutral heavy elements absorption is by far the dominant source of interaction with the X-ray photons. Indeed, a few computations showed that $n_{neutral}\sigma_X \gg k_{ff}$ and $n_{neutral}\sigma_X \gg n_e\sigma_T$. Thus, the mean free path for an X-ray photon of energy E can be simply written as

$$\lambda(E) = \frac{1}{n_{neutral}\sigma_X + k_{ff} + n_e\sigma_T} \cong \frac{1}{n_{neutral}\sigma_{neutral}} = \frac{\mu}{N_A \langle \rho \rangle_k \sigma_X(E)} \,. \tag{3.33}$$

Rather than following Morrison & McCammon 1983 [103] to compute $\sigma_X(E)$ (which is only good for cosmic abundances of elements), one can compute the cross section $\sigma_Z(E)$ for each neutral element of atomic number Z following Verner & Yakovlev 1995. Then, the total cross section is simply

$$\sigma_X(E) = \sum_Z \sigma_Z(E) \frac{n_Z}{n_H} = \frac{1}{n_H} \sum_Z \sigma_Z(E) n_Z \,, \tag{3.34}$$

where n_Z is the number density of the elements of atomic number Z and n_H is the number density of hydrogen atoms. Then, the column depth becomes

$$d\tau_X = \kappa_X \rho dz \,, \tag{3.35}$$

where $\kappa_X = \sigma_X n_H/\rho$, so using Equation 3.34, one gets

$$d\tau_X = \sigma_X n_H dz = \left(\frac{1}{n_H} \sum_Z \sigma_Z n_Z \right) n_H dz = \left(\sum_Z \sigma_Z n_Z \right) dz \,. \tag{3.36}$$

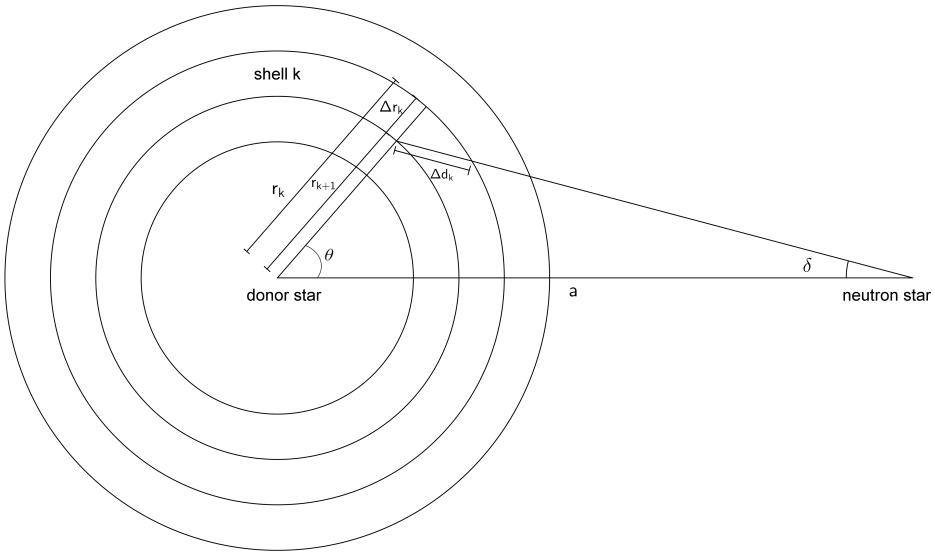

Figure 3.5: Geometry of X-ray Binaries. The figure shows that an X-ray penetrating down to shell k does not travel the same distance depending on its angle of incidence. The relation between Δr_k and Δd_k is discussed in the text.

Recalling that $d\tau = \frac{1}{\lambda} dz$, one concludes that

$$\lambda(E) = \frac{1}{\sum_Z \sigma_Z(E) n_Z} \,. \tag{3.37}$$

3.2.4 Geometry of X-ray Binary Systems

It has been seen in Section 3.1 that the angle of incidence of the X-ray photons modifies the irradiation flux. Furthermore, as will be shown in this section, the penetration depth of X-rays is not the same for different angles of incidence (see Figure 3.5).

It can be shown that at a certain shell k inside the donor star, the radial thickness of the shell, Δr_k, and the distance traveled by an X-ray photon, Δd_k, are related by the following equation,

$$\Delta d_k(\delta) = \sqrt{r_k^2 - a^2 \sin^2 \delta} - \sqrt{r_{k+1}^2 - a^2 \sin^2 \delta} \,, \tag{3.38}$$

where the angle δ is shown in Figure 3.5. A proof of this equation can be found in Appendix A.2.

The effect of this angle must be taken into account in the Monte-Carlo simulations. Thus, for every X-ray energy randomly generated, a random angle is generated. Since one assumes that the neutron star emits X-rays isotropically, one linearly selects a random

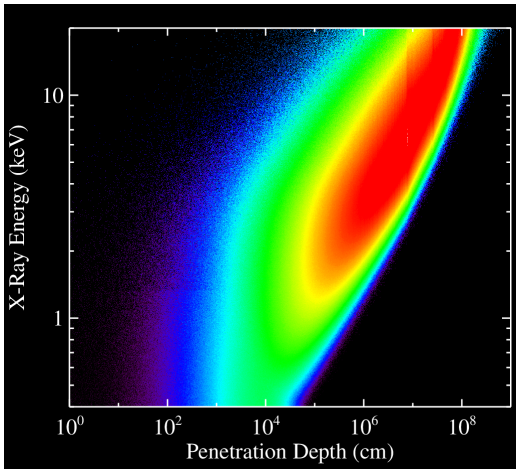

Figure 3.6: X-ray energy as a function of penetration depth below the photosphere using the Monte-Carlo method described in Section 3.2.5. For this example, a non-evolved $1.0\,M_\odot$ donor star was used. The color coding shows the relative logarithmic probability that an X-ray photon of a given energy has to travel a given depth below the photosphere. Red is 5 times more probable than yellow, 10 times more than green, 50 times more than cyan, and 500 times more than purple.

angle, δ_{rand}, between 0 and $\delta_{max} = \arcsin\left(\frac{R_2}{a}\right)$. In other words, for a random number $rand$, $\delta_{rand} = rand \cdot \arcsin\left(\frac{R_2}{a}\right)$. Then, the goal is to find at what shell k is an X-ray photon of energy E_{rand} going to travel a distance z, where z is given by equation 3.21. Thus, the following equation is solved for k,

$$\sum_{i=0}^{k} \Delta d_i(\delta_{rand}) = z\,, \tag{3.39}$$

and one obtains the final penetration depth for the given shell k, i.e., an energy E_{rand} is deposited in shell k.

3.2.5 Calculation

The methodology that was adopted is as follows: An energy E_{rand} is generated such that it follows the distribution given by Equation 3.22. Then, a random angle δ_{rand} is generated as well as another random number, $rand$. Then, one computes $\sum_{i=0}^{k} \Delta d_i(\delta_{rand})$ and $z_k = -\frac{\mu}{\langle\rho\rangle_k \sigma_X(E_{rand})} \ln(rand)$ for $k = 0$, 1, 2, ..., and when one quantity becomes sufficiently close to the other, one obtains the shell number k where the energy is deposited.

Figure 3.6 shows an example of the method outlined in the previous sections. In this example, the penetration depth is computed for a $1.0\,M_\odot$ unevolved donor star. The red

region of Figure 3.6 indicates the depth where it is most probable that photons deposit their energy. Thus, in this example, photons would be intercepted in between $\simeq 1\,\mathrm{km}$ and $\simeq 1000\,\mathrm{km}$ below the photosphere. These depths correspond to column depths of approximately $2.1\times10^{-2}\,\mathrm{g/cm^2}$ and $1.7\times10^{2}\,\mathrm{g/cm^2}$. The standard value of $1\,\mathrm{g/cm^2}$ for X-rays corresponds to a depth of roughly $4\times10^{6}\,\mathrm{cm}$. Thus, the Monte-Carlo simulation shows that some X-rays would be intercepted before the standard column depth and some would penetrate deeper than $1\,\mathrm{g/cm^2}$.

Once the Monte-Carlo simulation is done, it is important to add the correct amount of energy in the donor star, i.e. the correct ϵ_{irr} must be computed at every shell k where energy is deposited. Note that one can write

$$\epsilon_{irr,k} = \frac{dL_{irr,k}}{dm_k} \cong \frac{L_{irr,k} - L_{irr,k+1}}{\Delta m_k}\,, \tag{3.40}$$

where Δm_k is given by the `MESA` code. In general, one can write from simple geometry

$$L_{irr,k} = F_{irr}\int_{-\phi_{max,k}}^{\phi_{max,k}}\int_{-\theta_{max,k}}^{\theta_{max,k}} r_k^2\sin\theta\,d\theta d\phi\,, \tag{3.41}$$

where F_{irr} is given by Equation 3.3. Looking at Figure 3.5, one can see that $\theta_{max,k} = \arccos\left(\frac{r_k}{a}\right)$, and by spherical symmetry, $\phi_{max,k} = \theta_{max,k}$. So, one gets

$$L_{irr,k} = 4F_{irr}r_k^2\left[\phi\right]_0^{\arccos\left(\frac{r_k}{a}\right)}\left[-\cos\theta\right]_0^{\arccos\left(\frac{r_k}{a}\right)} = 4F_{irr}r_k^2\left(1-\frac{r_k}{a}\right)\arccos\left(\frac{r_k}{a}\right). \tag{3.42}$$

If a total energy E_k is deposited in shell k throughout the Monte-Carlo simulation, then

$$\epsilon_{irr,k} \cong \frac{1}{\Delta m_k}\frac{4F_{irr}\left[r_k^2\left(1-\frac{r_k}{a}\right)\arccos\left(\frac{r_k}{a}\right)E_k - r_{k+1}^2\left(1-\frac{r_{k+1}}{a}\right)\arccos\left(\frac{r_{k+1}}{a}\right)E_{k+1}\right]}{\sum_k E_k}\,, \tag{3.43}$$

where the sum is over all shells k of the donor star. Then, one simply adds this value of $\epsilon_{irr,k}$ in Equation 3.17 (for every shell k).

3.2.6 Non-Spherical Irradiation and the Uncertainty of η

It is important to note at this point that the model developed above assumes spherical irradiation, that is to say that as soon as an X-ray photon deposits some energy in a shell k, then the energy of the entire shell is instantaneously increased. However, it is obvious that while irradiation happens, there is a "dark side" of the donor star that is not heated and that does not receive any extra energy. Since the `MESA` code is only a one-dimensional code (it assumes spherical symmetry), one cannot easily model non-spherical irradiation. The other issue concerns the overall shape of the star (i.e., Roche geometry). Neither of these two effects have been taken into account (note that the second one is much smaller).

The issue of non-spherical irradiation has been explored by Hameury et al. [55] and they came to the conclusion that the spherically symmetric model is good enough if the circulation flow is supersonic and if $\eta \sim 1$. Unfortunately, both conditions are probably not met most of the time. On the other hand, Vilhu et al. [174] showed that if the energy is deposited in a convective region of the donor star, then the heat is distributed all around the star in a short thermal time scale relative to the evolutionary time scale.

Furthermore, it is known that there is a lot of uncertainty in the value of the efficiency factor η. Thus, it can be assumed that the errors behind spherical irradiation instead of non-spherical irradiation are included in the uncertainty of η. In fact, one can expect that non-spherical irradiation is equivalent to having smaller values of η. For example, Vilhu et al. [174] claim that, given the relatively fast redistribution of heat around the star, $\eta = 0.1$ is well justified with the assumption of spherical heating.

Let us recall that there is also some uncertainty in the radius of the neutron star (see Section 2.3.2), which comes into play in the equation for the irradiation flux (see Equation 3.3). Therefore, one can fix a given value for R_1, and again, claim that the uncertainty of R_1 gets transferred in the uncertainty of η. As discussed in Section 2.3.2, Guillot et al. [53] seem to indicate that neutron stars have smaller radii that the value used in this thesis. This would thus imply that slightly larger values of η are favored, but this would be a very small change.

3.3 Evolution with Irradiation

Now that the theory behind X-ray irradiation and how it can be implemented in the `MESA` code has been developed, one can recompute the evolution of LMXBs and IMXBs and compare the tracks with the previous results.

It is important to note at this point that the effects of X-ray irradiation complicate the computer simulations. Indeed, since energy is added in the outer shells of the donor star, the star suddenly finds itself with large temperature and luminosity gradients inside the envelope. These gradients significantly increase in magnitude within a few time steps. When this happens, if the `MESA` code does not decrease its time step sufficiently, it will not be able to converge to a solution, i.e. the code will crash. On the other hand, if the `MESA` code reduces the time step too much (down to seconds sometimes) to compensate for the large gradients, then the code will take an enormous amount of time to simulate only a few years of evolution. The solution to this issue resides in finding the best mesh controls (in order to have more shells near the region where energy is deposited) and the best time step controls, i.e. finding limits on the time steps change depending on particular values of the temperature and luminosity gradients. In the end, this allows one to successfully run the `MESA` code, but there are still some situations where either the code does not converge or it takes an "infinite" time to compute the entire evolution. And, in general, even when the

code converges successfully within an appropriate amount of time, it is important to note that the overall computing time is increased significantly.

3.3.1 Radius Increase

Before doing any evolutionary computations, it is important to verify that our X-ray irradiation model behaves as expected. To do this, one can try to reproduce Podsiadlowski's [120] results (recall Figure 3.1). The goal is to observe that for low irradiation fluxes, the donor star's radius remains the same, and then for increasing fluxes, the donor star bloats up before reaching a maximum value (the "plateau").

Here is how this computation is done. First, the donor star is removed from the binary system since it must not interact with the neutron star (one simply has to set the initial orbital period to be extremely large). Second, one artificially turns off nuclear reactions so that, without any external influence, the star's radius would remain constant through time. Third, one artificially irradiates the star at a constant flux for a sufficiently large amount of time so that the star reaches thermal equilibrium again.

Figure 3.7 shows the results of the computations described above. Note that the computations are performed for different donor star masses. First, one notes that for $\log\left(\frac{F_{irr}}{\mathrm{erg\,s^{-1}cm^2}}\right) \lesssim 11.0$, the constant heating does not perturb the donor star's radius significantly. However, for $11.0 \lesssim \log\left(\frac{F_{irr}}{\mathrm{erg\,s^{-1}cm^2}}\right) \lesssim 11.8$, the donor star seriously bloats up, and the less massive the star is, the larger the effect. In fact, Figure 3.7 shows that for $M = 1.5\,M_\odot$, the constant irradiation flux barely modifies the star's equilibrium properties. Then, for $\log\left(\frac{F_{irr}}{\mathrm{erg\,s^{-1}cm^2}}\right) \gtrsim 11.8$, the effect of increasing the irradiation flux does not modify the star's radius very noticeably.

The general behavior of the donor star under X-ray irradiation found here matches the results of Podsiadlowski [120]. The major difference is that in Podsiadlowski's results, the radius increase of the donor stars becomes important for smaller irradiation fluxes ($\log\left(F_{irr}/\mathrm{erg\,s^{-1}cm^2}\right) \simeq 10.2$). But one has to recall that Podsiadlowski's method (changing the boundary conditions of the star) and the one described in this thesis (Monte-Carlo simulation and deposition of energy inside the star) are rather different.

3.3.2 Evolutionary Tracks

This section shows the evolutionary tracks of X-ray binaries with the same initial conditions than the ones shown in Section 2.4.2 but with the effects of X-ray irradiation. Note that for the following, the efficiency factor is taken to be $\eta = 0.1$. Other values of η are explored in Section 4.2.1.

First, one notes that Figure 3.8 is fairly similar to Figure 2.10 (no irradiation for that case). However, there is a major difference if one looks at the mass-transfer rate. With irradiation, the first peak seems to have two mass-transfer phases rather than only one

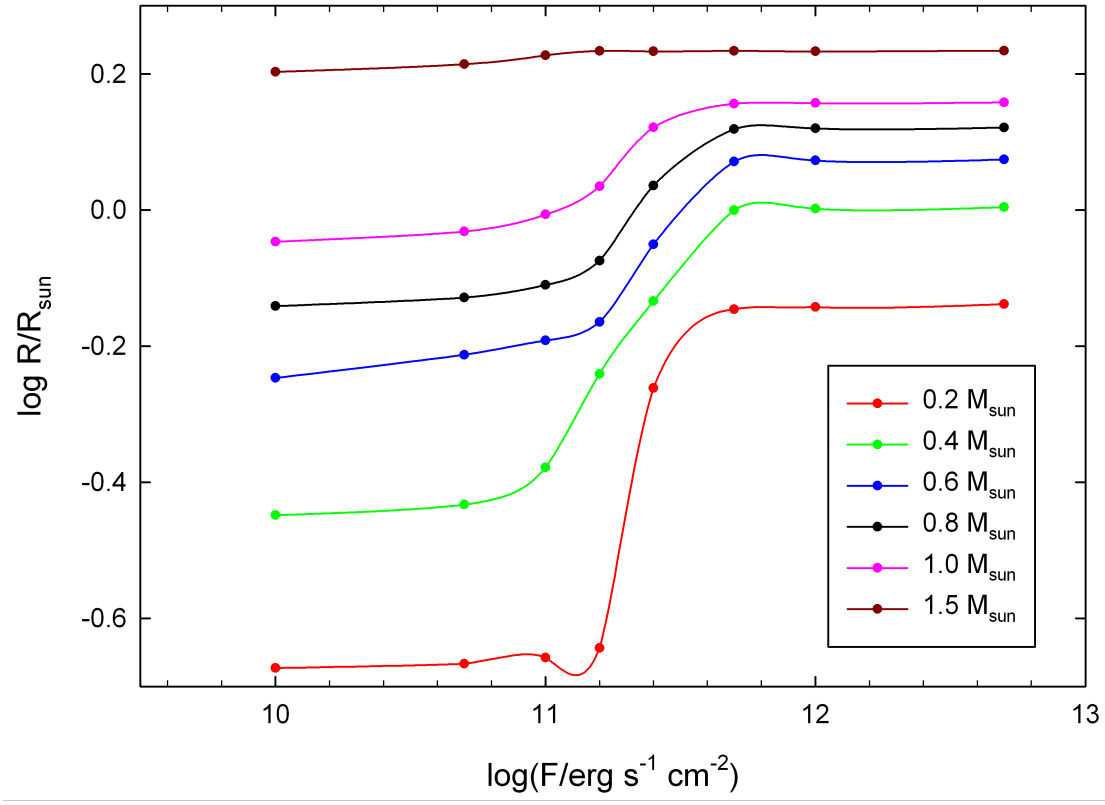

Figure 3.7: Evolution of isolated donor stars of different masses under constant X-ray irradiation and without nuclear burning. The graph shows the equilibrium radius (R) as a function of the external irradiation flux (F) for unevolved stars. Note that the bumpy feature of the red curve right after $F = 10^{11}\,\mathrm{erg\,s^{-1}\,cm^2}$ is only due to the limitation of the program used to fit a spline curve to the data points.

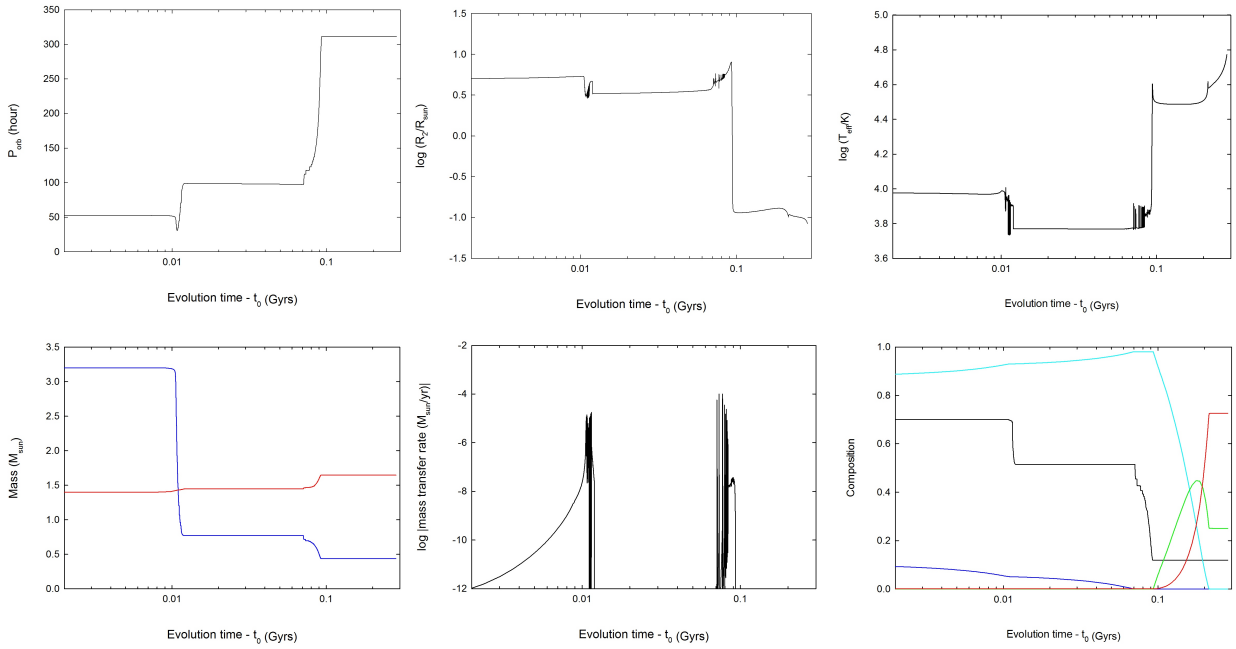

Figure 3.8: Same description for the graphs as for Figure 2.10 with the same initial conditions. The final values are $M_{1,f} \cong 1.65\,M_\odot$, $M_{2,f} \cong 0.44\,M_\odot$ and $P_{orb,f} \cong 311.2$ hr.

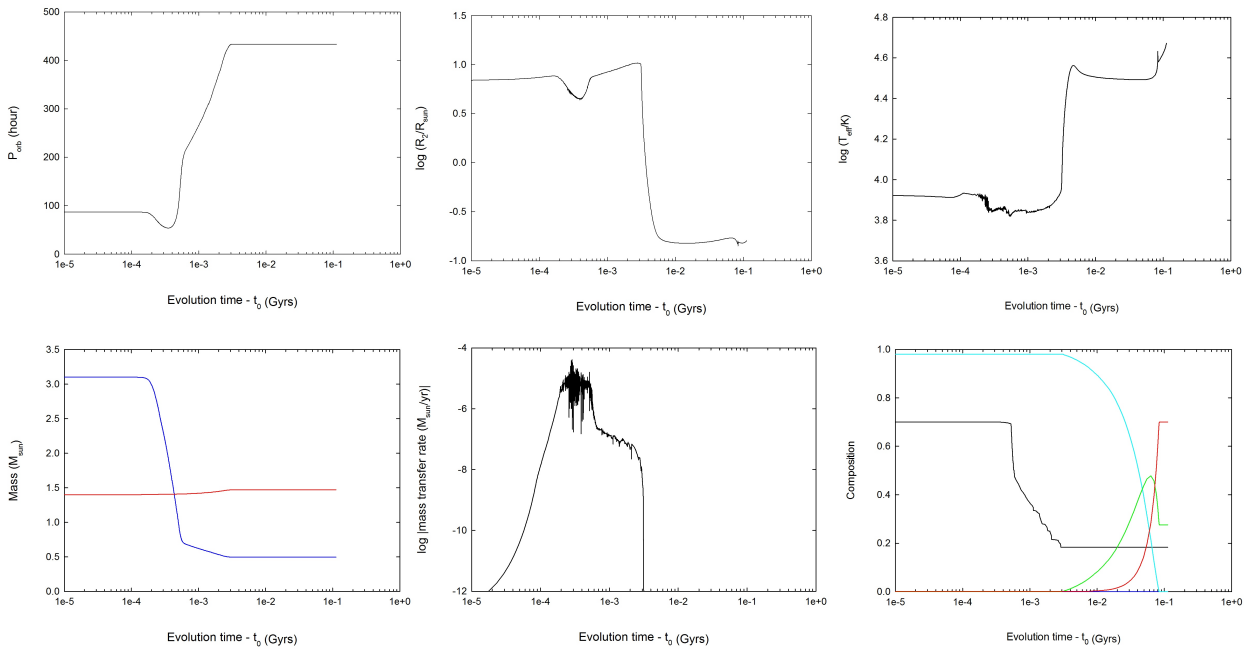

Figure 3.9: Same description for the graphs as for Figure 2.11 with the same initial conditions 2.11. The final values are $M_{1,f} \cong 1.47\,M_\odot$, $M_{2,f} \cong 0.50\,M_\odot$ and $P_{orb,f} \cong 433.5$ hr.

as is found without irradiation. Then, there is no plateau in the mass-transfer rate with irradiation. Also, the second peak is a lot different. With irradiation, there are many peaks that reach close to $10^{-4}\,M_\odot/\text{yr}$, which is well above the Eddington limit. This is an example of "irradiation cycles", which is discussed in more depth in the following section. Because of that, the second mass-transfer phase does not favor the accretion of mass onto the neutron star as much as it does without irradiation. Thus, although the end values for the orbital period and the mass of the donor star are similar, the mass of the neutron star is quite smaller with irradiation.

Comparing Figure 3.9 with Figure 2.11, there are almost no differences. In fact, the end values are basically identical. Thus, for this particular set of initial conditions, irradiation has almost no effect on the evolution.

As opposed to the last figure, Figure 3.10 shows a completely different behavior compared to the evolution without irradiation (Figure 2.12). Indeed, with irradiation, the mass-transfer rate shows one long mass-transfer phase followed by a short phase, which is then followed by a large number of irradiation cycles. In the end, the values are all very different (the neutron star is much less massive, the orbital period is smaller, and the donor star is less massive).

Figure 3.11 shows irradiation cycles that make the evolution seem very different than its

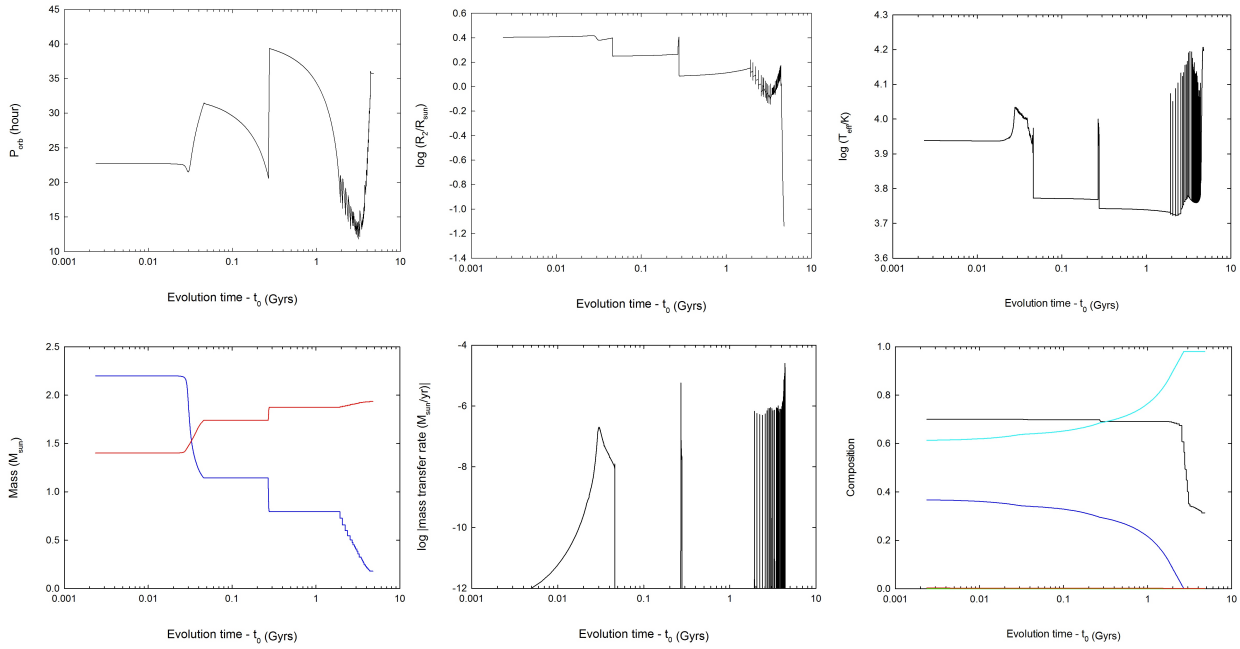

Figure 3.10: Same description for the graphs as for Figure 2.12 with the same initial conditions. The final values are $M_{1,f} \cong 1.93\, M_\odot$, $M_{2,f} \cong 0.18\, M_\odot$ and $P_{orb,f} \cong 35.8$ hr.

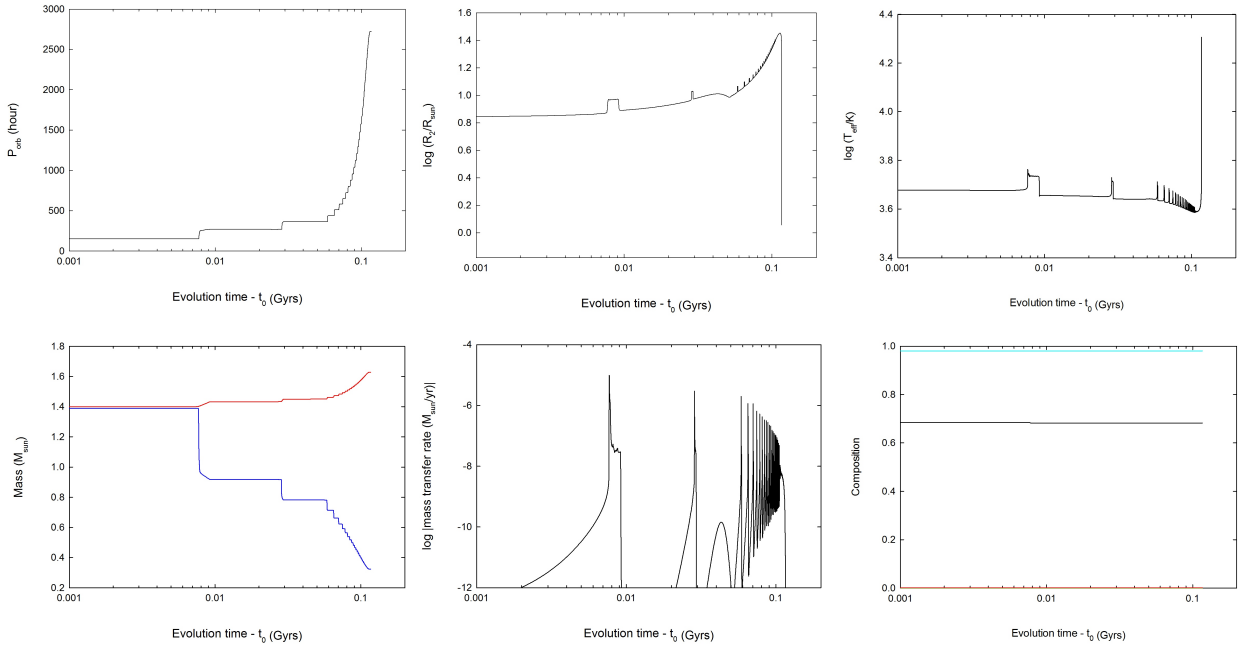

Figure 3.11: Same description for the graphs as for Figure 2.13 with the same initial conditions. The final values are $M_{1,f} \cong 1.63\, M_\odot$, $M_{2,f} \cong 0.32\, M_\odot$ and $P_{orb,f} \cong 2728.0$ hr.

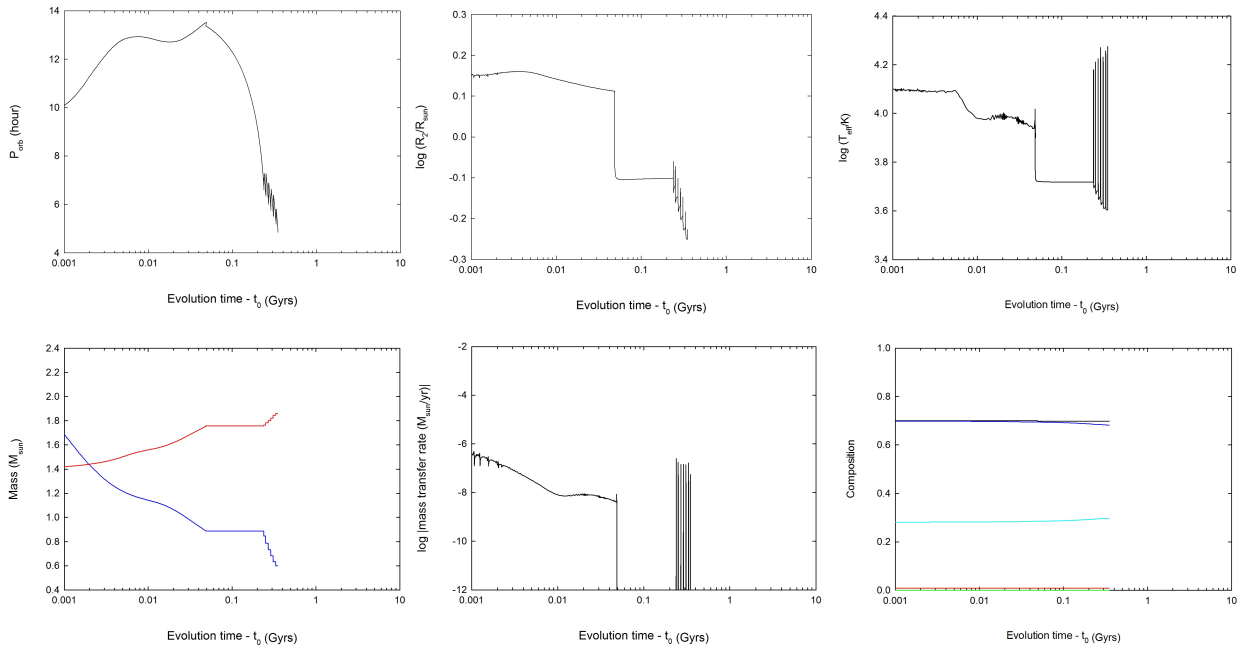

Figure 3.12: Same description for the graphs as for Figure 2.10. The initial conditions for this evolution are $M_{1,i} = 1.4\,M_{\odot}$, $M_{2,i} = 2.15\,M_{\odot}$ and $P_{orb,i} = 10.0$ hr.

non-irradiation counterpart. A very similar system is analyzed in more detail in the following section. Note that the final donor star mass and the final orbital period are very similar to the non-irradiated case, but the final neutron star mass is much smaller once again.

Finally, Figure 3.12 shows the evolution of an X-ray binary system that evolves as a CV-like system (see Section 2.4.1 for discussion of CV-like systems). The evolution of this particular system has not been shown previously without irradiation. The goal here is not to compare with non-irradiated simulations, but to show why this type of evolution is very demanding computationally. Looking at the effective temperature, one sees that the irradiation cycles lead to enormous changes. Every large change in T_{eff} makes it difficult for the code to converge. It has to reduce the time step to very small values, but this in turns slows the code significantly, i.e. the computational time is increased. It is for this reason that the computations of CV-like systems with irradiation are ignored in this work.

3.3.2.1 Irradiation Cycles

The goal of this section is to explain irradiation cycles. Let us start by looking at the mass-transfer rate. Looking at Figure 3.13, when the mass transfer starts at $\simeq 3.55 \times 10^9$ years, the mass-transfer rate for the irradiated system (blue curve) and for the non-

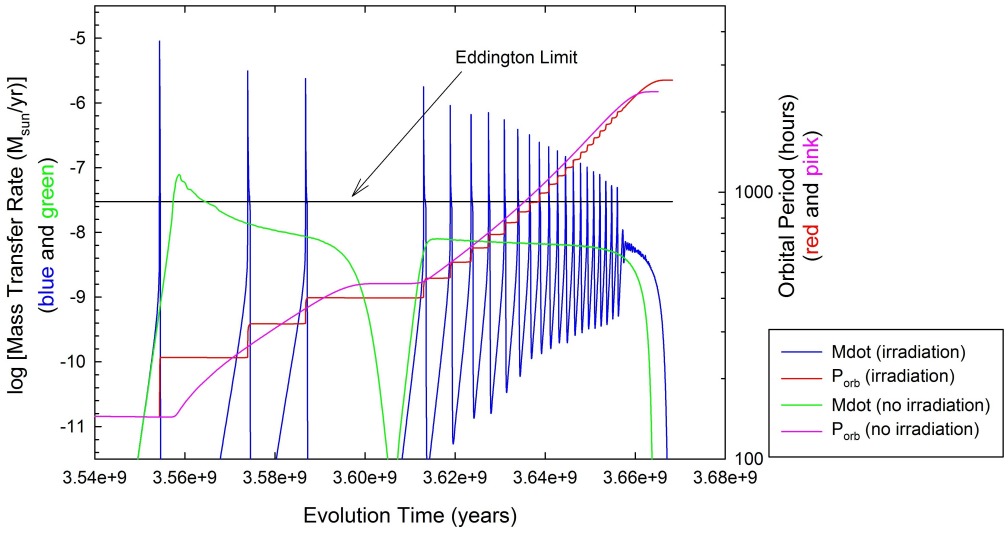

Figure 3.13: Comparison of the evolution of an X-ray binary system with and without irradiation. The evolutionary tracks depict a $1.39\,M_\odot$ donor star losing mass to an initially $1.4\,M_\odot$ neutron star with an initial period of 151.4 hr.

irradiated system (green curve) show identical behavior. As the mass-transfer rate increases, the donor star bloats up under X-ray irradiation and the mass-transfer rate increases even more rapidly. Thus, the two curves separate from one another. For the irradiated case, the mass-transfer rate peaks at $\simeq 10^{-5}\,M_\odot$/yr while for the non-irradiated case, the rate is still at $\simeq 10^{-9}\,M_\odot$/yr.

Now, looking at the orbital period, one sees that for the irradiated case, while the mass-transfer rate is very large, the orbital period increases suddenly (red curve). Recalling Equation 2.40 for the Roche lobe radius, the increase in binary separation (which is the same as an increase in orbital period) increases the Roche lobe radius. Thus, at one point, the donor star does not overflow the Roche lobe anymore and the mass transfer has to stop. This is why the mass-transfer rate for the irradiated case drops at $\simeq 3.555 \times 10^9$ years.

For the non-irradiated case, the mass-transfer rate does not peak at a high value, so the orbital period increases only smoothly (pink curve), and thus, mass is transferred continuously throughout the evolution. For the irradiated case, the sudden increase in binary separation stops the mass transfer and it is only nuclear evolution that can increase the radius of the donor star to bring the stars back into contact. Then, at $\simeq 3.57 \times 10^9$ years, the mass transfer starts all over again, peaking shortly later with a very high value. This process then repeats itself several times. These cycles in the mass-transfer rate are called irradiation cycles.

Overall, although the orbital period increases step wise with irradiation and continuously

without irradiation, the final orbital periods are quite close to one another at the end of the evolution. However, the major difference comes from the mass that the neutron star can accrete in both processes. Indeed, without irradiation, the mass-transfer rate stays (for the majority of the evolution) below the Eddington limit. For the irradiated case, all the mass-transfer peaks are a few orders of magnitude above the Eddington limit, which implies that system looses a lot of mass. Therefore, the non-irradiated X-ray binary ends up with a massive neutron star and the irradiated X-ray binary ends up with a much less massive neutron star.

Chapter 4

X-ray Irradiation: The Results

4.1 New Evolutionary Grids with Irradiation

Now that a model for the effects of self-induced X-ray irradiation has been implemented in the `MESA` code, one can compute an evolutionary grid. As described in Section 2.4.2, the evolution of 4,200 LMXBs and IMXBs is computed, where $M_{1,i} = 1.4\,M_\odot$, $M_{2,i} = 1-4\,M_\odot$ in increments of $0.05\,M_\odot$, and $P_{orb,i} = 10 - 250\,\mathrm{hrs}$ in increments of 0.02 in the log scale. This evolutionary grid is then computed for different values of the irradiation efficiency factor introduced in the previous chapter. The values are taken to be $\eta = 0.05$, 0.10, 0.50, and 1.00. This will show the effects of irradiation if only a limited X-ray flux reaches the donor star (e.g., 5%), and at the opposite end, if the donor star is fully irradiated (100%). One do not expect full irradiation, but the calculations with $\eta = 1$ are still carried out, allowing us to rule it out with more than heuristic arguments.

Let us note that for these computations with irradiation, the evolutionary paths of CV-like systems and ultracompacts were not computed. Indeed, as discussed in Section 3.3.2, CV-like systems tend to have many irradiation cycles with very large variations in surface temperature making the computations for the donor star very difficult. Thus, if for a given track the donor star evolved under $0.6\,M_\odot$ and the orbital period evolved below 5 hours, then the computation was simply stopped.

Figure 4.1 shows an example of evolutionary grid with irradiation with $\eta = 0.5$. As explained in the previous paragraph, no CV-like or ultracompact tracks are found in the grid. Comparing this Figure with panel a) of Figure 2.8, a few differences can be observed. First, the colors are not the same. As seen in Section 3.3.2 and 3.3.2.1, when irradiation is included, the mass-transfer phases are very intense but do not last for a long amount of time. However, it is during those phases that the mass of the star and the orbital period change. Thus, where one saw green in Figure 2.8, one now sees mainly blue (which indicates a lower relative probability) in this figure. However, if one looks carefully at Figure 4.1, one will

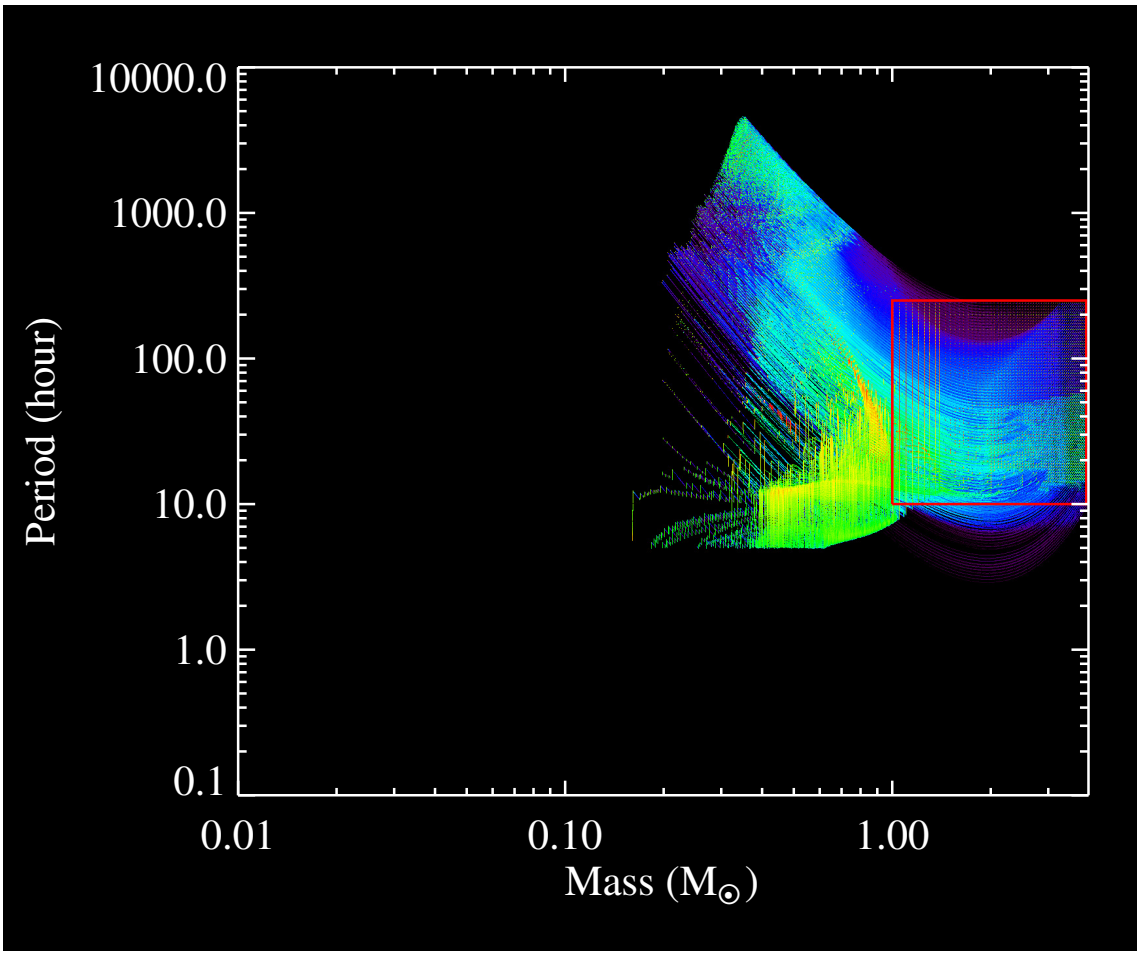

Figure 4.1: Evolutionary grid with the effects of self-induced irradiation. The irradiation efficiency factor is $\eta = 0.5$.

see that there are many small yellow and red points, which indicate small regions of higher relative probability. In fact, these points are due to the much longer quiescent phases in the irradiation cycles, i.e. when there is no mass transfer. Moreover, it is possible to observe irradiation cycles in this period-mass plot if one looks at the systems that evolve towards CV-like evolution (smaller orbital periods). There is one last feature to note that is not found in the non-irradiated grid. If one looks at Figure 4.1 for $M_2 \simeq 0.2\,M_\odot$ and $P_{orb} \simeq 400$ hours, one will see that there seems to be a number of tracks that evolved further than the previously obtained period-mass relation in this region. This will be discussed in more depth in the next section.

4.2 New End Points with Irradiation

4.2.1 The Effects of Changing the Efficiency Factor η

Now, let us look at the end points of the evolutionary grids that were computed with the effects of irradiation. Figure 4.2 shows the final orbital period as a function of the final donor star mass. Let us recall that without irradiation ($\eta = 0$), good results had already been obtained, i.e. results that matched most of the observed binary millisecond pulsars. Therefore, including the effects of irradiation cannot cause a large divergence from these results. If the results do diverge, then it might be an indication that the irradiation model is not physical.

In general, results for $\eta = 0$ and $\eta > 0$ seem to agree quite well with one another. There are a few regions though where the results differ. First, in the region delimited by $M_{2,f} \simeq 0.3 - 0.45\,M_\odot$ and $P_{orb,f} \simeq 200 - 600$ hours, all colored dots (irradiation) match one another, but they all slightly diverge towards smaller donor star masses with respect to the black dots (no irradiation) of the same final orbital periods. Second, along the period-mass relation (blue-green line in Figure 4.2) for $P_{orb,f} \lesssim 300$ hours, it looks as if irradiation produces systems with slightly larger final orbital periods with respect to the black dots (no irradiation) of the same donor star masses. Finally, there is a region that shows divergence among the different efficiency factors. This region, observed in the previous section around $P_{orb,f} \simeq 300 - 1000$ hours and $M_{2,f} \simeq 0.19 - 0.23\,M_\odot$ shows systems that evolved significantly further than the period-mass relation. However, this occurs only for $\eta = 0.5$ and $\eta = 1.0$, which might be an indication that irradiation with large efficiency factors ($\gtrsim 0.5$) is not physical. This would imply that at least half the X-rays would be intercepted before reaching the photosphere of the donor star. However, recall that the efficiency factor accounts for other uncertainties (such as spherical heating and the radius of the neutron star), so one has to be careful before making such a conclusion.

Now, let us look at Figure 4.3 where one see the final neutron star mass as a function of the final donor star mass. This time, it is obvious that irradiation has a strong effect on the

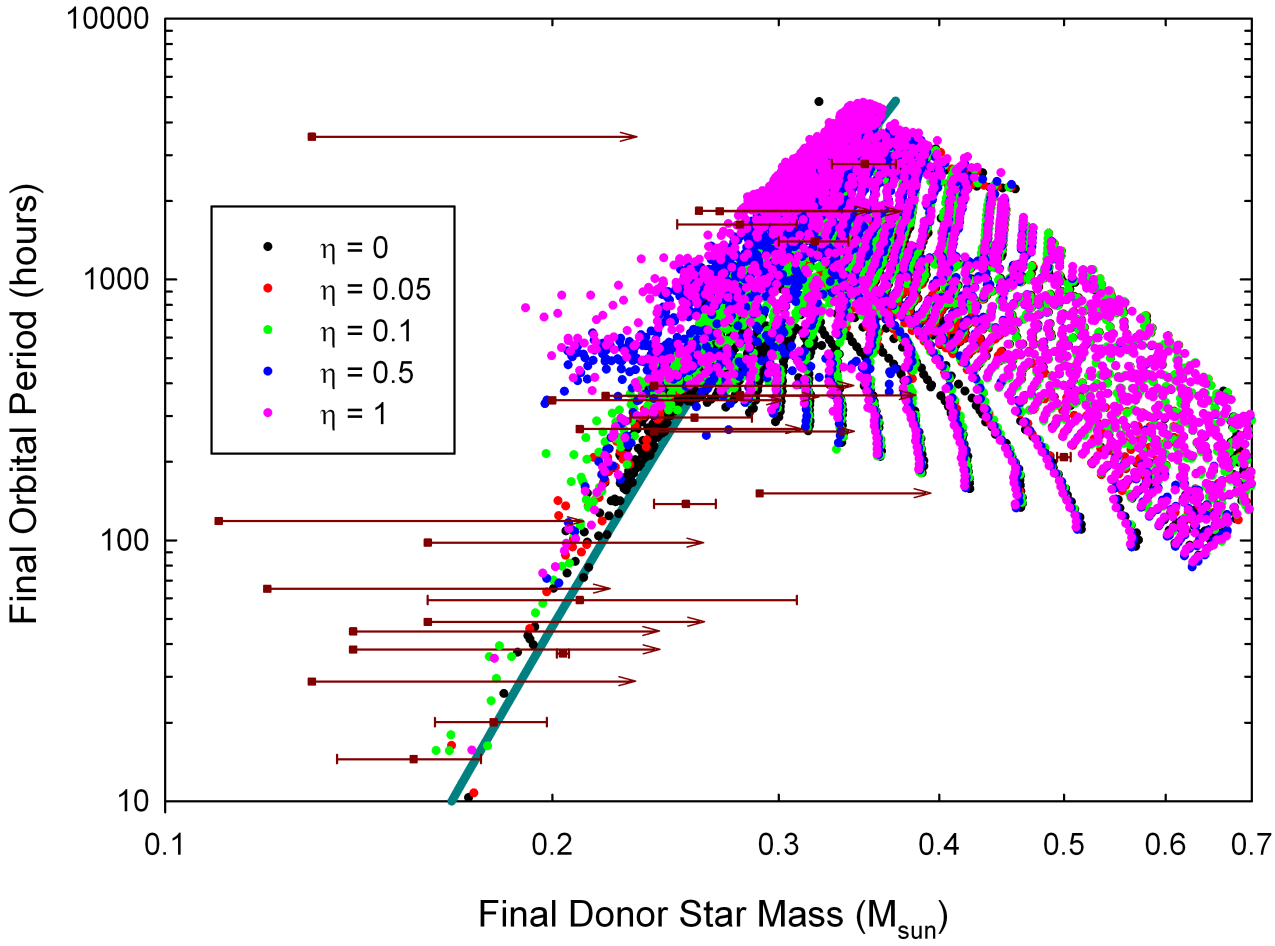

Figure 4.2: End points of the evolutionary grids with the effects of irradiation comparing $\eta = 0.0$ (no irradiation), 0.05, 0.10, 0.50, and 1.0 (full irradiation). This is a graph of the final orbital period as a function of the final donor star mass. The blue-green line is the period-mass relation of Lin et al. [90].

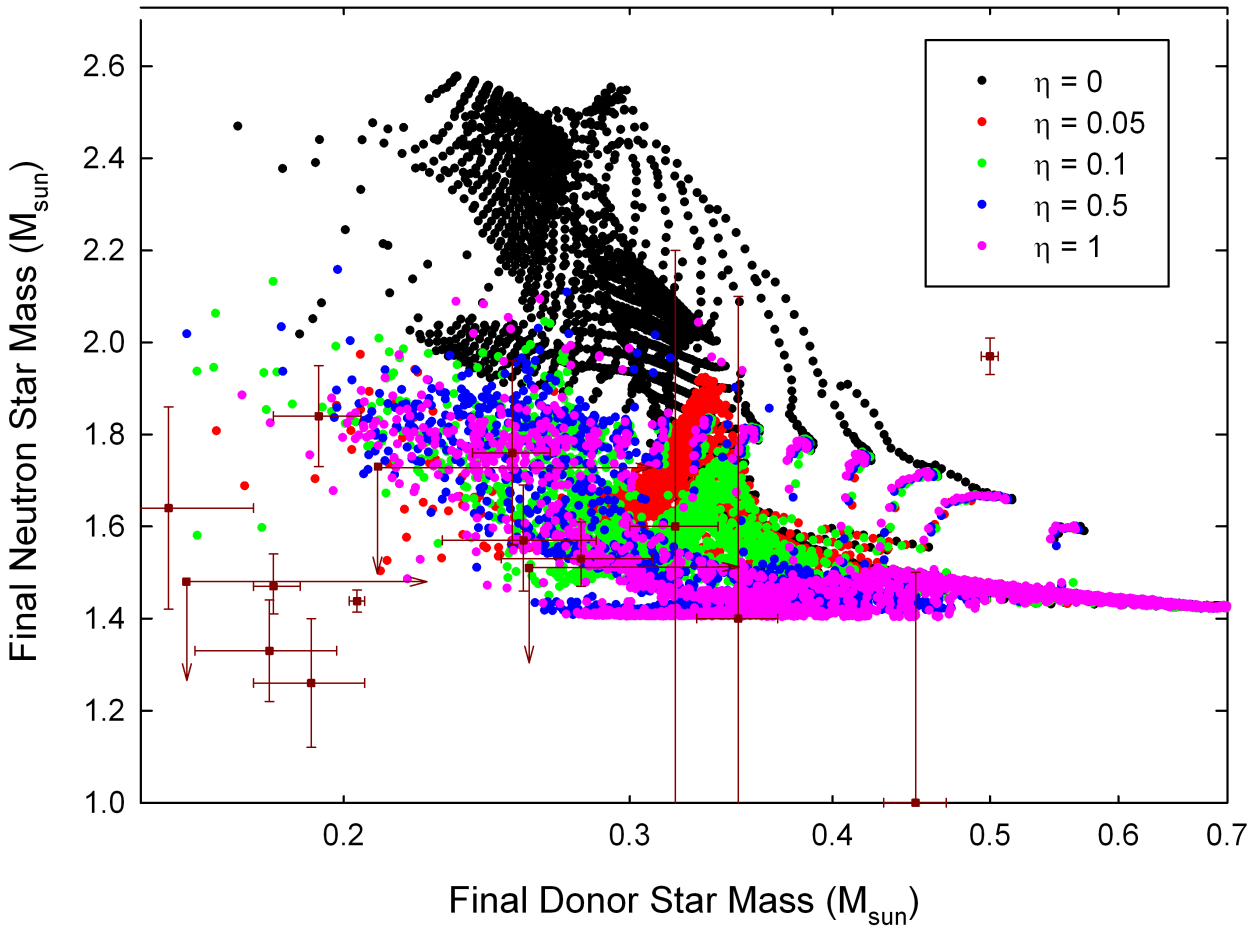

Figure 4.3: End points of the evolutionary grids with the effects of irradiation comparing $\eta = 0.0$ (no irradiation), 0.05, 0.10, 0.50, and 1.0 (full irradiation). This is a graph of the final neutron star mass as a function of the final donor star mass.

final neutron star mass. If without irradiation the results showed neutron stars as massive as $2.6\,M_\odot$, then with the effects of irradiation, only a few neutron stars accrete sufficient mass to grow larger than $2.0\,M_\odot$. Looking at the different efficiency factors, one sees different results for small efficiencies (5% and 10%) and large efficiencies (50% and 100%). Indeed, if all cases are similar for large final donor star masses ($\gtrsim 0.4\,M_\odot$), it is different for smaller final donor stars. In fact, it is easily seen that for the range $M_{2,f} \simeq 0.3 - 0.4\,M_\odot$, values of $\eta = 0.50$ and $\eta = 1.0$ produced similar results, but that $\eta = 0.1$ produces heavier final neutron stars, and that, $\eta = 0.05$ produces even slightly heavier final neutron star masses. However, as stated in the previous paragraph, there are reasons to believe that large efficiency factors are not physical.

The distinction between irradiated and non-irradiated results is more significant for $M_{2,f} \lesssim 0.3\,M_\odot$ where much smaller neutron stars were produced with irradiation. This has the advantage of reproducing the observed properties of many more binary millisecond pulsars that were not explained without irradiation (unless β_{max} was arbitrarily set to a very small value as discussed in Section 2.4.4).

Interestingly, these results are observed even with an efficiency factor as low as 5%, showing that the donor star does not need to be irradiated by a large fraction of the total irradiation flux in order to bloat up and produce irradiation cycles. Furthermore, one can test smaller efficiency factors. Computing another evolutionary grid would require some significant time, but one can simply check one particular track. For example, if one starts with $M_{1,i} = 1.4\,M_\odot$, $M_{2,i} = 1.45\,M_\odot$, and $P_{orb,i} \cong 25.12$ hours, one will obtain without irradiation $M_{1,f} \cong 2.28\,M_\odot$, $M_{2,f} \cong 0.26\,M_\odot$, and $P_{orb,f} \cong 477$ hours, whereas $\eta = 0.05$ produces $M_{1,f} \cong 1.55\,M_\odot$, $M_{2,f} \cong 0.25\,M_\odot$, and $P_{orb,f} \cong 367$ hours. Thus, $\eta = 0.05$ has a strong effect on $M_{1,f}$, an important effect on $P_{orb,f}$, but not so much on $M_{2,f}$. Now, computing the evolution of the same system but with $\eta = 0.01$ produces $M_{1,f} \cong 1.86\,M_\odot$, $M_{2,f} \cong 0.26\,M_\odot$, and $P_{orb,f} \cong 462$ hours. Thus, even an efficiency factor of 1% leads to a significantly smaller final neutron star mass. Again, $M_{2,f}$ is unchanged, but $P_{orb,f}$ is closer to the non-irradiated case.

It is interesting to note that Benvenuto et al. [15] considered irradiation with efficiency factors as low as $\eta = 0.05$ and $\eta = 0.01$ in order to reproduce the observed properties of a very peculiar binary millisecond pulsar, PSR J1719-1438, that contains a Jupiter-like mass companion in 2.2 hour orbit. The study of such a system would require us to look at CV-like evolution though.

Therefore, irradiation clearly seems to reproduce the smaller neutron star masses that one seeks for, but there are still a few important systems that remain unexplained. Indeed, there are not many theoretical simulations close to PSR J1909-3744 with $M_{NS} = 1.438 \pm 0.024\,M_\odot$ and $M_{WD} = 0.2038 \pm 0.0022\,M_\odot$. Also, PSR J1614-2230 with $M_{NS} = 1.97 \pm 0.04\,M_\odot$ and $M_{WD} = 0.500 \pm 0.006$ is far from being explained. The solution to this issue may reside in changing the natal mass of the neutron star as will be discussed in the following section.

So, irradiation clearly reduces the amount of mass that neutron stars can accrete, but

there might be an undesirable consequence of this. Ritter [137] claims that the amount of mass accreted by the neutron star would be insufficient to spin it up to a spin period of a few milliseconds as should be the case for binary millisecond pulsars. Fortunately, Tauris et al. [159] find that the accreted mass (ΔM), the mass of the neutron star (M_1), and the spin period of the pulsar (P_{ms}) are related by

$$\Delta M = 0.22\, M_\odot \frac{(M_1/M_\odot)^{1/3}}{P_{ms}^{4/3}}\,. \tag{4.1}$$

Thus, if a $1.4\, M_\odot$ neutron star accretes a little as $0.1\, M_\odot$ of matter, then it can still spin up to a period of $P \simeq 2\,$ms; most of the binary millisecond pulsars have periods above 2 ms (e.g., [159]). So, the small amounts of mass accreted should be sufficient to spin up neutron stars to produce millisecond pulsars. Computing the exact spin period and spin period derivative with irradiation, and comparing this with observations (as is done by Tauris et al. [159] without irradiation), would be interesting avenue of future investigation.

4.2.2 Changing the Natal Mass of the Neutron Star

In order to reproduce the properties of PSR J1614-2230 and PSR J1909-3744, one may have to invoke either smaller or larger natal masses for the neutron star. As discussed in Section 2.4, there is some uncertainty in the value that $M_{1,i}$ should take. For this reason, it may be possible that $M_{1,i} \simeq 1.2\, M_\odot$, which would be promising for J1614-2230, or it may be that $M_{1,i} \simeq 1.6\, M_\odot$, which would be promising for J1909-3744. So, let us look at the end points of binary evolutionary grids when the natal masses of the neutron star are either $1.2\, M_\odot$ or $1.6\, M_\odot$.

Figure 4.4 shows the end points for $M_{1,i} = 1.2\, M_\odot$. Comparing panel a) with Figure 4.2 shows that lowering the natal mass of the neutron star produces smaller final orbital periods, but the results still match the orbital period of most of the binary millisecond pulsars and the period-mass relation is still satisfied. Looking at panel b), one sees that the properties of most of the low-mass neutron stars are now very well reproduced with irradiation. Most importantly, there are many numerical results that would fit the properties of PSR J1909-3744.

Figure 4.5 shows the (perhaps) less likely situation where the neutron star would be born relatively massive ($1.6\, M_\odot$). One can claim that this is a less likely situation from neutron star birth mass studies. Furthermore, we see here that it is indeed a less likely situation looking at panel b) of Figure 4.5, since neutron stars would accrete mass up to almost $3\, M_\odot$ in some cases (without irradiation). However, this is the only way of getting closer to $M_{NS} = 1.97 \pm 0.04\, M_\odot$ for PSR J1614-2230. Indeed, there are a few tracks (without irradiation) that ended their evolution with properties similar to this system. One can see that there are two numerical results with irradiation (green dots) that show $M_{1,f} \simeq 1.87\, M_\odot$

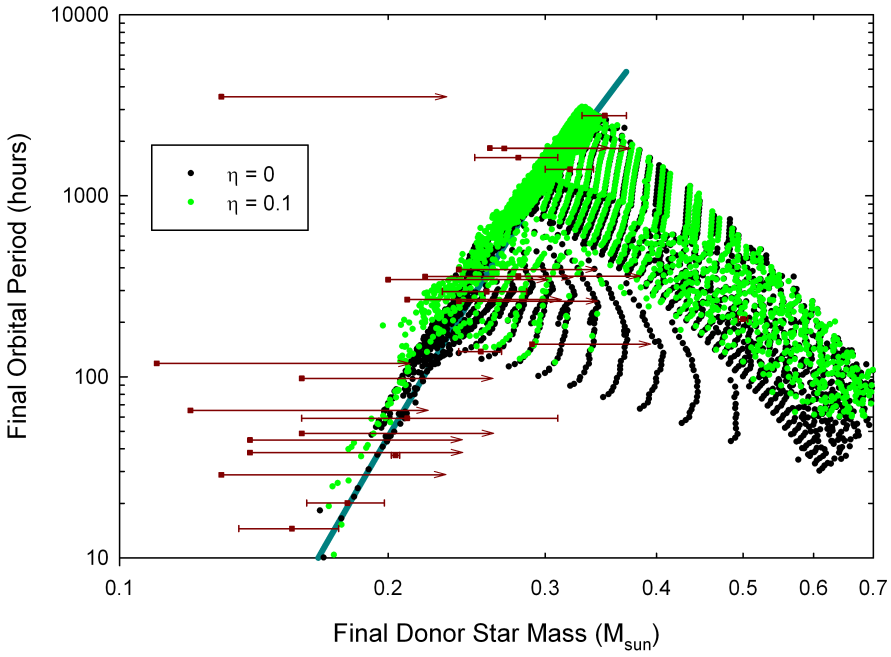

a)

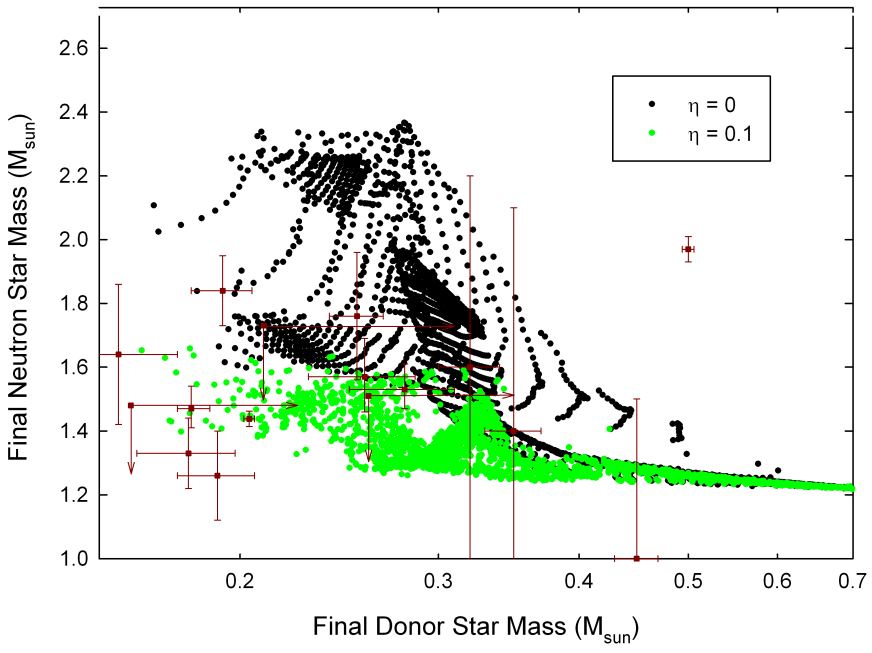

b)

Figure 4.4: End points of evolutionary grids where $M_{1,i} = 1.2\,M_{\odot}$. The black dots are computed without irradiation ($\eta = 0$) and the green dots show the effects of irradiation for $\eta = 0.1$.

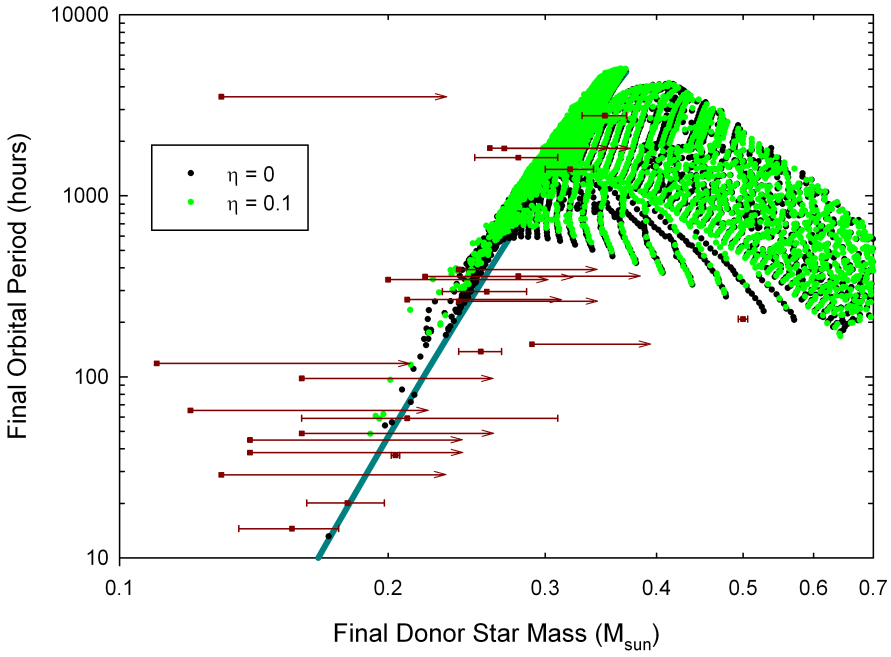

a)

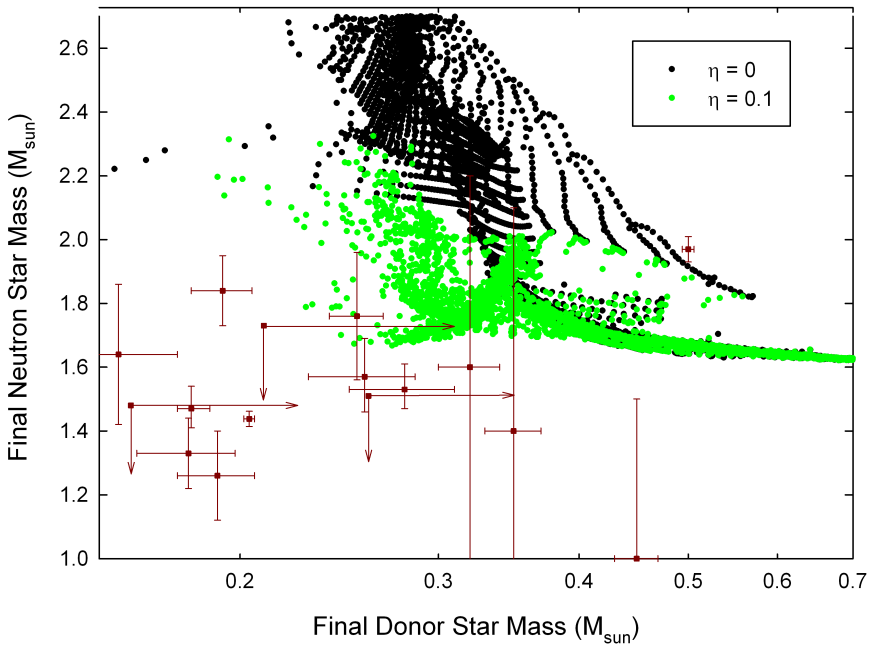

b)

Figure 4.5: End points of evolutionary grids where $M_{1,i} = 1.6\,M_{\odot}$. The black dots are computed without irradiation ($\eta = 0$) and the green dots show the effects of irradiation for $\eta = 0.1$.

(which is not too far below M_{NS} for PSR J1614-2230) and that would fit the final donor star mass. So, it could be that irradiation still occurs in the generation of such a system. However, an even slightly larger natal mass for the neutron star would be required in that case. Unfortunately, all those numerical results seem to have a larger orbital period than PSR J1614-2230 by about 100 hours. Thus, although one can get closer to reproducing this system with $M_{1,i} = 1.6\,M_\odot$, it remains a challenge to find the initial conditions that could reproduce it.

Note that Lin et al. [90] found that to reproduce the observed properties of PSR J1614-2230, one would need $M_{1,i} = 1.6 \pm 0.1\,M_\odot$. However, recall that this did not include the effects of the binding energy of the neutron star. Also, Tauris et al. [158] found for the same system that the natal mass of the neutron star should be $1.70 \pm 0.15\,M_\odot$, i.e. even more massive. Thus, it is possible that PSR J1614-2230 is a very special case which does require a very massive initial neutron star.

Chapter 5

Conclusions

The goal of this thesis was to study the evolution of low- and intermediate-mass X-ray binary systems. More particularly, the goal was to include the physics of self-induced X-ray irradiation in order to determine the overall effects of irradiation on the evolution of X-ray binaries. Thus a model consisting of Monte-Carlo simulations to determine the penetration depth of X-rays in the donor stars was created to include X-ray irradiation into the `MESA` stellar evolution code. Furthermore, the effects of the binding energy of neutron stars was included in the evolution. Then, the evolution of 4,200 binary models was computed from a set of initial conditions in the $P_{orb} - M_2$ parameter space. These calculations were repeated with different maximum mass-transfer fractions (β_{max}), different irradiation efficiency factors (η), and different natal masses for the neutron stars ($M_{1,i}$).

We showed that standard X-ray binary evolution ($\beta_{max} = 1$, $\eta = 0$, $M_{1,i} = 1.4\,M_\odot$) could reasonably reproduce some of the properties of many binary millisecond pulsars, but often, the neutron stars accreted too much mass compared to the observations. One of the possible solutions to this discrepancy is to reduce β_{max} arbitrarily, but there are few good physical reasons to do this. Another solution is to include the effects of irradiation.

We found that self-induced X-ray irradiation can produce irradiation cycles where the X-ray binaries alternated between transient high mass-transfer phases and quiescent phases. Thus, because the mass-transfer rates were super-Eddington most of the time, the neutron stars accreted barely any mass, hence better matching the smaller observed neutron star mass values. We also found that this effect could be significant with an efficiency factor as low as 5%.

The results presented in this thesis allows one to answer Ritter's [137] question: Is irradiation important for the secular evolution of low-mass X-ray binaries? It seems that irradiation does modify the evolutionary paths of LMXBs and IMXBs that evolve to become binary millisecond pulsars. In fact, irradiation significantly lowers the final mass of the neutron stars, which is a desirable effect given that one had to invoke non-conservative mass transfer in previous studies. Also, irradiation modifies the final orbital period of X-ray

binaries, but only slightly for $\eta = 0.1$ and $\eta = 0.05$. The changes are more important for $\eta = 0.5$ and $\eta = 1$, which suggest that irradiation with such high efficiencies does not occur.

Note that different natal masses for the neutron stars were also tested in this thesis in order to reproduce the observed properties of particular binary millisecond pulsars. This showed that $1.2\,M_{\odot}$ could be a suitable initial mass for the neutron star. Also, it showed that $M_{1,i} \geq 1.6\,M_{\odot}$ would be needed in special cases since the neutron star mass of some observed systems cannot not be explained with $M_{1,i} < 1.6\,M_{\odot}$.

5.1 Future Work

In the future, it would be interesting to focus on finding the initial conditions that can lead to particular observed systems such as PSR J1909-3744 and PSR J1614-2230. This would require one to zero in particular regions of the $P_{orb} - M_2$ parameter space and test various combinations of $M_{1,i}$, η, and β_{max}.

Also, as mentioned in Section 4.2.1, it would be interesting to investigate the spin-up of neutron stars as they become millisecond pulsars. Since there are good observations of neutron star spin period and of their spin period derivative, investigating this avenue could help improving the theoretical model of X-ray binary systems.

In order to improve the model for irradiation presented in this thesis, one would need to determine what fraction of the X-rays are intercepted by the accretion disk of the neutron star through a proper analysis of accretion disks. Also, three-dimensional computations in the donor star's interior would improve the energy deposition model.

Finally, analyzing the effects of self-induced X-ray irradiation in CV-like X-ray binary systems would be interesting to investigate in the future. However, this might be challenging given the numerical difficulties that we mentioned in Section 3.3.2.

Appendix A

Geometry of X-ray Binary Systems

A.1 Proof of the Formula for the Geometrical Factor $h(\theta)$ in the equation for the Irradiation Flux

Looking at Figure A.1, one can see that

$$\cos\theta_{max} = \frac{R_2}{a}\,, \tag{A.1}$$

where θ_{max} is the limb angle, that is for $\theta \geq \theta_{max}$, the star would not intercept any X-ray photon. Let us define

$$f_2 \equiv \frac{R_2}{a}\,. \tag{A.2}$$

Thus,

$$\theta_{max} = \arctan f_2\,. \tag{A.3}$$

According to Büning & Ritter [22], the geometrical factor that is of interest here, $h(\theta)$, is equal to $\cos\beta$, where the angle β is define in Figure A.1. Figure A.1 shows that $h(\theta) = \cos\beta$, since one only wants the component of the flux F_{irr} ($F(\theta)$ in Figure A.1) that is perpendicular to the surface of the star. Simple geometry tells us that $\gamma = \pi - \beta$ and $\delta = \beta - \theta$, so the law of sines $\frac{\sin\gamma}{a} = \frac{\sin\delta}{R_2}$ becomes

$$R_2 \sin(\pi - \beta) = a \sin(\beta - \theta) = a\,(\sin\beta\cos\theta - \cos\beta\sin\theta)\ , \tag{A.4}$$

so

$$f_2 \equiv \frac{R_2}{a} = \cos\theta - \cot\beta\sin\theta\,, \tag{A.5}$$

which can be solved for β. Thus,

$$\beta = \arctan\left(\frac{\sin\theta}{\cos\theta - f_2}\right)\ , \tag{A.6}$$

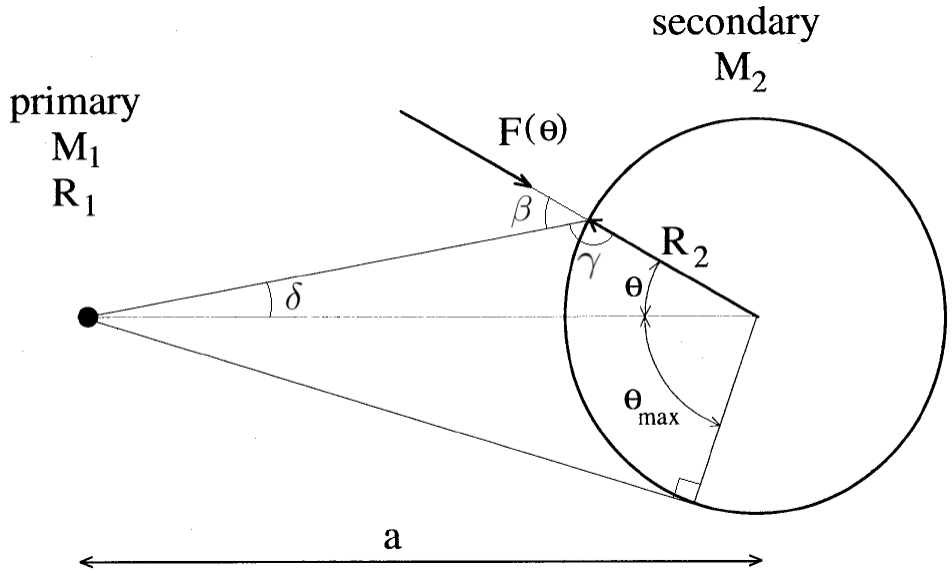

Figure A.1: Geometry of an X-ray binary system (figure taken from King et al. [76] with additional angles following Büning & Ritter [22]).

and consequently,

$$\cos\beta = \left[\left(\frac{\sin\theta}{\cos\theta - f_2}\right)^2 + 1\right]^{-\frac{1}{2}} , \tag{A.7}$$

which can be simplified to yield

$$\cos\beta = \left[\frac{\sin^2\beta + \cos^2\beta - 2f_2\cos\beta + f_2^2}{(\cos\beta - f_2)^2}\right]^{-\frac{1}{2}} ;$$

$$\therefore \cos\beta = \frac{\cos\theta - f_2}{(1 - 2f_2\cos\theta + f_2^2)^{\frac{1}{2}}} . \tag{A.8}$$

A.2 Proof of the Relation between the Distance Traveled in Shell k by an X-ray Photon, Δd_k, and the Shell Thickness, Δr_k.

According to Figure A.2, simple geometry tells us that

$$\begin{cases} \alpha_{k+1} + \beta_{k+1} = \pi \\ \alpha_{k+1} + \gamma_k + \omega_k = \pi \end{cases} , \tag{A.9}$$

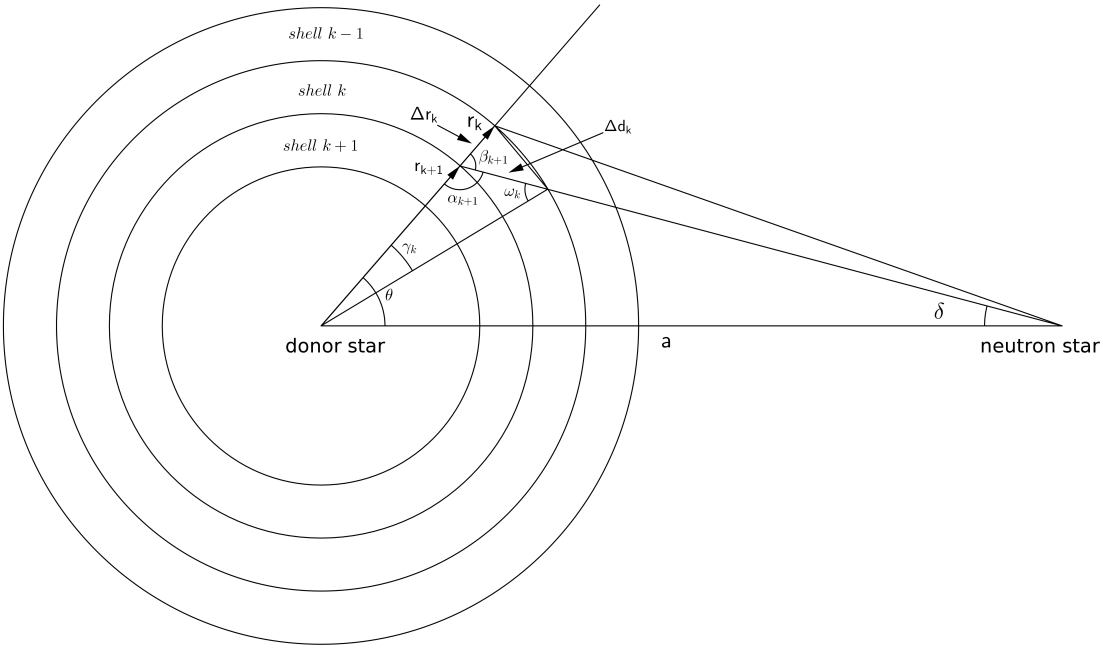

Figure A.2: Schematic diagram showing the angles used in the proof in this appendix.

so $\alpha_{k+1} = \pi - \beta_{k+1}$ and $\omega_k = \beta_{k+1} - \gamma_k$. Then, the law of sines,

$$\frac{\sin \alpha_{k+1}}{r_k} = \frac{\sin \gamma_k}{\Delta d_k} = \frac{\sin \omega_k}{r_{k+1}}\,, \tag{A.10}$$

becomes

$$\frac{\sin\left(\pi - \beta_{k+1}\right)}{r_k} = \frac{\sin \gamma_k}{\Delta d_k} = \frac{\sin\left(\beta_{k+1} - \gamma_k\right)}{r_{k+1}}\,, \tag{A.11}$$

or

$$\Delta d_k \sin \beta_{k+1} = r_k \sin \gamma_k \tag{A.12}$$

$$r_{k+1} \sin \beta_{k+1} = r_k \sin\left(\beta_{k+1} - \gamma_k\right) \tag{A.13}$$

$$r_{k+1} \sin \gamma_k = \Delta d_k \sin\left(\beta_{k+1} - \gamma_k\right)\,. \tag{A.14}$$

Then, starting from Equation A.13, one can solve for γ_k to find

$$\gamma_k = \beta_{k+1} - \arcsin\left(\frac{r_{k+1}}{r_k} \sin \beta_{k+1}\right) \tag{A.15}$$

$$\therefore \sin \gamma_k = \sin\left[\beta_{k+1} - \arcsin\left(\frac{r_{k+1}}{r_k} \sin \beta_{k+1}\right)\right]$$

$$\therefore \sin\gamma_k = \sin\beta_{k+1}\cos\left[\arcsin\left(\frac{r_{k+1}}{r_k}\sin\beta_{k+1}\right)\right] - \left(\frac{r_{k+1}}{r_k}\sin\beta_{k+1}\right)\cos\beta_{k+1}$$

$$\therefore \sin\gamma_k = \left(\sqrt{1-\frac{r_{k+1}^2}{r_k^2}\sin^2\beta_{k+1}} - \frac{r_{k+1}}{r_k}\cos\beta_{k+1}\right)\sin\beta_{k+1}$$

$$\therefore \sin\gamma_k = \frac{\sin\beta_{k+1}}{r_k}\left(\sqrt{r_k^2 - r_{k+1}^2\sin^2\beta_{k+1}} - r_{k+1}\cos\beta_{k+1}\right). \tag{A.16}$$

Using Equation A.12, one gets

$$\Delta d_k = \sqrt{r_k^2 - r_{k+1}^2\sin^2\beta_{k+1}} - r_{k+1}\cos\beta_{k+1}\,. \tag{A.17}$$

Now, looking at Figure A.2 again, one can apply the law of sines to another triangle, i.e.

$$\frac{\sin\alpha_{k+1}}{a} = \frac{\sin\delta}{r_{k+1}}\,. \tag{A.18}$$

So recalling that $\alpha_{k+1} = \pi - \beta_{k+1}$, one obtains

$$\sin\beta_{k+1} = \frac{a}{r_{k+1}}\sin\delta\,. \tag{A.19}$$

Thus, Equation A.17 becomes

$$\Delta d_k(\delta) = \sqrt{r_k^2 - r_{k+1}^2\frac{a^2}{r_{k+1}^2}\sin^2\delta} - r_{k+1}\sqrt{1-\frac{a^2}{r_{k+1}^2}\sin^2\delta}\,; \tag{A.20}$$

$$\therefore \Delta d_k(\delta) = \sqrt{r_k^2 - a^2\sin^2\delta} - \sqrt{r_{k+1}^2 - a^2\sin^2\delta}. \tag{A.21}$$

Bibliography

[1] Akmal, A.; Pandharipande, V. R.; and Ravenhall, D. G. *Equation of State of Nucleon Matter and Neutron Star Structure*, Physical Review C, 58:1804-1828 (1998)

[2] Alécian, E. and Morsink, S. M. *The Effect of Neutron Star Gravitational Binding Energy on Gravitational Radiation-Driven Mass-Transfer Binaries*, ApJ, 614:914-921 (2004)

[3] Andronov, N.; Pinsonneault, M.; and Sills, A. *Cataclysmic Variables: An Empirical Angular Momentum Loss Prescription From Open Cluster Data*, ApJ, 582:358-368 (2003)

[4] Antoniadis, J.; van Kerkwijk, M. H.; Koester, D.; Freire, P. C. C.; Wex, N.; Tauris, T. M.; Kramer, M.; and Bassa, C. G. *The Relativistic Pulsar-White Dwarf Binary PSR J1738+0333 - I. Mass Determination and Evolutionary History*, MNRAS, 423:3316-3327 (2012)

[5] Arons, J. *Self-Excited Flow in Binary X-ray Sources*, ApJ, 184:539-550 (1973)

[6] Arzoumanian, Z.; Thorsett, S. E.; and Taylor, J. H. *The Masses of two Binary Pulsar Systems*, in Fruchter, A. S.; Tavani, M.; and Backer, D. C. (eds) *Millisecond Pulsars: A Decade of Surprise*, Astronomical Society of the Pacific, San Francisco (1995)

[7] Bagchi, M. *The Role of Binding Energies of Neutron Stars on the Accretion Driven Evolution*, MNRAS, 413:L47-L50 (2011)

[8] Bagchi, M. and Ray, A. *Radio Pulsars Binaries in Globular Clusters: Their Orbital Eccentricities and Stellar Interactions*, ApJ, 701:1161-1174 (2009)

[9] Bailes, M.; Harrison, P. A.; Lorimer, D. R.; Johnston, S.; Lyne, A. G.; Manchester, R. N.; D'Amico, N.; Nicastro, L.; Tauris, T. M.; and Robinson, C. *Discovery of Three Binary Millisecond Pulsars*, ApJ, 425:L41-L44 (1994)

[10] Basko, M. M. and Sunyaev, R. A. *Interaction of the X-Ray Source Radiation with the Atmosphere of the Normal Star in Close Binary Systems*, Astrophysics and Space Science, 23:117-158 (1973)

[11] Bassa, C. G.; van Kerkwijk, M. H.; Koester, D.; and Verbunt, F. *The Masses of PSR J1911-5958A and its White Dwarf Companion*, Astronomy and Astrophysics, 456:295-304 (2006)

[12] Bath, G. T. *Dynamical Instabilities and Mass Exchange in Binary Systems*, MNRAS, 171:311-328 (1975)

[13] Becker, C. M.; Tavani, M.; and Rappaport, S. A. *A Study of Self-Excited Evolution of Low Mass X-ray Binaries*, in Fruchter, A. S.; Tavani, M.; and Backer, D. C. (eds) *Millisecond Pulsars: A Decade of Surprise*, Astronomical Society of the Pacific, San Francisco (1995)

[14] Belczynski, K.; Kalogera, V.; Rasio, F. A.; Taam, R. E.; Zezas, A.; Bulik, T.; Maccarone, T. J.; and Ivanova, N. *Compact Object Modeling with the StarTrack Population Synthesis Code*, ApJ S, 174:223-260 (2008)

[15] Benvenuto, O. G.; De Vito, M. A.; Horvath, J. E. *Evolutionary Trajectories of Ultracompact "Black Widow" Pulsars with Very Low Mass Companions*, ApJ, 753:L33-L36 (2012)

[16] Bhat, N. D. R.; Bailes, M.; and Verbiest J. P. W. *Gravitational-Radiation Losses from the Pulsar–White-Dwarf Binary PSR J1141–6545*, Phys. Rev. D 77, 124017 (2008)

[17] Bhattacharya, D. and van den Heuvel, E. P. J. *Formation and Evolution of Binary and Millisecond Radio Pulsars*, Physics Reports, 203:1-124 (1991)

[18] Bogdanov, S.; Archibald, A. M.; Hessels, J. W. T.; Kaspi, V. M.; Lorimer, D.; McLaughlin, M. A.; Ransom, S. M.; Stairs, I. H. *A Chandra X-Ray Observation of the Binary Millisecond Pulsar PSR J1023+0038*, ApJ, 724:97-106 (2011)

[19] Bogdanov, S.; Grindlay, J. E.; van den Berg, M. *An X-Ray Variable Millisecond Pulsar in the Globular Cluster 47 Tucanae: Closing the Link to Low-Mass X-Ray Binaries*, ApJ, 630:1029-1036 (2005)

[20] Böhm-Vitense, E. *Über die Wasserstoffkonvektionszone in Sternen verschiedener Effektivtemperaturen und Leuchtkräfte. Mit 5 Textabbildungen*, Zeitschrift für Astrophysik, 46:108-143 (1958)

[21] Brett, J. M. and Smith, R. C. *A Model Atmosphere Investigation of the Effect of Irradiation on the Secondary Star in a Dwarf Nova*, MNRAS, 264:641-653 (1993)

[22] Büning, A. and Ritter, H. *Long-Term Evolution of Compact Binaries with Irradiation Feedback*, Astronomy and Astrophysics, 423:281-299 (2004)

[23] Büning, A. and Ritter, H. *Irradiation-Driven Mass Transfer Cycles in Compact Binaries*, in Hameury, J.-M. and Lasota, J.-P. (eds) *The Astrophysics of Cataclysmic Variables and Related Objects*, Astronomical Society of the Pacific, San Francisco (2005)

[24] Callanan, P. J.; Garnavich, P. M.; and Koester, D. *The Mass of the Neutron Star in the Binary Millisecond Pulsar PSR J1012+5307*, MNRAS, 298:207-211 (1998)

[25] Camilo, F.; Nice, D. J.; and Taylor, J. H. *A Search for Millisecond Pulsars at Galactic Latitudes -50 degrees < B < -20 degrees*, ApJ, 461:812-819 (1996)

[26] Camilo, F.; Lorimer, D. R.; Freire, P.; Lyne, A. G.; and Manchester, R. N. *Observations of 20 Millisecond Pulsars in 47 Tucanae at 20 Centimeters*, ApJ, 535:975-990 (2000)

[27] Camilo, F.; Lyne, A. G.; Manchester, R. N.; Bell, J. F.; Stairs, I. H.; D'Amico, N.; Kaspi, V. M.; Possenti, A.; Crawford, F.; and McKay, N. P. F. *Discovery of Five Binary Radio Pulsars*, ApJ, 548:L187-L191 (2001)

[28] Carroll, S. M. *Spacetime and Geometry, An Introduction to General Relativity*, Addison-Wesley, San Francisco US (2004)

[29] Christian, D. J. and Swank, J. H. *The Survey of Low-Mass X-ray Binaries with the Einstein Observatory Solid-State Spectrometer and Monitor Proportional Counter*, ApJ S, 109:177-224 (1997)

[30] Corongiu, A.; Burgay, M.; Possenti, A.; Camilo, F.; D'Amico, N.; Lyne, A. G.; Manchester, R. N.; Sarkissian, J. M.; Bailes, M.; Johnston, S.; Kramer, M.; and van Straten, W. *A Shapiro Delay Detection in the Binary System Hosting the Millisecond Pulsar PSR J1910–5959A*, ApJ, 760:100-108 (2012)

[31] Cox, J. and Giuli, R. *Principles of Stellar Structure*, Gordon and Breach, New York NY (1968)

[32] Cui, W. *Evidence for "Propeller" Effects in X-Ray Pulsars GX 1+4 and GRO J1744-28*, ApJ, 482:L163-L166 (1997)

[33] D'Amico, N.; Lyne, A. G.; Manchester, R. N.; Possenti, A.; and Camilo, F. *Discovery of Short-Period Binary Millisecond Pulsars in Four Globular Clusters*, ApJ, 548:L171-L174 (2001)

[34] D'Antona, F. and Ergma, E. *Evolution of Binaries with a Low Mass Component Immerged in a Radiation Field I. Effect of Irradiation by a Millisecond Pulsar Companion*, Astronomy and Astrophysics, 269:219-230 (1993)

[35] Demorest, P. B.; Pennucci, T.; Ransom, S. M.; Roberts, M. S. E.; and Hessels, J. W. T. *A Two-Solar-Mass Neutron Star Measured using Shapiro Delay*, Nature, 467:1081-1083 (2010)

[36] De Vito, M. A. and Benvenuto, O. G. *The Evolution of Low Mass, Close Binary Systems with a Neutron Star Component: a Detailed Grid*, MNRAS, 421:2206-2222 (2012)

[37] Dubeau, E., *Radio Ejection and the Orbital Period Gap in the Distribution of Binary Millisecond Pulsars*, M.Sc. Thesis, Bishop's University (2009)

[38] Eddington, A. S. *The Internal Constitution of the Stars*, Cambridge University Press, Cambridge, UK (1926)

[39] Eggleton, P. *Approximation To The Radii of Roche Lobes*, ApJ, 268: 368-369 (1983)

[40] Faulkner, J. *Ultrashort-Period Binaries, Gravitational Radiation, and Mass Transfer. I. The Standard Model, with Applications to WZ Sagittae and Z Camelopardalis*, ApJ, 170:L99-L104 (1971)

[41] Ferdman, R. D.; Stairs, I. H.; Kramer, M.; McLaughlin, M. A.; Lorimer, D. R.; Nice, D. J.; Manchester, R. N.; Hobbs, G.; Lyne, A. G.; Camilo, F.; Possenti, A.; Demorest, P. B.; Cognard, I.; Desvignes, G.; Theureau, G.; Faulkner, A.; and Backer, D. C. *A Precise Mass Measurement of the Intermediate-Mass Binary Pulsar PSR J1802 - 2124*, ApJ, 711:764-771 (2010)

[42] Frank, J.; King, A. R.; and Lasota, J.-P. *Low-Mass X-ray Binary Evolution and the Origin of Millisecond Pulsars*, ApJ, 385:L45-L48 (1992)

[43] Frank, J.; King, A. R.; and Raine, D. J. *Accretion Power in Astrophysics*, Cambridge University Press, Cambridge (2002)

[44] Freire, P. C. C.; Bassa, C. G.; Wex, N.; Stairs, I. H.; Champion, D. J.; Ransom, S. M.; Lazarus, P.; Kaspi, V. M.; Hessels, J. W. T.; Kramer, M.; Cordes, J. M.; Verbiest, J. P. W.; Podsiadlowski, P.; Nice, D. J.; Deneva, J. S.; Lorimer, D. R.; Stappers, B. W.; McLaughlin, M. A.; and Camilo, F. *On the Nature and Evolution of the Unique Binary Pulsar J1903+0327*, MNRAS, 412:2763-2780 (2011)

[45] Freire, P. C.; Camilo, F.; Kramer, M.; Lorimer, D. R.; Lyne, A. G.; Manchester, R. N.; and D'Amico, N. *Further Results from the Timing of the Millisecond Pulsars in 47 Tucanae*, MNRAS, 340:1359-1374 (2003)

[46] Freire, P. C. C.; Ransom, S. M.; Bégin, S.; Stairs, I. H.; Hessels, J. W. T.; Frey, L. H.; and Camilo, F. *Eight New Millisecond Pulsars in NGC 6440 and NGC 6441*, ApJ, 675:670-682 (2008)

[47] Freire, P. C. C.; Ransom, S. M.; and Gupta, Y. *Timing the Eccentric Binary Millisecond Pulsar in NGC 1851*, ApJ, 662:1177-1182 (2007)

[48] Freire, P. C. C.; Wolszczan, A.; van den Berg, M.; and Hessels, J. W. T. *A Massive Neutron Star in the Globular Cluster M5*, ApJ, 679:1433-1442 (2008)

[49] Glendenning, N. K. *Special and General Relativity With Applications to White Dwarfs, Neutron Stars and Black Holes*, Springer, US (2007)

[50] Goliasch, J., *Detailed Population Synthesis Studies of Cataclysmic Variables*, M.Sc. Thesis, Bishop's University (2009)

[51] Gontikakis, C. and Hameury, J.-M. *Constraints on the Illumination Model for Soft X-ray Transients*, Astronomy and Astrophysics, 271:118-124 (1993)

[52] Gonzalez, M. E.; Stairs, I. H.; Ferdman, R. D.; Freire, P. C. C.; Nice, D. J.; Demorest, P. B.; Ransom, S. M.; Kramer, M.; Camilo, F.; Hobbs, G.; Manchester, R. N.; and Lyne, A. G. *High-precision Timing of Five Millisecond Pulsars: Space Velocities, Binary Evolution, and Equivalence Principles*, ApJ, 743:102-114 (2011)

[53] Guillot, S.; Servillat, M.; Webb, N. A.; and Rutledge, R. E. *Measurement of the Radius of Neutron Stars with High S/N Quiescent Low-Mass X-ray Binaries in Globular Cluster*, arxiv:1302.0023 (2013)

[54] Hameury, J.-M.; King, A. R.; and Lasota, J.-P. *A Model for Soft X-ray Transients*, Astronomy and Astrophysics, 162:71-79 (1986)

[55] Hameury, J.-H.; King, A. R.; Lasota, J.-P.; and Raison, F. *Structure and Evolution of X-ray Heated Compact Binaries*, Astronomy and Astrophysics, 277:81-92 (1993)

[56] Hameury, J.-M.; King, A. R.; Lasota, J.-P. *LMXB Evolution: Illumination Effect*, in Fruchter, A. S.; Tavani, M.; and Backer, D. C. (eds) *Millisecond Pulsars: A Decade of Surprise*, Astronomical Society of the Pacific, San Francisco (1995)

[57] Hameury, J.-M. and Ritter, H. *Illumination in Binaries*, Astronomy and Astrophysics Supplement Series, 123:273-277 (1997)

[58] Harpaz, A. and Rappaport, S. *Evolution of Compact Binary Systems with X-ray Heating*, ApJ, 383:739-744 (1991)

[59] Harpaz, A. and Rappaport, S. *Episodic Mass Transfer in Binaries with X-ray Heating*, ApJ, 434:283-287 (1994)

[60] Harpaz, A. and Rappaport, S. *Heating of a Rotating Star*, Astronomy and Astrophysics, 294:L49-L52 (1995)

[61] Herwig, F. *The Evolution of AGB Stars with Convective Overshoot*, Astronomy and Astrophysics, 360:952-968 (2000)

[62] Howell, S.; Nelson, L.; and Rappaport, S. *An Exploration of The Paradigm For The 2-3 Hour Period Gap In Cataclysmic Variables*, ApJ, 550: 897-918 (2001)

[63] Hurley, J. R.; Tout, C. A.; Pols, O. R. *Evolution of Binary Stars and the Effect of Tides on Binary Populations*, MNRAS, 329:897-928 (2002)

[64] Hussain, G. A. J. *Magnetic Braking in Convective Stars*, in Schmidtobreick, L.; Schreiber, M. R.; and Tappert, C. (eds) *Evolution of Compact Binaries*, Astronomical Society of the Pacific, San Francisco (2011)

[65] Iben, I., Jr.; Tutukov, A. V.; and Yungelson, L. R. *A Model of the Galactic X-Ray Binary Population. II. Low-Mass X-Ray Binaries in the Galactic Disk*, ApJ S, 100:233-268 (1995)

[66] Illarionov, A. F. and Sunyaev, R. A. *Why the Number of Galactic X-ray Stars Is so Small?*, Astronomy and Astrophysics, 39:185-195 (1975)

[67] Irwin, J. A. and Bregman, J. N. *Using the Bulge of M31 as a Template for the Integrated X-ray Emission from Low-Mass X-ray Binaries*, ApJ, 527:125-131 (1999)

[68] Jacoby, B. A.; Hotan, A.; Bailes, M.; Ord, S.; and Kulkarni, S. R. *The Mass of a Millisecond Pulsar*, ApJ, 629:L113-L116 (2005)

[69] Jacoby, B. A.; Bailes, M.; Ord, S. M.; Knight, H. S.; and Hotan, A. W. *Discovery of Five Recycled Pulsars in a High Galactic Latitude Survey*, ApJ, 656:408-413 (2007)

[70] Janssen, G. H.; Stappers, B. W.; Bassa, C. G.; Cognard, I.; Kramer, M.; and Theureau, G. *Long-term timing of four millisecond pulsars*, Astronomy and Astrophysics, 514, A74 (2010)

[71] Joss, P. C. and Rappaport, S. A. *Neutron Stars in Interacting Binary Systems*, Annual review of astronomy and astrophysics, 22:537-592 (1984)

[72] Kaplan, D. L.; Bhalerao, V. B.; van Kerkwijk, M. H.; Koester, D.; Kulkarni, S. R.; and Stovall, K. *A Metal-rich Low-gravity Companion to a Massive Millisecond Pulsar*, ApJ, 765:158-166 (2013)

[73] Kaspi, V. M.; Taylor, J. H.; and Ryba, M. F. *High-Precision Timing of Millisecond Pulsars. 3: Long-Term Monitoring of PSRs B1855+09 and B1937+21*, ApJ, 428:713-728 (1994)

[74] King, A. R. *Irradiation of the Companion Star in Cataclysmic Variables*, MNRAS, 241:365-374 (1989)

[75] King, A. R.; Frank, J.; Kolb, U.; and Ritter, H. *Mass Transfer Cycles in Cataclysmic Variables*, ApJ, 444:L37-L40 (1995)

[76] King, A. R.; Frank, J.; Kolb, U.; and Ritter, H. *Global Analysis of Mass Transfer Cycles in Cataclysmic Variables*, ApJ, 467:761-772 (1996)

[77] King, A. R.; Frank, J.; Kolb, U.; and Ritter, H. *Mass Transfer Cycles in Close Binaries with Evolved Companions*, ApJ, 482:919-928 (1997)

[78] King, A. R. *Accretion in Compact Binaries*, in Lewin, W. H. G. and van der Klis, M. (eds) *Compact Stellar X-ray Sources*, Cambridge University Press, Cambridge (2006)

[79] Kippenhahn, R. and Weigert, A. *Stellar Structure and Evolution*, Springer-Verlag, Germany (1991)

[80] Kiziltan, B.; Kottas, A.; and Thorsett, S. *The Neutron Star Mass Distribution*, arxiv:1011.4291 (2010)

[81] Kolb, U. *Extreme Environment Astrophysics*, Cambridge University Press, New York (2010)

[82] Kopal, Z. *Close Binary Systems*, Chapman & Hall, London (1959)

[83] Kraft, R. *Studies of Stellar Rotation. V. The Dependence of Rotation On Age Among Solar-Type Stars*,_ApJ, 150: 551-570 (1969)

[84] Kramer, M. *Exploiting Binary Pulsars as Laboratories of Gravity Theories*, in Colpi, M.; Casella, P.; Gorini, V.; Moschella, U.; and Possenti, A. (eds) *Physics of Relativistic Objects in Compact Binaries: From Birth to Coalescence*, Springer, Bristol (2009)

[85] Kuiper, L.; Hermsen, W.; Verbunt, F.; Ord, S.; Stairs, I.; and Lyne, A. *High-Resolution Spatial and Timing Observations of Millisecond Pulsar PSR J0218+4232 with Chandra*, ApJ, 577:917-922 (2002)

[86] Landau, L. D. and Lifshitz, E. M. *The Classical Theory of Fields*, Pergamon Press, Oxford UK (1989)

[87] Lattimer, J. M. and Prakash, M. *Neutron Star Structure and the Equation of State*, ApJ, 550:426-442 (2001)

[88] Lattimer, J. M. *Neutron Stars*, 33rd SLAC Summer Institute on Particle Physics (2005)

[89] Lavagetto, G.; Burderi, L.; D'Antona, F.; Di Salvo, T.; Iaria, R.; and Robba, N. *The Role of General Relativity in the Evolution of Low-Mass X-ray Binaries*, MNRAS, 359:734-740 (2005)

[90] Lin, J.; Rappaport, S.; Podsiadlowski, Pd.; Nelson, L.; Paxton, B.; and Todorov, P. *LMXB and IMXB Evolution: I. The Binary Radio Pulsar PSR J1614-2230*, ApJ, 732:70-78 (2011)

[91] Lipunov, V. M. *Astrophysics of Neutron Stars*, Springer-Verlag, US (1992)

[92] Longair, M. S. *High Energy Astrophysics, Volume 1: Particles, Photons and their Detection*, Cambridge University Press, Cambridge (1992)

[93] Longair, M. S. *High Energy Astrophysics, Volume 2: Stars, the Galaxy and the interstellar medium*, Cambridge University Press, Cambridge (1994)

[94] Lorimer, D. R.; Nicastro, L.; Lyne, A. G.; Bailes, M.; Manchester, R. N.; Johnston, S.; Bell, J. F.; D'Amico, N.; and Harrison, P. A. *Four New Millisecond Pulsars in the Galactic Disk*, ApJ, 439:933-938 (1995)

[95] Lorimer, D. R.; Lyne, A. G.; Bailes, M.; Manchester, R. N.; D'Amico, N.; Stappers, B. W.; Johnston, S.; and Camilo, F. *Discovery of Four Binary Millisecond Pulsars*, ApJ, 283:1383-1387 (1996)

[96] Lynch, R. S.; Freire, P. C. C.; Ransom, S. M.; and Jacoby, B. A. *The Timing of Nine Globular Cluster Pulsars*, ApJ, 745:109-120 (2012)

[97] Lynch, R. S. and Ransom, S. M. *A New Pulsar in Green Bank Telescope Searches of 10 Globular Clusters*, ApJ, 730:L11-L15 (2011)

[98] Lynch, R. S.; Ransom, S. M.; Freire, P. C. C.; and Stairs, I. H. Six New Recycled Globular Cluster Pulsars Discovered with the Green Bank Telescope, ApJ, 734:89-96 (2011)

[99] Maisonneuve, F., *High and Low Metallicity Stellar Modeling of Low-Mass Stars and Brown Dwarfs*, M.Sc. Thesis, Bishop's University (2007)

[100] McCormick, P. and Frank, J. *Evolutionary Effects of Irradiation in Cataclysmic Variables*, ApJ, 500:923-934 (1998)

[101] Melia, F. *High-Energy Astrophysics*, Princeton University Press, US (2009)

[102] Misner, C. W.; Thorne, K. S.; and Wheeler, J. A. *Gravitation*, Freeman, New York US (1973)

[103] Morrison, R. and McCammon, D. *Interstellar Photoelectric Absorption Cross Sections, 0.03-10 keV*, ApJ, 270:119-122 (1983)

[104] Navarro, J.; de Bruyn, A. G.; Frail, D. A.; Kulkarni, S. R.; and Lyne, A. G. A *Very Luminous Binary Millisecond Pulsar*, ApJ, 455:L55-L58 (1995)

[105] Nelson, L. A.; Chau, W. Y.; and Rosenblum, A. *Evolution of Rotationally and Tidally Distorted Low-Mass, Close Binary Systems - Implications for the Minimum Orbital Period of Cataclysmic Variables*, ApJ, 299:658-667 (1985)

[106] Nelson, L. A.; Dubeau, E.; and MacCannell, K. A. *Evolutionary Properties of Helium-Rich, Degenerate Dwarfs in Binaries Containing Compact Companions*, ApJ, 616:1124-1147 (2004)

[107] Nelson, L. A. and Rappaport, S. *Theoretical Considerations on the Properties of Accreting Millisecond Pulsars*, ApJ, 598:431-445 (2003)

[108] Nice, D. J.; Splaver, E. M.; and Stairs, I. H. *On the Mass and Inclination of the PSR J2019+2425 Binary System*, ApJ, 549:516-521 (2001)

[109] Nice, D. J.; Splaver, E. M.; and Stairs, I. H. *Neutron Star Masses from Arecibo Timing Observations of Five Pulsar-White Dwarf Binary Systems* in Bailes, M.; Nice, D. J.; and Thorsett, S. E. (eds) *Radio Pulsars*, Astronomical Society of the Pacific, San Francisco (2003)

[110] Nice, D. J.; Splaver, E. M.; Stairs, I. H.; Löhmer, O.; Jessner, A.; Kramer, M.; and Cordes, J. M. *A 2.1 $M_\odot$ Pulsar Measured by Relativistic Orbital Decay*, ApJ, 634:1242-1249 (2005)

[111] Nice, D. J.; Stairs, I. H.; and Kasian, L. E. *Masses of Neutron Stars in Binary Pulsar Systems*, 40 YEARS OF PULSARS: Millisecond Pulsars, Magnetars and More, 983:453-458 (2008)

[112] Osaki, Y. *Irradiation-Induced Mass-Overflow Instability as a Possible Cause of Superoutbursts in SU UMa Stars*, Astronomy and Astrophysics, 144:369-380 (1985)

[113] Özel, F.; Psaltis, D.; Narayan, R.; and Villarreal, A. S. *On the Mass Distribution and Birth Masses of Neutron Stars*, ApJ, 757:55-68 (2012)

[114] Paczyński, B. *Gravitational Waves and the Evolution of Close Binaries*, Acta Astronomicam 17:287-296 (1967)

[115] Paczyński, B. *Evolutionary Processes in Close Binary Systems*, Annual Review of Astronomy and Astrophysics, 9:183-208 (1971)

[116] Paczyński, B. and Prószyński, M. *Models of Radiation-Driven Winds from General Relativistic Neutron Stars*, ApJ, 302:519-529 (1986)

[117] Pallanca, C.; Dalessandro, E.; Ferraro, F. R.; Lanzoni, B.; Rood, R. T.; Possenti, A.; D'Amico, N.; Freire, P. C.; Stairs, I.; Ransom, S. M.; and Bégin, S. *The Optical Companion to the Binary Millisecond Pulsar J1824-2452H in the Globular Cluster M28*, ApJ, 725:1165-1169 (2010)

[118] Paxton, B.; Bildsten, L.; Dotter, A.; Herwig, F.; Lesaffre, P.; and Timmes, F. *Modules for Experiments in Stellar Astrophysics (MESA)*, ApJ S, 192:3-38 (2011)

[119] Pfahl, E.; Rappaport, S.; and Podsiadlowski, Ph. *The Galactic Population of Low- and Intermediate-Mass X-Ray Binaries*, ApJ, 597:1036-1048 (2003)

[120] Podsiadlowski, Ph. *Irradiation-driven Mass Transfer in Low-Mass X-ray Binaries*, Nature, 350:136-138 (1991)

[121] Podsiadlowski, Ph. *Irradiation-Driven Mass Transfer in Low-Mass X-ray Binaries*, in Kondo, Y.; Sisteró, R. F.; and Polidan, R. S. (eds) Evolutionary Processes in Interacting Binary Stars, Kluwer Academic Publishers, Dordrecht (1992)

[122] Podsiadlowski, Ph.; Rappaport, S.; and Pfahl, E. D. *Evolutionary Sequences for Low- and Intermediate-Mass X-ray Binaries*, ApJ, 565:1107-1133 (2002)

[123] Podsiadlowski, Ph.; Rappaport, S.; and Han, Z. *On the Formation and Evolution of Black Hole Binaries*, MNRAS, 341:385-404 (2003)

[124] Ponman, T. J.; Foster, A. J.; and Ross, R. R. *Self-Consistent Comptonised Models for The Spectra of Low-Mass X-ray Binaries*, in *ESA, The 23rd ESLAB Symposium on Two Topics in X Ray Astronomy. Volume 1: X Ray Binaries*, 296:585:591 (1989)

[125] Potekhin, A. Y. and Chabrier, G. *Thermodynamic Functions of Dense Plasmas: Analytic Approximations for Astrophysical Applications*, Contributions to Plasma Physics, 50:82-87 (2010)

[126] Prialnik, D. *An Introduction to the Theory of Stellar Structure and Evolution*, Cambridge University Press, UK (2010)

[127] Pylyser, E. and Savonije, G. J. *Evolution of Low-Mass Close Binary Systems with a Compact Mass Accreting Component*, Astronomy and Astrophysics, 191:57-70 (1988)

[128] Pylyser, E. H. P. and Savonije, G. J. *The Evolution of Low-Mass Close Binary Systems with a Compact Component. II - Systems Captured by Angular Momentum Losses*, Astronomy and Astrophysics, 208:52-62 (1989)

[129] Ransom, S. M.; Greenhill, L. J.; Herrnstein, J. R.; Manchester, R. N.; Camilo, F.; Eikenberry, S. S.; and Lyne, A. G. *A Binary Millisecond Pulsar in Globular Cluster NGC 6544*, ApJ, 546:L25-L28 (2001)

[130] Ransom, S. M.; Hessels, J. W. T.; Stairs, I. H.; Freire, P. C. C.; Camilo, F.; Kaspi, V. M.; and Kaplan, D. L. *Twenty-One Millisecond Pulsars in Terzan 5 Using the Green Bank Telescope*, Science, 307:892-896 (2005)

[131] Ransom, S. M.; Stairs, I. H.; Backer, D. C.; Greenhill, L. J.; Bassa, C. G.; Hessels, J. W. T.; and Kaspi, V. M. *Green Bank Telescope Discovery of Two Binary Millisecond Pulsars in the Globular Cluster M30*, ApJ, 604:328-338 (2004)

[132] Rappaport, S. A.; Fregeau, J. M.; and Spruit, H. *Accretion onto Fast X-Ray Pulsars*, ApJ, 606:436-443 (2004)

[133] Rappaport, S.; Podsiadlowski, Ph.; Joss, P. C.; Di Stefano, R.; and Han, Z. *The Relation between White Dwarf Mass and Orbital Period in Wide Binary Radio Pulsars*, MNRAS, 273:731-741 (1995)

[134] Rappaport, S.; Verbunt, F.; and Joss, P. C. *A New Technique for Calculations of Binary Stellar Evolution, with Application to Magnetic Braking*, ApJ, 275:713-731 (1983)

[135] Ritter, H. *Turning On and Off Mass Transfer in Cataclysmic Binaries*, Astronomy and Astrophysics, 202:93-100 (1988)

[136] Ritter, H. *Secular Evolution of Compact Binaries: Tema Con Variazioni*, Memorie della Società Astronomia Italiana, 65:173-181 (1994)

[137] Ritter, H. *Is Irradiation Important for the Secular Evolution of Low-Mass X-ray Binaries?,* New Astronomy Reviews, 51:869-877 (2008)

[138] Ritter, H.; Zhang, Z.; and Kolb, U. *The Reaction of Low-Mass Stars to Anisotropic Irradiation and its Implications for the Secular Evolution of Cataclysmic Variables*, in van Paradijs, J.; van den Heuvel, E. P. J.; and Kuulkers, E. (eds) *Compact Stars in Binaries*, Kluwer Academic Publishers, Dordrecht (1996)

[139] Ritter, H.; Zhang, Z.; and Kolb, U. *Irradiation and Mass Transfer in Low-Mass Compact Binaries*, Astronomy and Astrophysics, 360:969-990 (2000)

[140] Rogers, F. J. and Nayfonov, A. *Updated and Expanded OPAL Equation-of-State Tables: Implications for Helioseismology*, ApJ, 576:1064-1074 (2002)

[141] Ross, R. R. *Spectral Formation in Compact X-ray Sources*, ApJ, 233:334-343 (1979)

[142] Ross, R. R. and Fabian, A. C. *The Spectra of Accretion Disks in Low-Mass X-ray Binaries*, MNRAS, 281:637-643 (1996)

[143] Rosswog, S. and Brüggen, M. *Introduction to High-Energy Astrophysics*, Cambridge University Press, UK (2007)

[144] Ruderman, M.; Shaham, J.; Tavani, M.; and Eichler, D. *Late Evolution of Very Low Mass X-ray Binaries Sustained by Radiation from their Primaries*, ApJ, 343:292-312 (1989)

[145] Saumon, D.; Chabrier, G.; and van Horn, H. M. *An Equation of State for Low-Mass Stars and Giant Planets*, ApJ S, 99:713-741 (1995)

[146] Schulz, N. S. *ROSAT Energy Spectra of Low-Mass X-ray Binaries*, ApJ, 511:304-323 (1999)

[147] Schulz, N. S.; Hasinger, G.; and Trümper, J. *Spectral Classification of Low-Mass X-ray Binary (LMXB) Energy Spectra with Color-Color Diagrams*, Astronomy and Astrophysics, 225:48-68 (1989)

[148] Schwab, J.; Podsiadlowski, Ph.; and Rappaport, S. *Further Evidence for the Bimodal Distribution of Neutron-Star Masses*, ApJ, 719:722-727 (2010)

[149] Shakura, N. I. and Sunyaev, R. A._*Black Hole in Binary Systems: Observational Appearance*, A&A, 24:337-335 (1973)

[150] Shapiro, S. L. and Teukolsky, S. A. *Black Holes, White Dwarfs, and Neutron Stars: The Physics of Compact Objects*, Wiley, US (1983)

[151] Shapiro, S. L. and Salpeter, E. E. *Accretion onto Neutron Stars under Adiabatic Shock Conditions*, ApJ, 198:671-682 (1975)

[152] Shu, F. *The Physical Universe: An Introduction to Astronomy*, University Science Books, Mill Valley CA (1982)

[153] Soberman, G. E.; Phinney, E. S.; and van den Heuvel, E. P. J. *Stability Criteria for Mass Transfer in Binary Stellar Evolution*, Astronomy and Astrophysics, 327:620-635 (1997)

[154] Splaver, E. M. and Nice, D. J. *Probing the Masses of the PSR J0621+1002 Binary System through Relativistic Apsidal Motion*, ApJ, 581:509-518 (2002)

[155] Splaver, E. M.; Nice, D. J.; Stairs, I. H.; Lommen, A. N.; and Backer, D. C. *Masses, Parallax, and Relativistic Timing of the PSR J1713+0747 Binary System*, ApJ, 620:405-415 (2005)

[156] Stairs, I. H. *Masses of Radio Pulsars*, Journal of Physics G: Nuclear and Particle Physics, 32:S259-S265 (2006)

[157] Tauris, T. M. and van den Heuvel, E. P. J. *Formation and Evolution of Compact Stellar X-ray Sources*, in Lewin, W. H. G. and van der Klis, M. (eds) *Compact Stellar X-ray Sources*, Cambridge University Press, Cambridge (2006)

[158] Tauris, T. M.; Langer, N.; and Kramer, M. *Formation of Millisecond Pulsars with CO White Dwarf Companions - I. PSR J1614-2230: Evidence for a Neutron Star Born Massive*, MNRAS, 416:2130-2142 (2011)

[159] Tauris, T. M.; Langer, N.; Kramer, M. *Formation of millisecond pulsars with CO white dwarf companions - II. Accretion, spin-up, true ages and comparison to MSPs with He white dwarf companions*, MNRAS, 425:1601-1627 (2012)

[160] Tauris, T. M. and Savonije, G. J. *Formation of millisecond pulsars. I. Evolution of low-mass X-ray binaries with $P_{orb} < 2$ days*, Astronomy and Astrophysics, 350:928-944 (1999)

[161] Tavani, M. *Orbital Evolution of Low-Mass X-ray Binaries due to Radiation Driven Mass Transfer*, Nature, 351:39-41 (1991)

[162] Tavani, M. *Irradiation-Driven Evolution of Low-Mass X-ray Binaries and Binary Millisecond Pulsars*, Memorie della Società Astronomia Italiana, 65:291-300 (1994)

[163] Tavani, M. and London, R. *Hydrodynamics of Winds from Irradiated Companion Stars in Low-Mass X-ray Binaries*, ApJ, 410:281-294 (1993)

[164] Thorsett, S. E.; Arzoumanian, Z.; McKinnon, M. M.; and Taylor, J. H. *The Masses of two Binary Neutron Star Systems*, ApJ, 405:L29-L32 (1993)

[165] Thorsett, S. E. and Chakraborty, D. *Neutron Star Mass Measurement. I. Radio Pulsars*, ApJ, 512:288-299 (1999)

[166] Timmes, F. X. and Swesty, F. D. *The Accuracy, Consistency, and Speed of an Electron-Positron Equation of State Based on Table Interpolation of the Helmholtz Free Energy*, ApJ S, 126:501-516 (2000)

[167] Treves, A.; Maraschi, L; and Abramowicz, M. *Basic Elements of the Theory of Accretion*, in Treves, A.; Maraschi, L; and Abramowicz, M. (eds) *Accretion: A Collection of Influential Papers*, World Scientific Publishing, Singapore (1989)

[168] Tuchman, Y. and Yahel, R. Z. *Accretion onto Neutron Star: The X-ray Spectra and Luminosity*, Astrophysics and Space Science, 50:473-492 (1977)

[169] Valentim, R.; Rangel, E.; and Horvath, J. E. *On the Mass Distribution of Neutron Stars*, MNRAS, 414(2):1427-1431 (2011)

[170] van den Heuvel, E. P. J. *The Formation and Evolution of Relativistic Binaries*, in Colpi, M.; Casella, P.; Gorini, V.; Moschella, U.; and Possenti, A. (eds) *Physics of Relativistic Objects in Compact Binaries: From Birth to Coalescence*, Springer, Bristol (2009)

[171] van Kerkwijk, M. H.; Breton, R. P.; and Kulkarni, S. R. *Evidence for a Massive Neutron Star from a Radial-velocity Study of the Companion to the Black-widow Pulsar PSR B1957+20*, ApJ, 728:95-102 (2011)

[172] Verbiest, J. P. W.; Bailes, M.; van Straten, W.; Hobbs, G. B.; Edwards, R. T.; Manchester, R. N.; Bhat, N. D. R.; Sarkissian, J. M.; Jacoby, B. A.; and Kulkarni, S. R. *Precision Timing of PSR J0437-4715: An Accurate Pulsar Distance, a High Pulsar Mass, and a Limit on the Variation of Newton's Gravitational Constant*, ApJ, 679:675-680 (2008)

[173] Verbunt, F. and Zwaan, C. *Magnetic Braking in Low-mass X-ray Binaries*, Astronomy and Astrophysics, 100: L7-L9 (1981)

[174] Vilhu, O.; Ergma, E.; and Fedorova, A. *The X-ray Heating and Evolution of LMXB's*, Astronomy and Astrophysics, 291:842-846 (1994)

[175] Wald, R. M. *General Relativity*, The Chicago University Press, Chicago US (1984)

[176] Warner, B. *Cataclysmic Variable Stars*, Cambridge University Press, Cambridge MA (1995)

[177] Webbink, R. F.; Rappaport, S.; and Savonije, G. J. *On the Evolutionary Status of Bright, Low-Mass X-ray Sources*, ApJ, 270:678-693 (1983)

[178] Xilouris, K. M.; Kramer, M.; Jessner, A.; von Hoensbroech, A.; Lorimer, D.; Wielebinski, R.; Wolszczan, A.; and Camilo, F. *The Characteristics of Millisecond Pulsar Emission. II. Polarimetry*, ApJ, 501:286-306 (1998)

[179] Zhang, S. N.; Yu, W.; and Zhang, W. *Spectral Transitions in Aquila X-1: Evidence for "Propeller" Effects*, ApJ, 494:L71-L74 (1998)